Epitaxial Growth and Characterization for Thin Films of Colossal Magnetoresistive Layered Manganates(Dissertation_全文)

AUTHOR(S):

Lmouchter, Mohamed

Epitaxial Growth and Characterization for Thin Films of Colossal Magnetoresistive Layered Manganates

March 2008

Mohamed LMOUCHTER

Electronic Science and Engineering
Kyoto University

Abstract

The present thesis is a study on the c-axis epitaxial growth and characterization for thin films of colossal magnetoresistive layered manganates. Along the c-axis, the crystal structure of these materials can be regarded as a stack of spin tunnel junctions. This feature endows the layered manganates with technologically attractive properties. For instance, it produces peculiarly high magnetoresistance effects. Towards the extraction of these ideal spin tunnel junctions for a detailed study of spin tunneling phenomena, this work studies the c-axis epitaxial growth for layered manganate thin films. The grown films are characterized in order to assess their quality and confirm their applicability to the study of spin tunneling.

The crystal structure of the layered manganates is based on the perovskite structure. Depending on the chemical composition, these materials form in different crystal structures called the Ruddelsden-Popper series. In the La-Sr-Mn-O system, their general chemical formula is $(La,Sr)_{n+1}Mn_nO_{3n+1}$ (n, integer). In the case of $n = \infty$, the chemical formula becomes $(La,Sr)MnO_3$, and the crystal structure is reduced to the simple perovskite structure without crystal anisotropy (LSMO113). When $n \geq 1$, the crystal structure along the c-axis becomes a stack of n LSMO113 magnetic layers separated by a non-magnetic insulating (La,Sr)O layer. This results in a highly anisotropic structure. In the present study, because of its intrinsic spin tunneling characteristic, the layered manganate $(La,Sr)_3Mn_2O_7$ of $n = 2$ is the main research subject. The epitaxial growth and characterization of LSMO113 films, however, is studied first because it is of great value when analyzing and discussing the properties of LSMO327 thin films. Then, the c-axis epitaxial growth of LSMO327 thin films is studied. It is shown that in order to achieve the c-axis epitaxial growth of layered manganate thin films, control of the deposition rate is crucial (e.g., ≤ 0.8 nm/min at 760 °C). The obtained c-axis epitaxial thin films at this stage are characterized, and it is concluded that they contain about 40 % of defects typical to this system, i.e., intergrowths from the LSMO113 and LSMO214 ($n = 1$) phases. The quantitative method for characterizing these intergrowths is also presented. Next, it is shown that partial substitution of Mn for Cu (Cu doping) is effective in improving the c-axis epitaxial growth of layered manganate thin films. The effect of Cu-substitution on the electronic properties is also studied. Finally, using a new sputtering configuration, c-axis epitaxial layered manganate thin films with an amount of intergrowths less than 20 % are grown and characterized. These films have magnetic and electrical properties close to those of the bulk. They are suitable for intrinsic spin tunneling

studies such as those based on small mesa structures fabricated on film's surface.

After giving some background on this study in Chapter 1 and explaining the used experimental methods in Chapter 2, the epitaxial growth and characterization of LSMO113 thin films is described in Chapter 3. The relation between the film growth and the sputtering conditions is studied. The electrical and magnetic properties of the films are characterized and the optimal epitaxial growth conditions are determined. It is shown that epitaxial thin films grown at 820 °C have the best crystalline quality compared with those grown at lower substrate temperatures. When these films are annealed in oxygen at 900 °C, they show magnetic and electrical characteristics comparable to those of bulk single crystals. LSMO113 thin films thus grown show streaky RHEED patterns that indicate that their surface is considerably smooth, and that they are suitable for multilayer film fabrication. Exploiting their full spin polarization property, LSMO113 epitaxial thin films, combined with high-T_c superconductor thin films, are used to fabricate a spin-injection device.

In Chapter 4, the *c*-axis epitaxial growth and characterization for the layered manganate $(La,Sr)_3Mn_2O_7$ are studied. It is shown that at 820 °C, only *a*-axis thin films can be grown. After reconstruction of the heater block, *c*-axis thin films appear at substrate temperatures above 900 °C. However, their crystalline quality is very poor, and therefore, the deposition rate is decreased in order to improve the *c*-axis epitaxial growth. It is shown that the film quality is largely improved by decreasing the growth rate from 25 to 0.8 nm/min. The magnetic and electrical properties are, however, far from the bulk ones and the surface of the film shows many precipitates because the film contains many intergrowths such as LSMO113 and LSMO214. Then, a quantitative method for characterizing these intergrowths based on X-ray diffraction (XRD) experiment and simulation is developed. The results indicate that the above *c*-axis LSMO327 epitaxial thin films contain about 40 % of intergrowths. Based on these results, the *c*-axis epitaxial growth for the layered manganates and the properties of the grown films are discussed.

In Chapter 5, the effects of Cu-substitution of Mn on the *c*-axis epitaxial growth and on the properties of layered manganates are studied. Cu-substitution facilitates the fabrication of sputtering targets for the manganates, but most importantly, it lowers their melting point. Therefore, the atom's migration is fostered at the growing film surface. This is of crucial importance for the *c*-axis epitaxial growth. It is shown that, as expected, the *c*-axis epitaxial growth is improved by introducing Cu. This improvement and the effect of Cu on the electronic properties of layered manganates are discussed.

In Chapter 6, in order to grow better *c*-axis epitaxial layered manganate thin films, a new sputtering configuration is proposed. By placing an intermediate plate between the sputtering target and the substrate, the high-energy particles that exist during sputtering are suppressed. Thus, it can be said that the film growth takes place in a mild environment free from disturbances. Using this configuration, *c*-axis epitaxial layered manganate thin films with intergrowth contents less than 20 % are achieved. The electronic properties of these thin films are close to those of bulk single crystals.

In Chapter 7, the results obtained in this study are summarized with conclusions.

Acknowledgements

I would like to express my deep and sincere gratitude to my supervisor Professor Minoru Suzuki for his guidance throughout this work. His understanding, encouragement, illuminating discussions, and invaluable advices during my time in the laboratory are highly appreciated and admired. He is who introduced me to research in both superconductivity and spin electronics, and what I have learnt under his supervision is huge and extends beyond the scope of the present work. I would like also to thank deeply Professor Shizuo Fujita and Professor Gikan Takaoka for their helpful advices and stimulating comments on this dissertation.

I would like to thank Assistant Professor Michinaka Sugano for his interest in this research and for his kind assistance in in-plane X-ray diffraction experiments. I would like to thank also Associate Professor Jun Suda for his advices and support in atomic force microscopy (AFM) and high-resolution scanning electron microscopy (HRSEM) experiments.

Thanks are due to Mr. Kenkichi Anagawa (TDK Corporation). Me and him were the first students in the laboratory. We had many collaborations and shared interesting discussions about our research and many other subjects. I would like to thank also Mr. Hideto Tamaso (Sumitomo Electric Industries, Ltd.), Mr. Masayoshi Iwayama (Toshiba Corporation), Mr. Hirotaka Endo (Panasonic Corporation), Mr. Yosuke Tanaka (Philips Electronics Japan, Ltd.), Mr. Yuji Nakamura (Nippon Yusen Kabushiki Kaisha), Mr. Ryo Tatsumi (Sumitomo Electric Industries, Ltd.), and Mr. Tomoki Ikawa (Integrated Functional Eng. Lab.) for their interest in this work and for their helpful support.

I would like to thank Dr. Tsuyoshi Kawakami (Mitsubishi Electric Corporation) and Dr. Yoshiharu Yamada (NTT Basic Research Laboratory) for the enjoyable discussions and time that we had together. Thanks are also due to all other members of the Integrated Functional Engineering Laboratory for their kind help.

I would like to thank the Ministry of Education, Culture, Sports, Science, and Technology for providing me the opportunity to study in Japan through the Monbusho scholarship program.

I would like also to acknowledge the financial support of the Mitsubishi Foundation and the 21st Century COE Program (Grant for Center of Excellence for Research and Education of Fundamental Technologies in Electrical and Electronic Engineering from the Ministry of Education, Culture, Sports, Science, and Technology).

Warm thanks are due to all my friends from all the countries with whom I had the chance to meet in Japan, for their kind friendship and for the enjoyable time that we had together.

Finally, I would like to thank deeply my family for their unconditional love and generous support.

Table of Contents

Chapter 1

Background

1.1 Introduction

The modern world relies on electronics in almost every aspect of life. One can hardly imagine life without electric light bulbs, mobile phones, or computers, just to name a few. Most of our daily life is now based in a form or another on the work of electrons. Electronics has significantly improved our life, and a significant part of the price that we pay in return is the production of electrical energy necessary for the operation of the electronic devices. Therefore, as the need for electronic functions increases, so is the need for electrical energy. As such, electronic devices that consume power as less as possible will be always sought after.

Using the electron's spin property is a way to reduce energy consumption and, at the same time, to invent some new electronic functions (still) using electrons. A general look at electronics shows that almost all of the devices perform their functions by controlling the electron flow, exploiting the electron's charge property. As is known, the electron is electrically charged with a negative charge of $-e = -1.6\times10^{-19}$ C. However, the electron has also another property, i.e., spin. Spin is purely a quantum-mechanical concept. One can make an analogy between the electron's motion around the nucleus and the earth's motion around the sun. As earth rotates around itself, the electron also rotates around itself, and for this spinning motion, quantum mechanics associates a discrete value of the magnetic moment (spin) $\mu = -e\hbar s/m$, where s can take only two values $\pm1/2$ [1]. Actually, electronics has been using this property, but indirectly. Magnetic materials have been used in many electronic applications, and it is the spin property of the electron that produces the material's magnetic properties. For instance, for most of the ferromagnetic materials, say, Fe, Ni, Co, their alloys, and also for the manganates studied in the present thesis, the contribution from the orbital magnetic moment is negligible, and the contribution of spin to magnetism is the most important [2]. Electronics has only been using the spin without controlling it. Recently, however, the control of the flow of electrons using the electron's spin property has been demonstrated and established, as recently discovered using magnetic

materials or multilayer thin films [3–5].

Using magnetic materials is better than using, for example, semiconductors, because magnetization is not volatile. This leads to new devices with much lower power-consumption characteristics. It also leads to many new functional devices such as the tunneling magnetoresistive (TMR) device [3–5]. As shown in Fig. 1.1, the TMR device consists of two metallic and ferromagnetic layers separated by a thin insulating non-magnetic layer that forms the tunneling barrier. As the resistance depends on the relative directions of the magnetization of the ferromagnetic layers, parallel and antiparallel directions yield two different resistances, which can be associated to the "0" and "1" bits. This has created vitally important electronic products. For example, hard-disc drives with high storage capacities exceeding 100 Gb/in^2 are now common and have been possible thanks to high performance small magnetic read-heads based on TMR (Fig. 1.2) [3, 5–15]. Developments in this field are reporting 100 % increase in density every year. Another important application of TMR is the magnetic random access memory MRAM [3, 4, 16–18]. A structure of MRAM is shown in Fig. 1.3. As shown in Table 1.1, MRAM has all the advantages of other memories, namely, non-volatility, high density, and fast access time. Therefore, it has the potential to become a universal memory. MRAM of 4 Mbits density is being commercialized, and MRAM as large as 16 Mbits also has been produced. Further developments are carried out in many major semiconductor companies.

Many other spintronic applications have been discovered. Magnetic field sensors are another application of spin-dependent devices. These devices have sensitivities of a ten and a few Gausses that compete with Hall devices but they provide a larger output signal [3]. Spin currents can also generate microwave signals. This effect was predicted in the 1990s, and was recently confirmed experimentally [19, 20]. Spin currents injected into magnetic multilayers have produced signals in the GHz range with power in the range of pW with currents in the mA range injected into structures with about 7000 nm^2 area. This has advantages because it provides the possibility for nanoscale microwave sources that can be tuned by injected currents and by applied magnetic fields [21]. Spin field effect transistors also have been proposed, where the collector and emitter are ferromagnets. This transistor uses the change due to spin-orbit coupling upon application of the gate voltage. Thus the spin direction is controlled by the gate voltage. Other variations like the all-metal spin transistor and the ferromagnetic single electron transistor have been suggested and experimentally studied [3, 4, 22]. Advantages of these devices include their high speed operation because the control of switching magnetization is of the order of nanoseconds and the control of spin with gate voltage is estimated to be in the picoseconds. Light emission devices (LED) that rely on the injection of spin currents have also been demonstrated in ferromagnetic semiconductor structures [3, 23]. Analysis of the polarization of the emitted light provides a way to find the polarization of the injected electrons and check the spin injection efficiency. There is also another important application of spin. As it defines the quantum state of a particle, the control and manipulation of this quantum state provides a way to realize a

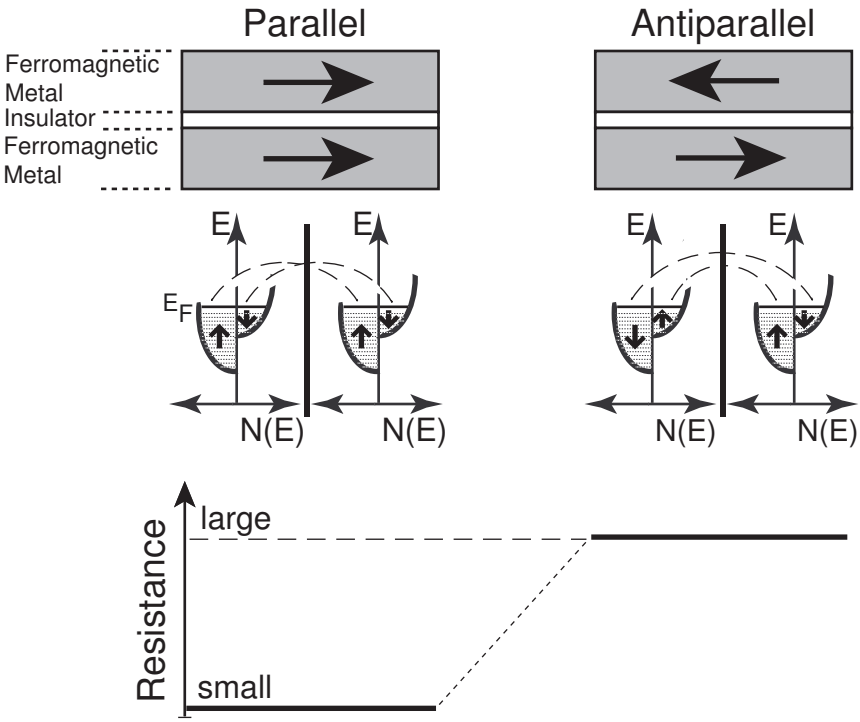

Figure 1.1: Principle of tunneling magnetoresistance (TMR).

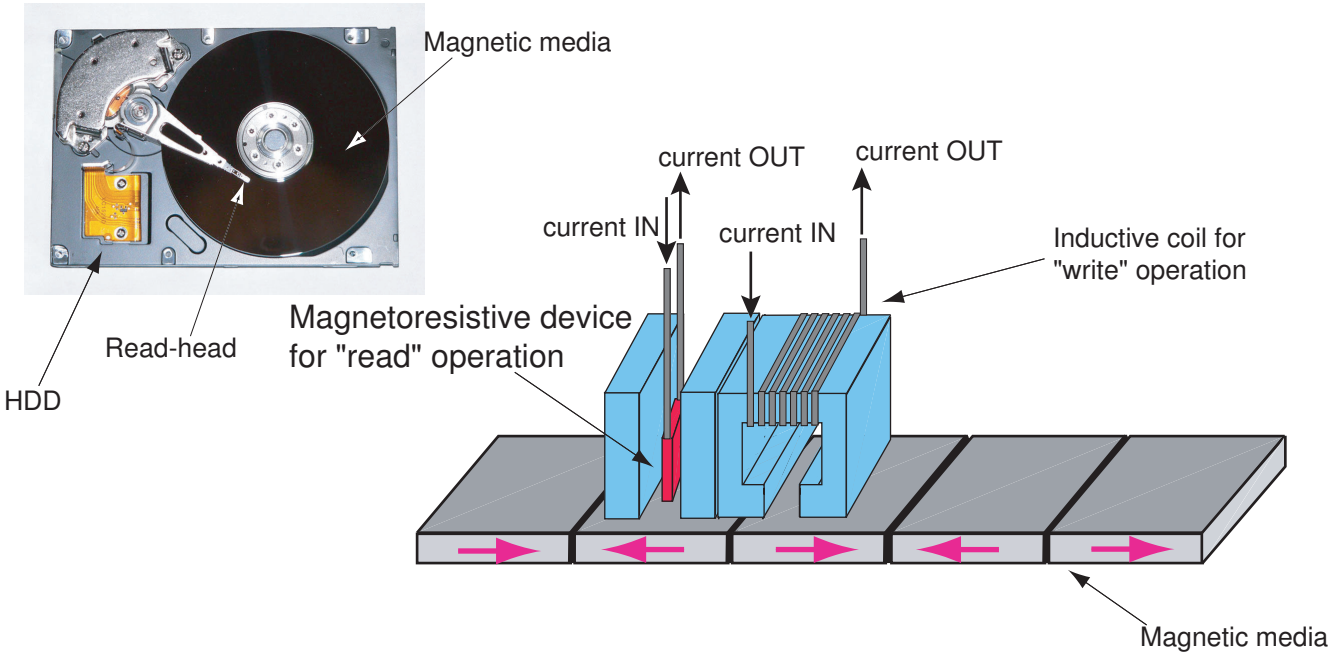

Figure 1.2: Structure of the hard-disc drive and principle of read-head operation.

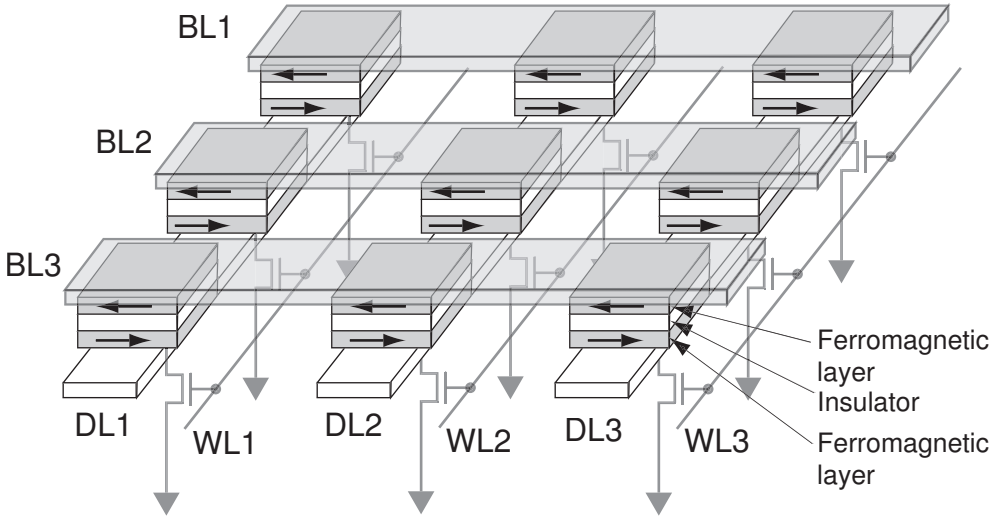

Figure 1.3: Cell structure of a magnetic random access memory (MRAM). BL: bit line, WL: word line, DL: digit line.

Table 1.1: Comparison of MRAM with other memory technologies[a] [25].

	SRAM	DRAM	FLASH	FRAM	MRAM
Read	Fast	Moderate	Fast	Moderate	Moderate-fast
Write	Fast	Moderate	**Slow**	Moderate	Moderate-fast
Nonvolatile	**No**	**No**	Yes	**Partially**[b]	Yes
Endurance	Unlimited	Unlimited	**Limited**[c]	**Limited**[b]	Unlimited
Refresh	No	**Yes**	No	No	No
Cell size	**Large**	Small	Small	Medium	Small
Low voltage	Yes	Limited	**No**	Limited	Yes

[a]Bold letters indicate undesirable attributes.

[b]Destructive read and limited read/write endurance.

[c]Limited write endurance.

quantum computer, which is much faster than all current classical computers. Use can be made of electron or nuclear spin in semiconductor structures because of the large coherence time in semiconductors (of the order of ns). The states of spin 1/2 particles are two-level systems and form the quantum bits (qubits) [3, 9, 24].

The present study is related to how electron spin controls electrical resistance, i.e., magnetoresistance, and is on materials that exhibit peculiarly high magnetoresistance values. Therefore, some background on magnetoresistance and on these materials, i.e., the manganates, is given in the following sections.

1.2 Magnetoresistance

Magnetoresistance (MR) is the change of a material's electrical resistivity under the influence of a magnetic field. The MR effects have been discovered in a variety of materials systems, and they occur by a variety of physical mechanisms. The MR effects known so far are ordinary MR (OMR), anisotropy MR (AMR), giant MR (GMR), colossal MR (CMR), and tunnel MR (TMR).

1.2.1 Ordinary Magnetoresistance (OMR)

In almost every metal, some change in electrical resistance when a magnetic field is applied is always seen (Fig. 1.4) [26]. Electrical conduction is carried out by electrons at the Fermi surface, and these are affected by the Lorentz force created by the magnetic field. This affects the electron's trajectory and generally increases the material's resistance. Both the magnetic field perpendicular and parallel to the current change resistance, but the effect of the former is larger. Appreciable changes are, however, observed for very clean samples, at low temperatures, and in high magnetic fields. Due to this, OMR has not yet found technological applications.

1.2.2 Anisotropic Magnetoresistance (AMR)

Anisotropic magnetoresistance occurs only in ferromagnetic metals [3, 4]. As shown in Fig. 1.5, the material's resistance depends on the direction of the electric current relative to that of the magnetization. Resistance is low when the two directions are perpendicular to each other, and it is high when they are parallel to each other. The physical origin of this anisotropy magnetoresistance (AMR) can be found in the asymmetric scattering cross-section of the conduction electrons (which have unequal densities for each spin type) due to the spin-orbit coupling. The magnitude of AMR in many ferromagnetic metals and alloys is of a few percent at room temperature and in magnetic fields less than a few tens of Oe. This has immediately found technological applications. For example, the inductive read-heads used to measure the local magnetic fields emanating from the recording media

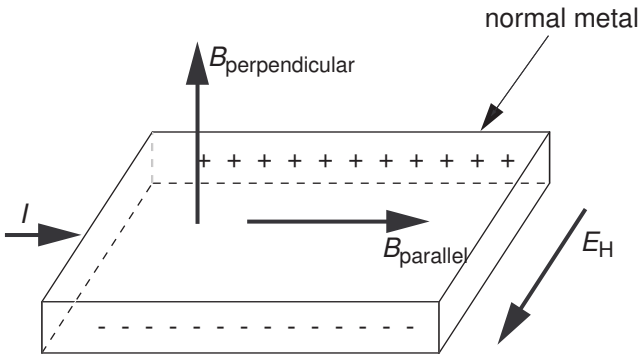

I : electric current
B : magnetic field
E_H : Hall electric field (in the case of $B_{perpendicular}$)

Figure 1.4: Principle of ordinary magnetoresistance (OMR).

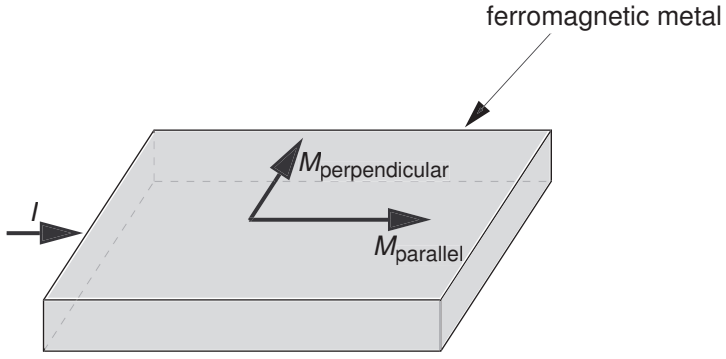

I : electric current
M : magnetization of the ferromagnetic metal

Figure 1.5: Principle of anisotropic magnetoresistance (AMR).

in hard-disc drives were replaced by those based on AMR films of permalloy. These heads were a significant improvement in size and cost.

1.2.3 Giant Magnetoresistance (GMR)

Giant magnetoresistance occurs in multilayers consisting of metallic ferromagnetic layers separated by thin non-magnetic layers (Fig. 1.6). The effect was discovered in 1988 by Baibich *et al.* [27] The physical origin of GMR can be qualitatively understood using the two-spin-current model [3–5]. The ferromagnetic layers are fabricated so that they are antiferromagnetically coupled at 0 magnetic field. In this state, both spin-up and spin-down electrons are frequently scattered at the interface. Therefore, the resistance in this state is high. When a magnetic field is applied to align the magnetization direction of the ferromagnetic layers, the majority spin-up conduction electrons get more easily through the layer interfaces. As a consequence, the resistance drops to a smaller value. Corresponding to these resistive states, both current-in-plane (CIP) and current-perpendicular-to-plane (CPP) configurations exist. With the discovery of GMR, AMR devices in many applications were replaced by devices based on GMR because the effect is more substantial. The AMR read-heads mentioned above were soon replaced by GMR read-heads since 1997. GMR, as opposed to OMR and AMR, is not found in materials properties, but is an engineered effect.

1.2.4 Tunneling Magnetoresistance (TMR)

The phenomenon of electron tunneling through electrically insulating barriers has been known since the development of quantum mechanics. The effect has been used in many basic research studies and also in technological applications using semiconductors and superconductors. The control of electron tunneling using the electron's spin state was experimentally discovered in the 1970s using tunnel junctions made from superconductors and ferromagnetic metallic electrodes [28]. Spin-dependent tunneling in ferromagnetic tunnel junctions also had been studied, but a larger interest in this field had to wait for the breakthrough achieved in 1995 by Moodera *et al.* [29] A qualitative explanation of TMR in the case of identical ferromagnetic electrodes is as follows (Fig. 1.1). In the ferromagnetic state, the metal has two spin-dependent electron densities at the Fermi level, $N_\uparrow$ for spin-up electrons, and $N_\downarrow$ for spin-down electrons. As the tunneling probability t is proportional to the density of state at both electrodes, $t \propto N_\uparrow^2 + N_\downarrow^2$ when the magnetizations are parallel. When these are antiparallel, $t \propto N_\uparrow N_\downarrow + N_\downarrow N_\uparrow = 2N_\uparrow N_\downarrow$. Because $t \propto N_\uparrow^2 + N_\downarrow^2 \geq 2N_\uparrow N_\downarrow$, the resistance when the magnetization vectors are parallel is lower than its value when they are antiparallel. It is clear that high spin polarizations and coherent interfaces are necessary in order to obtain a substantial magnetoresistance effect in these structures. TMR performance has significantly improved. At present, TMR values exceeding 70 % at room temperature are reached, after taking some care of the interface problem. Current TMR

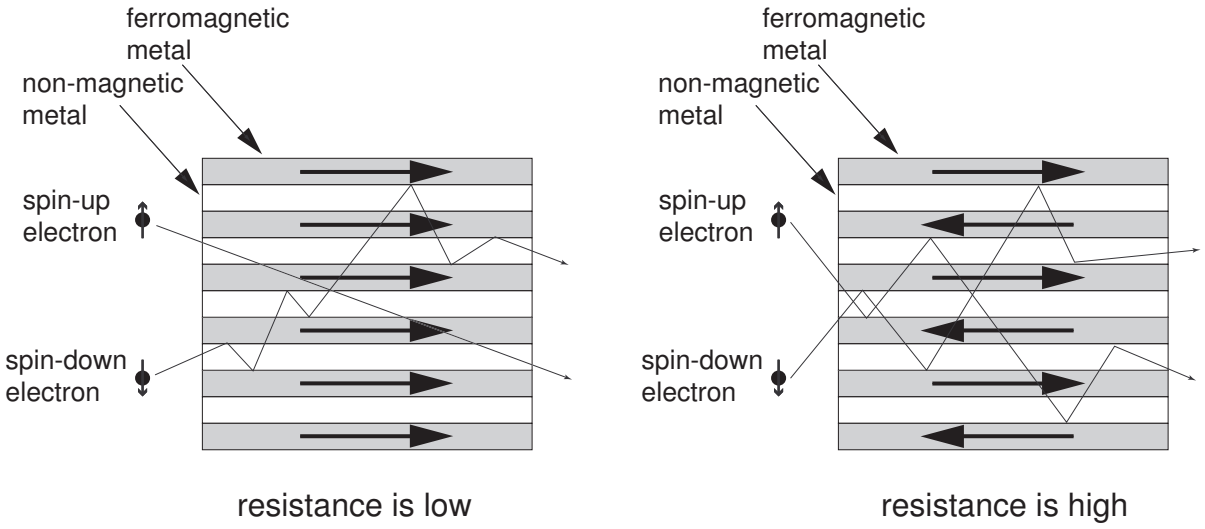

Figure 1.6: Principle of giant magnetoresistance (GMR).

applications include read-heads for hard-disc drives and magnetic random access memory (MRAM) as mentioned in Section 1.1.

1.2.5 Colossal Magnetoresistance (CMR)

A much larger, colossal, magnetoresistance effect was discovered in mixed-valence manganates with a perovskite structure, $Re_{1-x}Ae_x\mathrm{MnO_3}$ where Re is a rare earth ion and Ae is a divalent alkaline. In 1993, von Helmolt *et al.* observed an $[\rho(7T) - \rho(0)]/\rho(0)$ of 60 % at room temperature in $\mathrm{La_{0.67}Ba_{0.33}MnO_3}$ thin films [30]. In the following year, Jin *et al.* reported an MR effect in excess of a million percent at 77 K in a $\mathrm{La_{0.67}Ca_{0.33}MnO_3}$ thin film [31]. Later, similar large MR effects were observed in other complex oxides such as layered perovskites ($\geq$ 90 % at 4.2 K) [32]. The CMR effect in $Re_{1-x}Ae_x\mathrm{MnO_3}$ occurs mainly because of a close correlation between the magnetic phase transition and the electronic phase transition near the Curie temperature T_C [33]. A detailed description of CMR mechanism will be given in the next section. Because the CMR effect usually requires large magnetic fields, typically in the range of several teslas, the technological applications of the CMR are largely limited so far. However, the conduction electrons in CMR materials are known to be nearly perfectly spin-polarized, and this is highly attractive for TMR structures with high TMR values. This property is also used for spin injection into other materials such as superconductors in order to study their fundamental properties and to search for new spintronic devices. Moreover, as discussed later, the layered manganates can be considered as a stack of intrinsic tunnel junctions in the c-axis direction. These junctions, unlike their artificial counterparts, are perfectly smooth. Therefore, the study of spin tunneling using perfect tunnel junctions is possible using these materials.

1.3 Manganates: Colossal Magnetoresistive and Spin Injector Materials

The manganates are manganese oxides. Because of the magnetic element Mn, the manganates are magnetic materials that show antiferromagnetism or ferromagnetism. Research into the manganates started from the 1950s, when the correlation between magnetism and electric conduction was discovered [34–39]. It was of interest to the physics community because in common ferromagnetic metals, such as Ni or Fe, the electrical conductivity does not change between the normal state and the ferromagnetic state. In the manganates, in contrast, the ferromagnetic phase transition from a normal to a ferromagnetic state is at the same time accompanied by an electrical phase transition from a semiconducting state with high resistivity to a metallic state with low resistivity. This phase transition, when controlled by a magnetic field, produces a large change in electrical resistivity, i.e., "colossal magnetoresistance (CMR)" [33]. The manganates are, unlike other ferromagnetic metals,

half-metallic, as the conduction band is formed from a single spin species. This is useful in spin-related studies.

1.3.1 Crystal structure

The main building block of the manganates crystal structure is, as in high-T_c superconductor cuprates, the perovskite structure ABO_3 shown in Fig. 1.7, where A is a rare earth element and B is a transition metal element [33]. In the superconducting cuprates B = Cu, while in the manganates B = Mn.

Manganese perovskites show a series of crystal structures called the Ruddelsden-Popper series as shown in Fig. 1.8, depending on composition. The general formula is $A_{n+1}\mathrm{Mn}_n\mathrm{O}_{3n+1}$, where n is an integer. $A\mathrm{MnO}_3$, in the case of $n = \infty$, has an isotropic cubic perovskite structure. From $n \geq 1$, the crystal structure starts to show crystallographic anisotropy, and it can be regarded as a stack of n consecutive $A\mathrm{MnO}_3$ layers and an AO layer along the c-axis.

1.3.2 Magnetic properties

Without doping, the manganates are antiferromagnetic insulators. Electrical conduction appears in the ferromagnetic state, and this is achieved by hole doping [33]. In the present study, the triply charged $(A = \mathrm{La})^{3+}$ ion is partially substituted with the doubly charged Sr^{2+}. Properties of La-Sr-Mn-O (LSMO) manganates relevant to this study are summarized below.

LSMO113 ($n = \infty$)

Doping LaMnO_3 with Sr ($\mathrm{La}_{1-x}\mathrm{Sr}_x\mathrm{MnO}_3$) establishes a metallic and ferromagnetic state in the system as shown in the phase diagram of Fig. 1.9. The maximum Curie temperature is approximately 370 K at doping levels near $x = 0.3$ [33]. This temperature is above room temperature, which is of importance in technological applications.

LSMO214 ($n = 1$)

LSMO214 is antiferromagnetic insulator irrespective of doping levels [33, 40, 41]. From the point of view of basic physics, this phase exhibits some interesting phenomena such as charge and orbital ordering. These, however, are not treated in the present study, and therefore, will not be described in detail. To fabricate metallic and ferromagnetic manganate thin films, attention should be paid so that the LSMO214 phase is not formed.

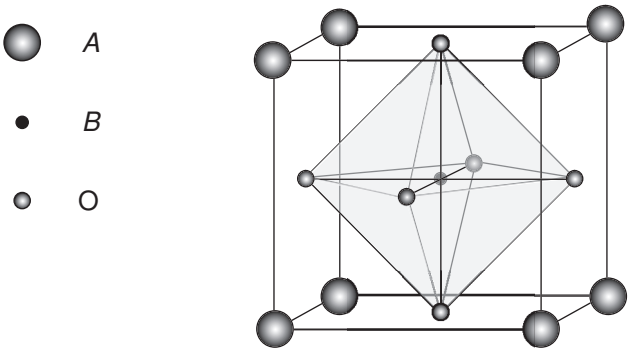

Figure 1.7: Perovskite crystal structure ABO_3.

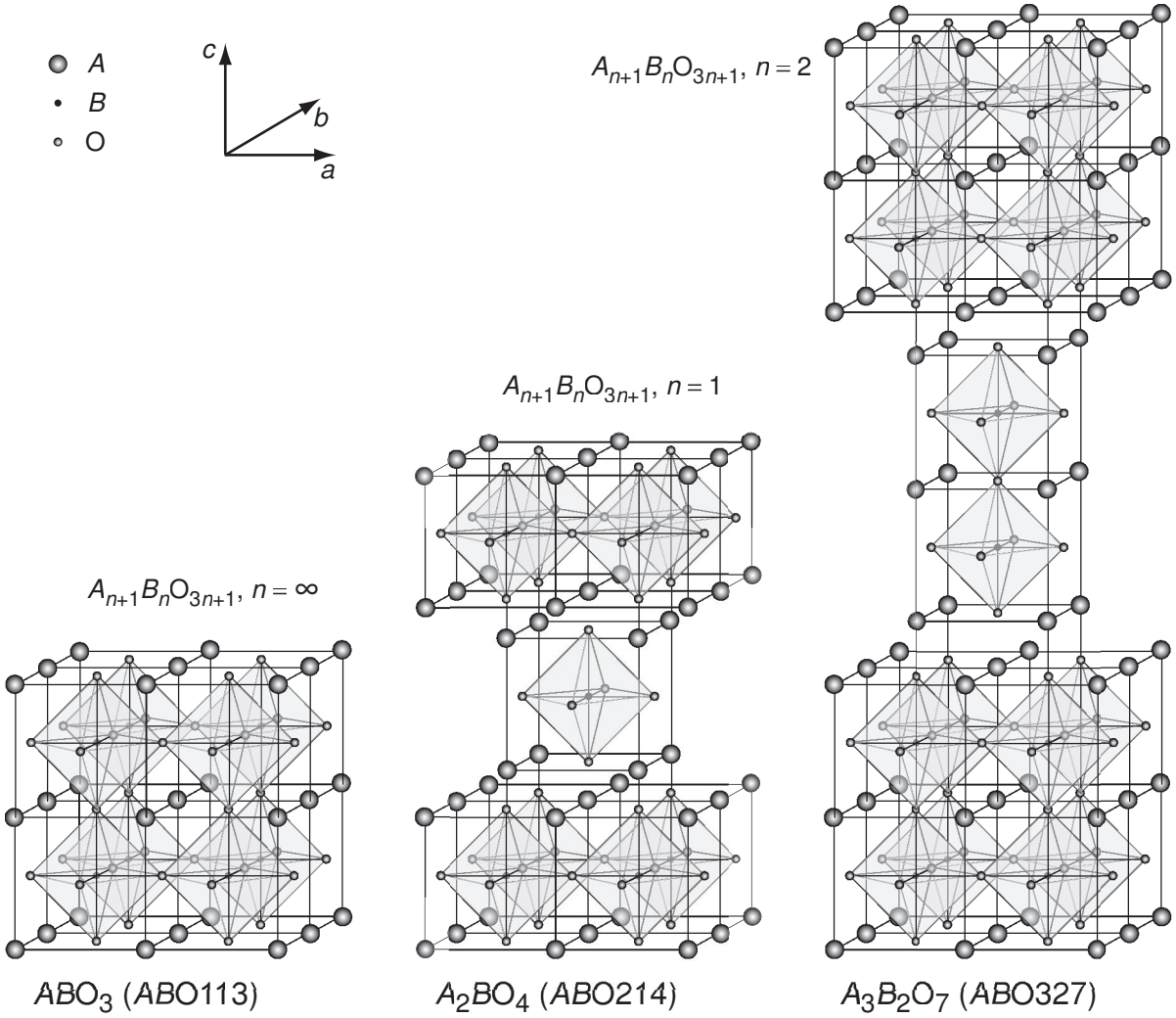

Figure 1.8: Crystal structure of the Ruddelsden-Popper series $A_{n+1}B_nO_{3n+1}$. The manganates form in both the isotropic ($n = \infty$) and the layered structures ($n \geq 1$).

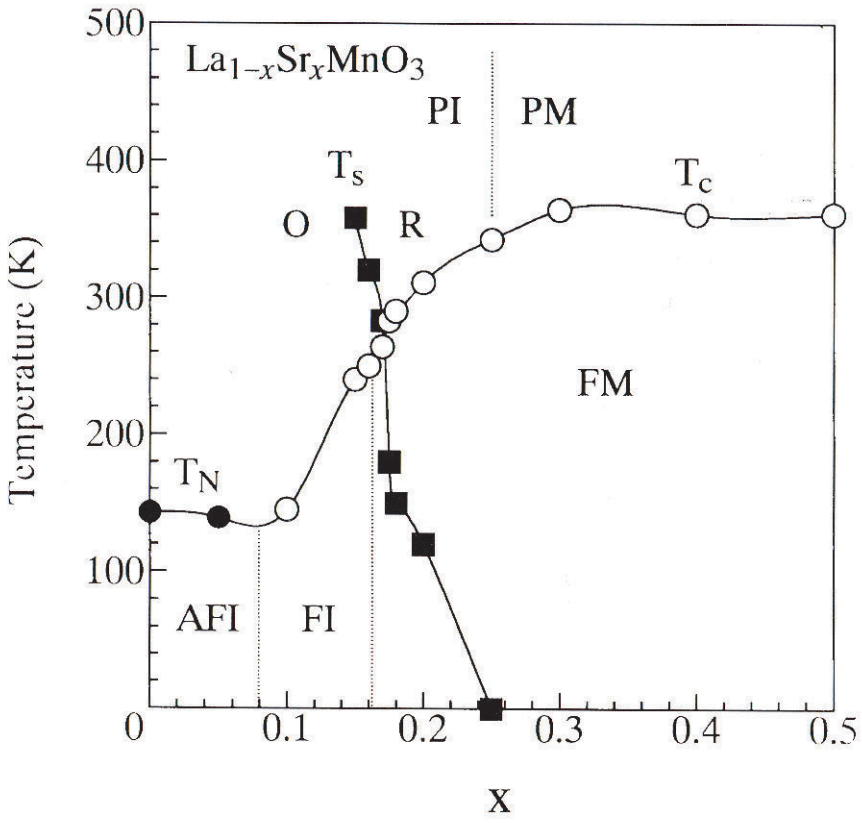

Figure 1.9: Electronic, magnetic, and structural phase diagram of $La_{1-x}Sr_xMnO_3$. Filled circles: Néel temperatures (T_N), open circles: Curie temperatures (T_C), filled squares: structural phase transition temperatures (T_s). PI: paramagnetic insulator, PM: paramagnetic metal, AFI: antiferromagnetic insulator, FI: ferromagnetic insulator, FM: ferromagnetic metal [33].

LSMO327 ($n = 2$)

LSMO327 is the main subject treated in this study. Unlike LSMO214, LSMO327 becomes metallic and ferromagnetic in the doping range $0.3 \leq x \leq 0.4$, as shown in Fig. 1.10 [33, 40]. Magnetic and electrical properties relevant to this study are shown in Fig. 1.11.

1.3.3 Mechanism of electrical conduction and colossal magnetoresistance

Zener's double exchange model is considered to constitute the main physics of electrical conduction in the manganates [33, 42]. According to this model, the ferromagnetic interaction occurs via the exchange of conduction electrons between Mn ions through O ions. The amplitude of the effective electron hopping between Mn^{3+} and Mn^{4+} (i and j sites) is expressed as

$$t_{ij} = t_{ij}^0 \cos(\theta_{ij}/2),$$

where t_{ij}^0 is the maximum hopping amplitude, and θ_{ij} the relative angle between the neighboring spins. t_{ij} depends both on the distance between Mn and O ions and on the Mn^{3+}-O-Mn^{4+} angle (Fig. 1.12).

In Mn, due to the ligand field, the electron levels are split to a high-energy e_g (conduction) electron level and a low-energy t_{2g} (core) electron level. The levels are interacting through a strong Hund coupling that aligns their spin directions. Therefore, all intra-site electrons have spins with a same direction.

Now, the mechanism of colossal magnetoresistance is explained as follows (Fig. 1.12) [33]. Taking the La-Sr-Mn-O system as example, the undoped parent compound $LaMnO_3$ is antiferromagnetic and insulator because all the sites are occupied by e_g electrons, and moreover, these have opposite spins. When the material is doped with Sr, holes are created, and the ferromagnetic state is stabilized by maximizing the kinetic energy of the conduction electrons e_g. When temperature is near T_C, the configuration of the spins is dynamically disordered. Consequently, the effective hopping interaction is reduced on average, which causes the electrical resistivity to increase. When a magnetic field is applied to align the spins, the fluctuations are suppressed, leading to an abrupt decrease in resistivity. This is why colossal magnetoresistance happens in the manganates.

1.3.4 Half metallicity and its application for spin injection experiments

Because of the strong Hund interaction between the e_g conduction electrons and the core electrons, all the conduction electron spins are aligned in the metallic ferromagnetic state. Therefore, the manganates are half-metals in this state, as shown in Fig. 1.13 [33, 43].

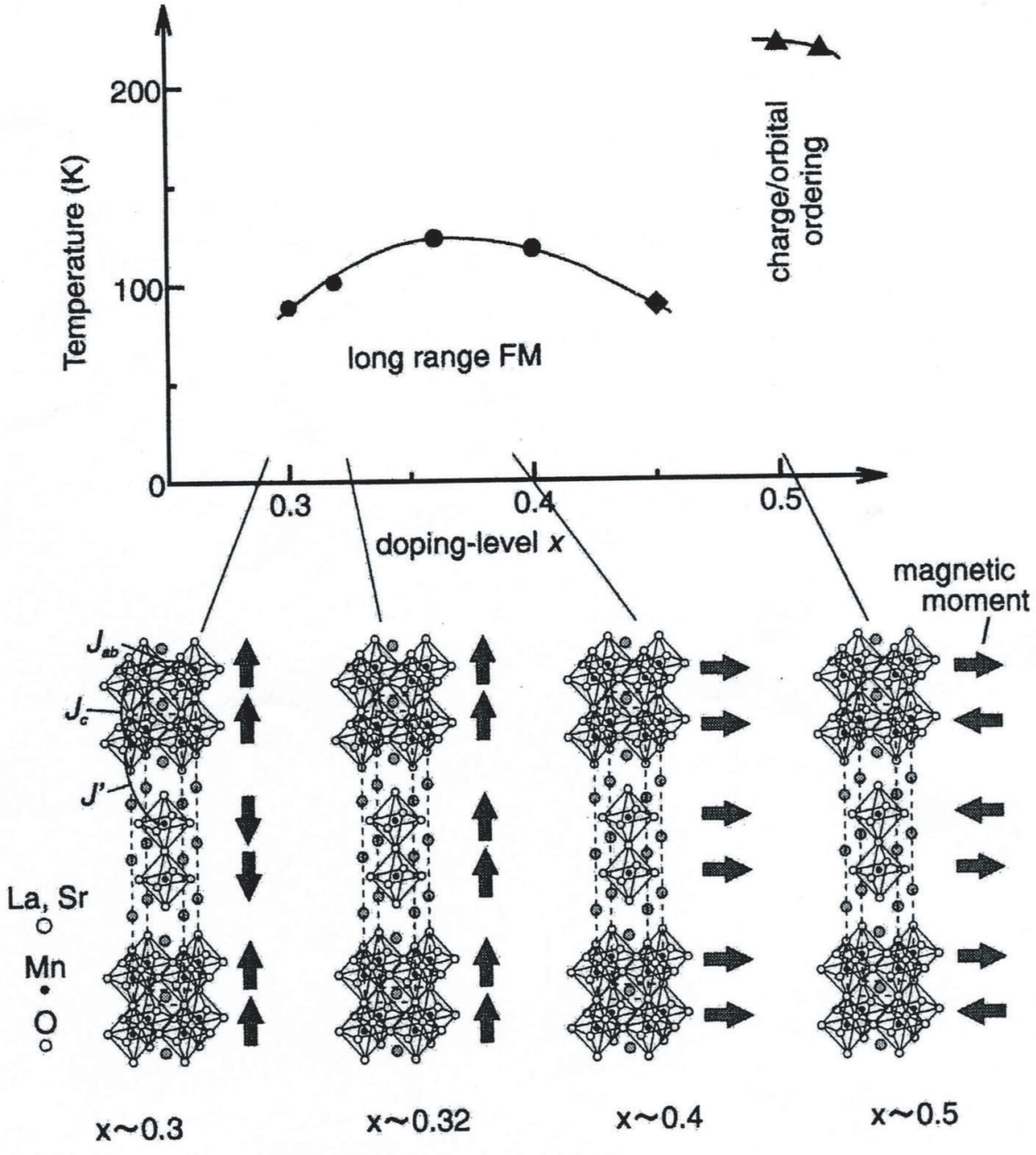

Figure 1.10: Magnetic phase diagram of $La_{2-2x}Sr_{1+2x}Mn_2O_7$ layered manganates [40].

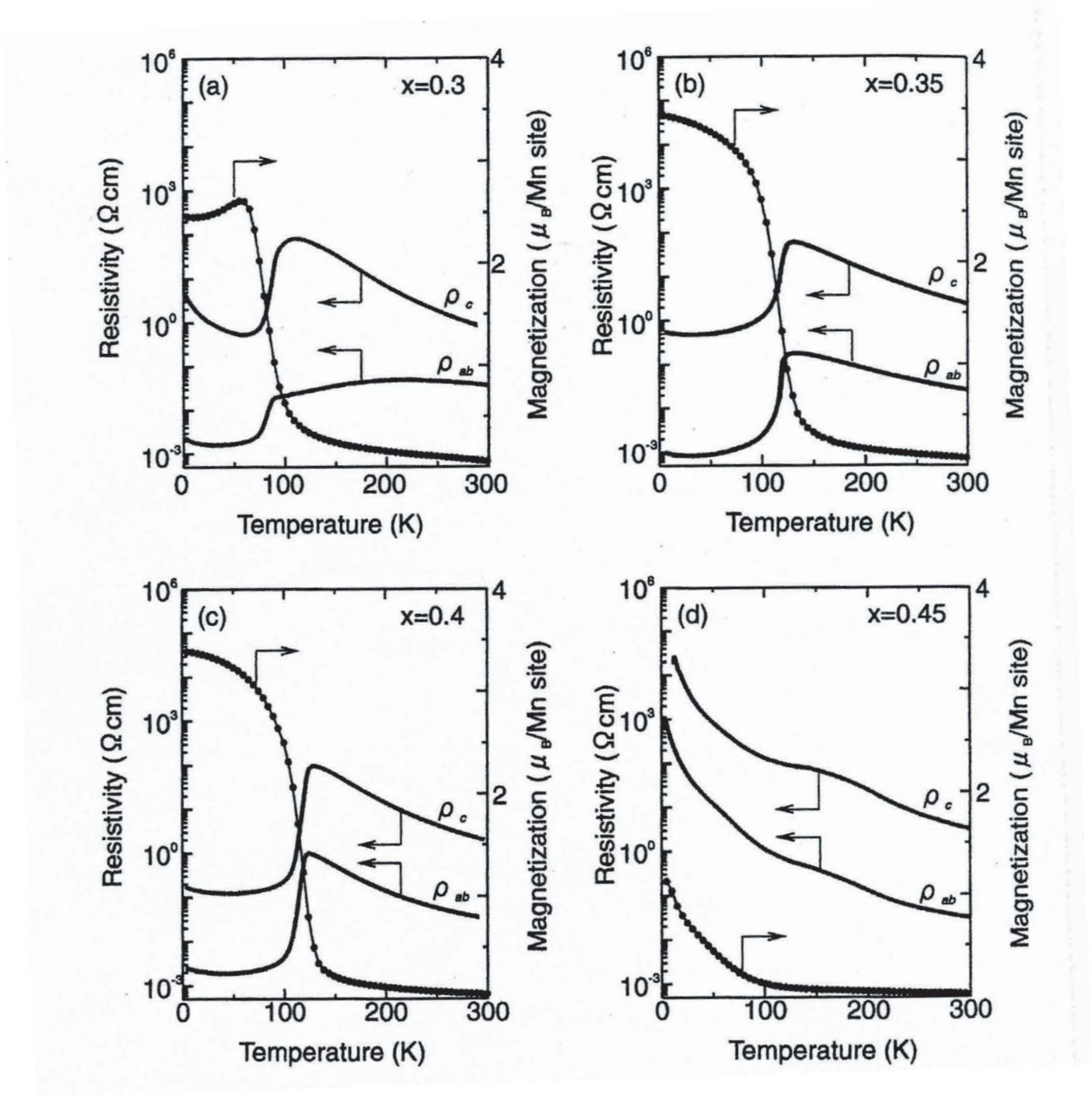

Figure 1.11: Temperature dependence of magnetization and electrical resistivity for single crystals of $La_{2-2x}Sr_{1+2x}Mn_2O_7$ layered manganates [40].

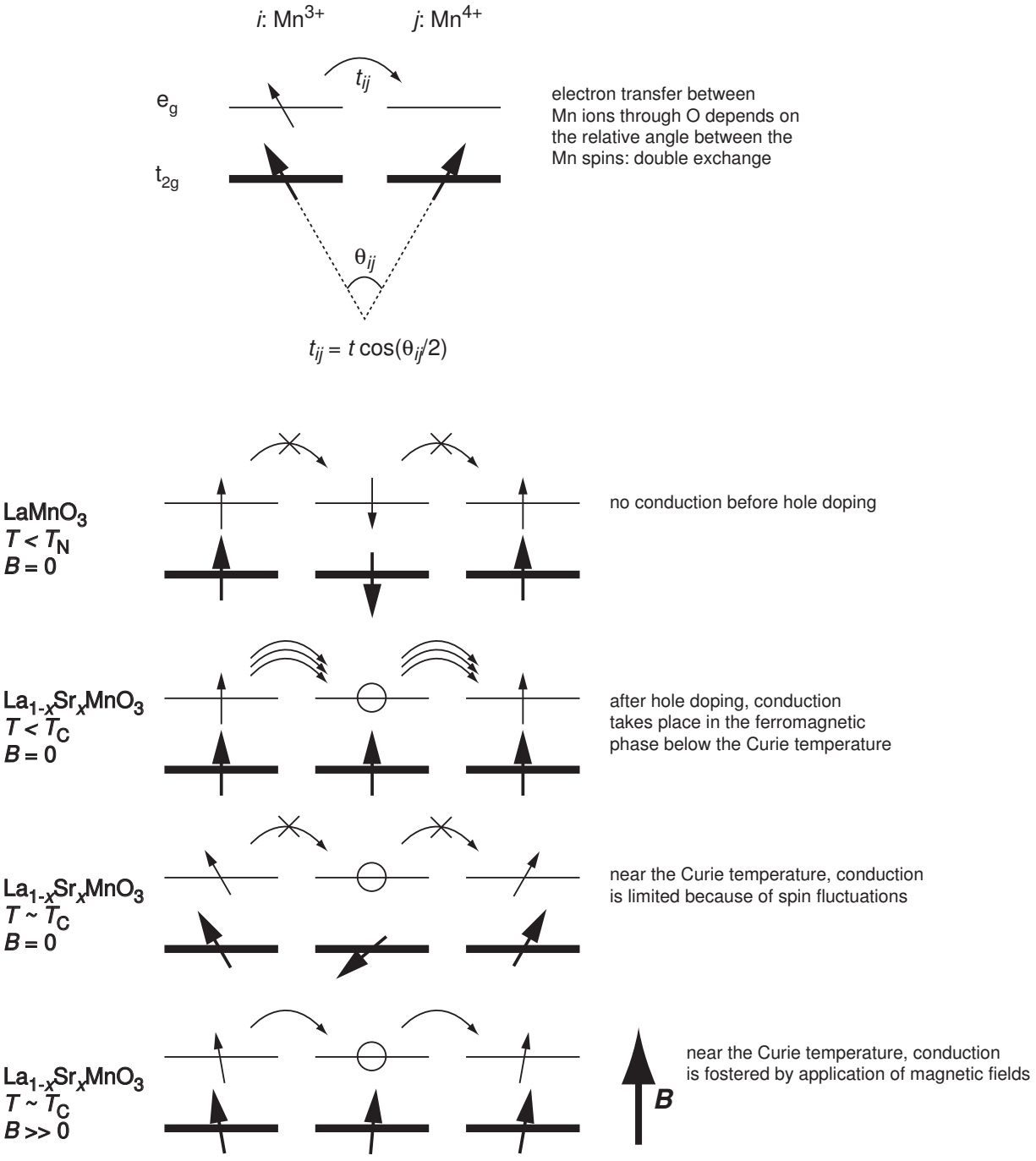

Figure 1.12: Mechanism of electrical conduction and colossal magnetoresistance in the manganate system La-Sr-Mn-O.

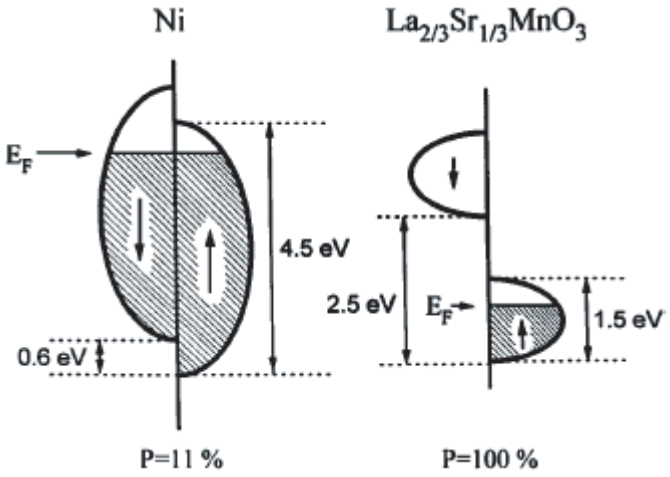

Figure 1.13: A band model of the manganates at low temperatures, compared with another for Ni. In the metallic ferromagnetic state, the spin polarization P of conduction electrons in the manganates is 100 % [43].

Experiments such as the one shown in Fig. 1.14 have also confirmed the half-metallicity of the manganates [44].

The full spin polarization of the carriers in the ferromagnetic manganates makes them attractive for studies using spin-injection experiments. Spin injection, as is understood today, started in the 70's with the important tunneling spectroscopy work of Tedrow and Meservey in ferromagnet/insulator/superconductor junctions [28]. The tunneling conductance measures single-particle tunneling and has peaks at the singularities of the density of states near the superconducting gap edge. For ferromagnetic electrodes, unlike in the case of non-magnetic ones, the tunneling conductance is asymmetric about the voltage origin $V = 0$. As the tunneling current is proportional to the density of states, analysis of the asymmetric current–voltage characteristic can determine the difference in spin-up and spin-down bands at the Fermi level. Thus, the spin polarization of conduction electrons for many ferromagnetic metals could be known.

Spin injection can be used to study also issues related to the phenomenon of superconductivity. In the standard Bardeen-Cooper-Schrieffer (BCS) model of superconductivity, the populations of spin-up and spin-down electrons are nearly equal. Local magnetic moments associated with magnetic impurities, for example, are known to suppress strongly superconductivity. If a similar effect could be obtained using spin-polarized currents, it would deepen our understanding of superconductivity (especially the not-yet understood high-T_c superconductivity) and may generate new electronic functional devices.

Spin injection is being studied also using semiconductors. The interest in semiconductors was triggered by the proposal to fabricate a spin injected field effect transistor (spin FET) using a ferromagnetic source and a similar drain [3, 22]. Many other spin-injection studies using semiconductors have been carried out, as mentioned in Section 1.1.

1.3.5 Layered manganates: colossal magnetoresistance and intrinsic spin tunneling

The manganates with the $n = 2$ layered structure are known to show intrinsic electron tunneling, such as that known in high-T_c superconductors [32, 40, 45–53]. As shown in Fig. 1.15, the ferromagnetic MnO_2 bilayers are separated by the non-magnetic insulating layers (La,Sr)O, forming a stack of magnetic tunnel junctions along the c-axis. The interfaces in these intrinsic tunnel junctions are considered to be atomically smooth, as in similar intrinsic Josephson junctions in $Bi_2Sr_2CaCu_2O_{8+\delta}$ (BSCCO) high-T_c superconductor. Owing to this property and to full spin polarization, peculiarly large magnetoresistance values have been observed in layered manganates [32, 40, 40]. In layered manganates, if the inter-bilayer coupling is antiferromagnetic, spin tunneling and electron transport are prohibited. When magnetic fields are applied to align the bilayer magnetization vectors, an abrupt decrease in resistivity occurs because spin tunneling becomes possible, leading to large values of magnetoresistance. In general, because of its spin tunneling character,

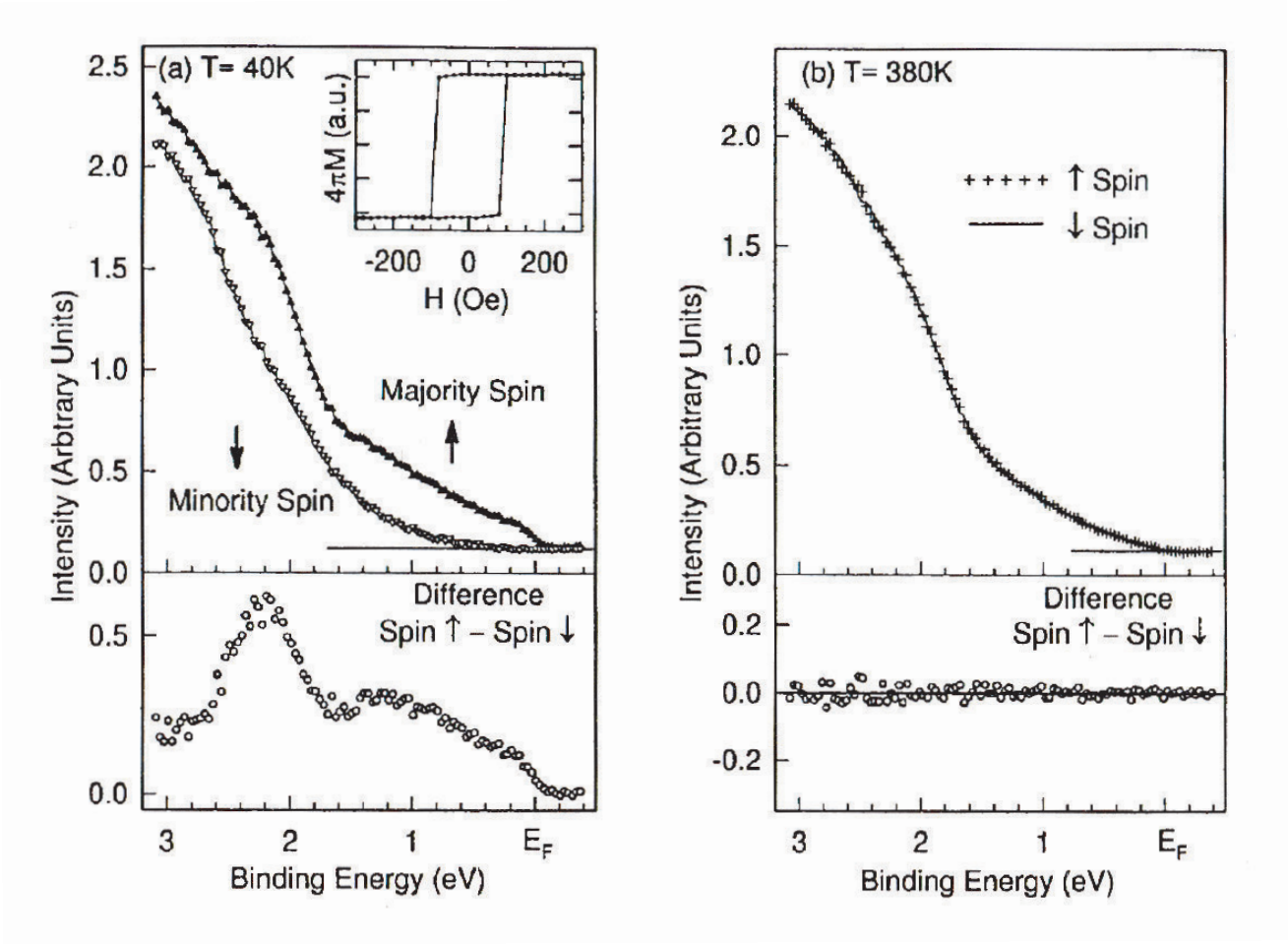

Figure 1.14: Spin-resolved photoemission spectra for a $La_{0.7}Sr_{0.3}MnO_3$ thin film with $T_C = 350$ K at (a) $T = 40$ K and (b) $T = 380$ K [44].

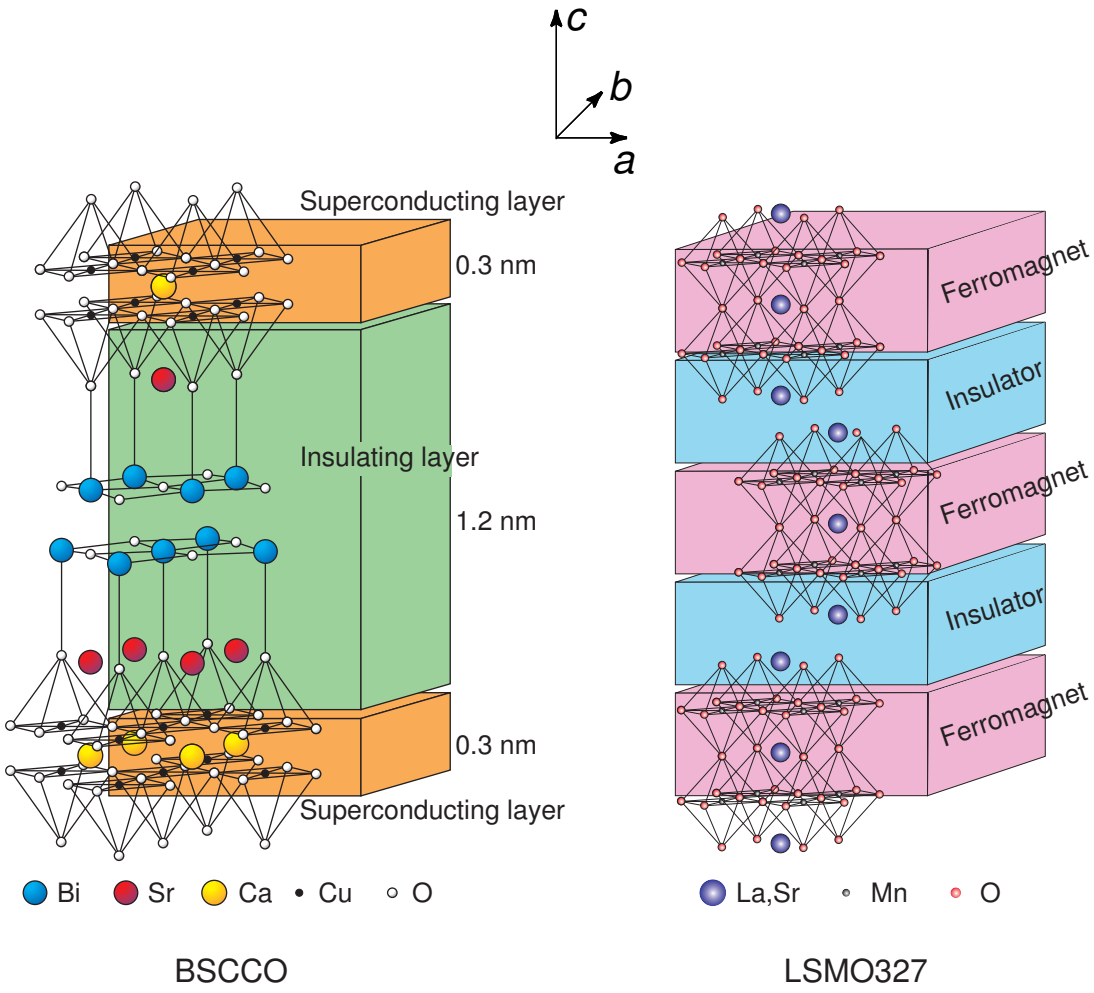

Figure 1.15: Intrinsic spin tunnel junctions in the bilayer manganate LSMO327 and intrinsic Josephson junctions in the high-T_c superconductor $Bi_2Sr_2CaCu_2O_{8+\delta}$ (BSCCO).

magnetoresistance in layered manganates does not fade away below the Curie temperature, unlike the case in isotropic manganates.

At present, spin tunneling as a phenomenon is attracting interest not only because of its successful application to magnetic recording, but also because of other newly discovered effects such as emission of microwaves and magnetization reversal by current injection [3]. Other new phenomena also may be discovered in the future.

Half-metallicity and the ideal intrinsic spin tunnel junctions that exist in layered manganates are ideal conditions for the study of spin tunneling phenomena.

1.4 Aim and Overview of this Thesis

Because it provides the opportunity to study spin tunneling in the intrinsic tunnel junctions of LSMO327, *c*-axis epitaxial growth of thin films for these layered materials is the objective of this study. This study uses sputtering for thin film growth, which has not been used yet for *c*-axis layered manganate epitaxial thin films. It also establishes a quantitative method to characterize intergrowths in these layered materials. This method and other experimental analysis are used to characterize the obtained thin films in order to assess their quality and confirm their applicability to the study of spin tunneling.

The organization of the present thesis is as follows. After a description of the used experimental methods in Chapter 2, the epitaxial growth and characterization for LSMO113 thin films is described in Chapter 3. The relationship between epitaxial thin film growth and sputtering conditions is studied. The electrical and magnetic properties of the films are characterized and the optimal epitaxial growth conditions are determined. Exploiting their full spin polarization property, LSMO113 epitaxial thin films, combined with high-T_c superconductor thin films, are used to fabricate a spin-injection device.

In Chapter 4, the *c*-axis epitaxial growth and characterization for the layered manganate $(La,Sr)_3Mn_2O_7$ are studied. The importance of controlling the deposition rate is explained. The magnetic, electrical, and magnetoresistive properties of the thin films are also characterized. Intergrowths such as LSMO113 and LSMO214 are easily incorporated into the structure of layered manganates, and therefore, a quantitative method of characterizing these intergrowths based on X-ray diffraction (XRD) experiment and simulation is developed. Based on these results, the *c*-axis epitaxial growth for the layered manganates and the properties of the grown films are discussed.

In Chapter 5, the effects of Cu-substitution of Mn on the *c*-axis epitaxial growth and the magnetic, electrical, and magnetoresistive properties of layered manganates are studied. The results are analyzed and discussed.

In Chapter 6, in order to grow better *c*-axis epitaxial layered manganate thin films with small intergrowth amounts, a new sputtering configuration is proposed. The advantages of this configuration are explained. The crystal structure of the grown *c*-axis epitaxial films

is characterized. The magnetic, electrical, and magnetoresistive characteristics are also measured, followed by a discussion of the obtained results.

Finally, in Chapter 7, the results obtained in this study are summarized with conclusions.

References

[1] P. A. M. Dirac, *The Principles of Quantum Mechanics* (Clarendon Press, 1958).

[2] N. W. Ashcroft and N. D. Mermin, *Solid state physics* (Saunders College, 1976).

[3] M. Ziese and M. J. Thornton (Eds.), *Spin Electronics* (Springer, 2001).

[4] T. Miyazaki, *Spintronics: Fundamentals for Next-Generation Memory MRAM* (Nikkan Kougyou Shimbun-sha, 2004).

[5] E. Hirota, H. Sakakima, and K. Inomata, *Giant Magneto-Resistance Devices* (Springer, 2001).

[6] G. A. Prinz, Science **282**, 1660 (1998).

[7] G. A. Prinz, J. Magn. Magn. Mater. **200**, 57 (1999).

[8] S. A. Wolf, J. Supercon. **13**, 195 (2000).

[9] S. A. Wolf, D. D. Awschalom, R. A. Buhrman, J. M. Daughton, S. von Molnár, M. L. Roukes, A. Y. Chtchelkanova, and D. M. Treger, Science **294**, 1488 (2001).

[10] A. Moser, K. Takano, D. T. Margulies, M. Albrecht, Y. Sonobe, Y. Ikeda, S. Sun, and E. E. Fullerton, J. Phys. D: Appl. Phys. **35**, R157 (2002).

[11] E. E. Fullerton, D. T. Margulies, A. Moser, and K. Takano, Sol. Stat. Tech. **44**, 87 (2001).

[12] J. R. Childress and R. E. Fontana, C. R. Phys. **6**, 997 (2005).

[13] P. J. Grundy, J. Phys. D: Appl. Phys. **31**, 2975 (1998).

[14] C. K. Lo, Y. W. Huang, Y. D. Yao, D. R. Huang, and J. H. Huang, IEEE Trans. Magn. **41**, 892 (2005).

[15] T. Osaka, T. Asahi, J. Kawaji, and T. Yokoshima, Electrochimica Acta **50**, 4576 (2005).

[16] R. C. Sousa and I. L. Prejbeanu, C. R. Phys. **6**, 1013 (2005).

[17] B. N. Engel, N. D. Rizzo, J. Janesky, J. M. Slaughter, R. Dave, M. DeHerrera, M. Durlam, and S. Tehrani, IEEE Trans. Nanotech. **1**, 32 (2002).

[18] W. Reohr, H. Hönigschmid, R. Robertazzi, D. Gogl, F. Pesavento, S. Lammers, K. Lewis, C. Arndt, Y. Lu, H. Viehmann, R. Scheuerlein, L. K. Wang, P. Trouilloud, S. Parkin, W. Gallagher, and G. Müller, IEEE Circ. Dev. Mag. **18**, 17 (2002).

[19] J. C. Slonczewski, J. Magn. Magn. Mater. **159**, L1 (1996).

[20] L. Berger, Phys. Rev. B **54**, 9353 (1996).

[21] S. I. Kiselev, J. C. Sankey, I. N. Krivorotov, N. C. Emley, R. J. Schoelkopf, R. A. Buhrman, and D. C. Ralph, Nature **425**, 380 (2003).

[22] S. Datta and B. Das, Appl. Phys. Lett. **56**, 665 (1990).

[23] H. Ohno, F. Matsukura, and Y. Ohno, Jap. Soc. Appl. Phys. Int. **5**, 4 (2002).

[24] S. Das Sarma, Amer. Scient. **89**, 516 (2001).

[25] J. M. Slaughter, R. W. Dave, M. DeHerrera, M. Durlam, B. N. Engel, J. Janesky, N. D. Rizzo, and S. Tehrani, J. Supercon. **15**, 19 (2002).

[26] E. Y. Tsymbal and D. G. Pettifor, *Solid state physics*, Vol. **56**, ed. by H. Ehrenreich and F. Spaepen (Academic Press, 2001).

[27] M. N. Baibich, J. M. Broto, A. Fert, F. Nguyen Van Dau, F. Petroff, P. Eitenne, G. Creuzet, A. Friederich, and J. Chazelas, Phys. Rev. Lett. **61**, 2472 (1988).

[28] R. Meservey and P. M. Tedrow, Phys. Rep. **238**, 173 (1994).

[29] J. S. Moodera, L. R. Kinder, T. M. Wong, and R. Meservey, Phys. Rev. Lett. **74**, 3273 (1995).

[30] R. von Helmolt, J. Wecker, B. Holzapfel, L. Schultz, and K. Samwer, Phys. Rev. Lett. **71**, 2331 (1993).

[31] S. Jin, T. H. Tile, M. McCormack, R. A. Ramesh, and L. H. Chen, Science **413**, 264 (1994).

[32] T. Kimura, Y. Tomioka, H. Kuwahara, A. Asamitsu, M. Tamura, and Y. Tokura, Science **274**, 1698 (1996).

[33] Y. Tokura (Ed.), *Colossal Magnetoresistive Oxides* (Gordon and Breach, 2000).

[34] J. Volger, Physica **20**, 49 (1954).

[35] G. H. Jonker and J. H. Van Santen, Physica **16**, 337 (1950).

[36] J. H. Van Santen and G. H. Jonker, Physica **16**, 599 (1950).

[37] G. H. Jonker and J. H. Van Santen, Physica **19**, 120 (1953).

[38] G. H. Jonker, Physica **20**, 1118 (1954).

[39] G. H. Jonker, Physica **22**, 707 (1956).

[40] T. Kimura and Y. Tokura, Ann. Rev. Mater. Sci. **30**, 451 (2000).

[41] S. Larochelle, A. Mehta, L. Lu, P. K. Mang, O. P. Vajk, N. Kaneko, J. W. Lynn, L. Zhou, and M. Greven, Phys. Rev. B **71**, 024435 (2005).

[42] C. Zener, Phys. Rev. **82**, 403 (1951).

[43] H. Y. Hwang, S. W. Cheong, N. P. Ong, and B. Batlogg, Phys. Rev. Lett. **77**, 2041 (1996).

[44] J. H. Park, E. Vescovo, H. J. Kim, C. Kwon, R. Ramesh, and T. Venkatesan, Nature **392**, 794 (1998).

[45] Y. Moritomo, Y. Tomioka, A. Asamitsu, Y. Tokura, and Y. Matsui, Phys. Rev. B **51**, 3297 (1995).

[46] H. Asano, J. Hayakawa, and M. Matsui, Phys. Rev. B **56**, 5395 (1997).

[47] T. Kimura, A. Asamitsu, Y. Tomioka, and Y. Tokura, Phys. Rev. Lett. **79**, 3720 (1997).

[48] T. G. Perring, G. Aeppli, T. Kimura, Y. Tokura, and M. A. Adams, Phys. Rev. B **58**, R14693 (1998).

[49] S. Heim, T. Nachtrab, M. Mö, R. Kleiner, R. Koch, S. Rother, O. Waldmann, P. Müller, T. Kimura, and Y. Tokura, Physica C **367**, 348 (2002).

[50] R. Kleiner, F. Steinmeyer, G. Kunkel, and P. Müller, Phys. Rev. Lett. **68**, 2394 (1992).

[51] R. Kleiner and P. Müller, Phys. Rev. B **49**, 1327 (1994).

[52] M. Suzuki, T. Watanabe, and A. Matsuda, Phys. Rev. Lett. **81**, 4248 (1998).

[53] M. Suzuki, K. Tanabe, S. Karimoto, and Y. Hidaka, IEEE Trans. Appl. Supercond. **7**, 2956 (1997).

Chapter 2

Experimental Methods

2.1 Method of Thin Film Growth

2.1.1 rf Magnetron sputtering

In sputtering (Fig. 2.1), positive ions such as Ar^+ ions are produced and accelerated to the negatively biased target (cathode). Such gas ions exist in the plasma of the same gas, which can be produced using high voltages ($\sim$ 1 kV). The positive ions possess high energies of a few 100 eV, and therefore, are able to sputter atoms from the surface of the target. Most materials have a binding energy of a few eV. The sputtered atoms diffuse until they reach a heated substrate where they react and form the film. In order to increase the plasma density for low operation pressures and high deposition rates, magnets are usually used to create magnetic fields to trap electrons and increase the ionization probability. The cathode is often driven by high frequency electric fields so that sputtering of electrically insulating materials is also possible [1, 2].

rf Magnetron sputtering is the method used to grow films in this study. The actual apparatus is shown in Fig. 2.2. An ANELVA SPF-210H on-axis rf magnetron sputtering apparatus was used (13.56 MHz, 1 kW). This apparatus uses sputtering targets of a cylindrical form with $\sim$ 7 mm in height and $\sim$ 100 mm in diameter. During sputtering, the target was cooled with circulating cold water at 10 °C. Substrates up to 30 ϕ are mountable. The distance between the target and the substrate was maintained at about 5 or 7.5 cm. A Kanthal wire of 0.7 mm in diameter and with resistance of about 23 Ω was used to raise the temperature of the substrate up to 1000 °C. A type K thermocouple (Alumel-Chromel) was inserted in a stainless steel plate of the heater block, near the place where the substrate is placed with a quartz glass plate beneath it. The substrate temperature, then, was raised by thermal radiation from the heater, carrying a current of a few amperes generated from a dc current source (Kikusui electronics Co., 160 V, 7 A). In this study, the substrate temperature is defined as the value measured by the above thermocouple before starting the sputtering process. The sputtering chamber is evacuated by a rotary pump

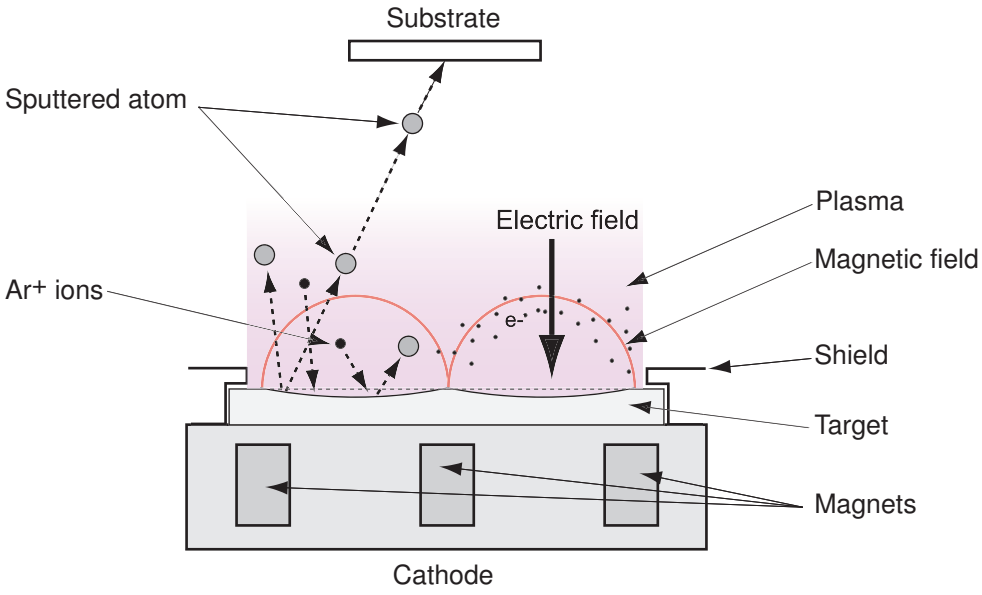

Figure 2.1: Principle of magnetron sputtering.

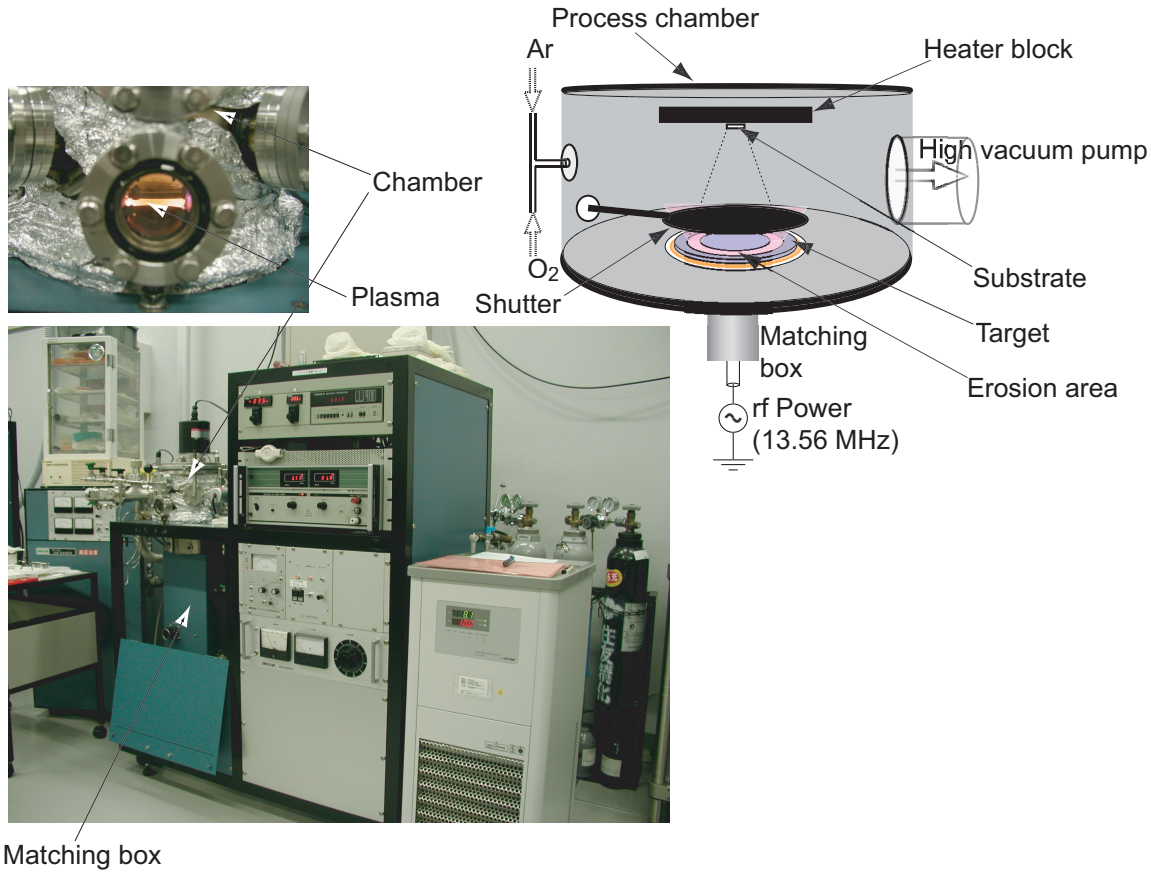

Figure 2.2: Schematic and image of the rf magnetron sputtering apparatus used in this study.

and an oil diffusion pump, typical base pressures being around 4×10^{-6} Torr. For plasma production, high purity gases of Ar and O_2 (Ar: 99.999 %, O_2: 99.8 %) were introduced into the chamber. The gas flow rate was controlled using a corresponding mass flow controller (STEC Inc.).

2.1.2 Fabrication of the sputtering target

The basic process for fabricating sputtering targets in this study is summarized in Fig. 2.3. Targets were prepared by the solid reaction technique. Appropriate molar quantities of high purity La_2O_3, $SrCO_3$, and Mn_2O_3 powders (99.9 %, Kojundo Chemical Laboratory Co.) were thoroughly mixed and then calcined at 1200 °C for 12 hours in air, using an electric furnace (Motoyama, Super-Burn 2025D). The mixture was then ground and calcined for a few times with the same conditions in order to ensure homogeneity. After this process, the calcined powder was reground and mixed with 4 % of Polyvinyl Alcohol (PVA), passed through a sieve with 420 μm cells, and finally pressed into a disk with a diameter of 100 $\sim$ 110 mm under a uniaxial pressure of $\sim$ 0.7 MPa (Riken, Co.). The disk was then sintered at 1450 $\sim$ 1500 °C for 8–100 hours in air. The result of calcining or sintering in flowing oxygen atmosphere, with the flowing rate fixed at 1 ℓ/min, was not much different from the one obtained with air when the number of regrinding times is increased.

The above process produced relatively easily stable LSMO113 targets that could be used for film growth experiments. It was not, however, sufficient to produce stable LSMO327 targets. As shown in Fig. 2.4, a residual La_2O_3 phase was found in the target after this process, which causes spontaneous destruction of the target because of the strong water absorption characteristics of La_2O_3. Stable LSMO327 targets were successfully fabricated by modifying the above process. First, the target with a diameter of 98 mm is pressed for two times in a hydraulic (oil) pressure applicator at 180 MPa (Riken, Co.). The pressing was carried out after inserting the target inside an air-evacuated and sealed plastic bag. Besides, one of the following is carried out:

1. Mn-addition to the stoichiometric target. $La_{1.4}Sr_{1.6}Mn_{2.2}O_7$ and $La_{1.4}Sr_{1.6}Mn_{2.45}O_7$ were fabricated successfully. By increasing Mn, the chance that a La_2O_3 phase remains can be made small (Fig. 2.5).

2. Cu-substitution of Mn in the stoichiometric target. Targets of $La_{1.4}Sr_{1.6}Mn_2Cu_{0.3}O_7$, $La_{1.4}Sr_{1.6}Mn_{1.8}Cu_{0.2}O_7$, and $La_{1.4}Sr_{1.6}Mn_{1.7}Cu_{0.2}O_7$ have been fabricated successfully. It is presumed that the high mobility of Cu improves the chemical reaction, and therefore, results in the reaction of all La_2O_3 (Fig. 2.6).

3. Use of a two-step fabrication process. This newly developed process consists of preparing La_2MnO_4 and Sr_2MnO_4 separately, first. The calcining process is the same as above but repeated at least five times. Then the two compositions were mixed with the addition of Mn_2O_3 to achieve the desired target composition. The mixture is pressed

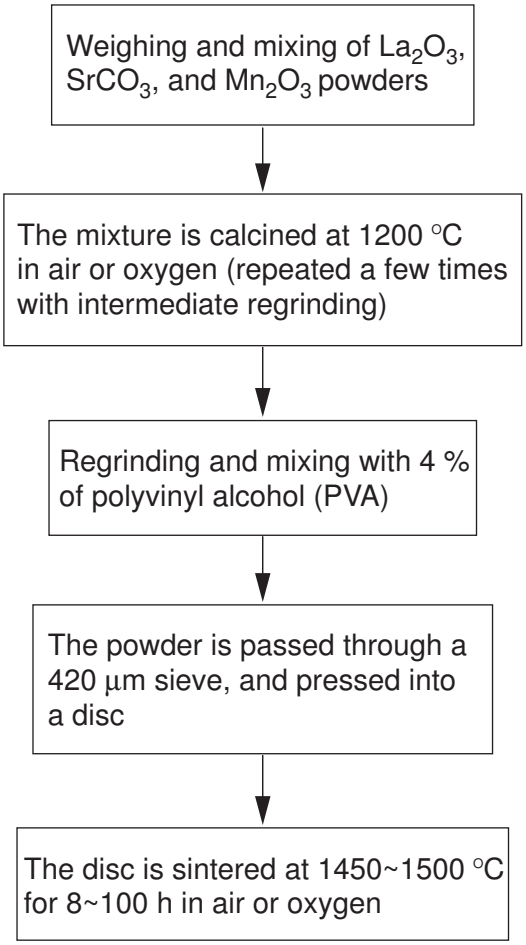

Figure 2.3: Basic process of fabrication for the sputtering target.

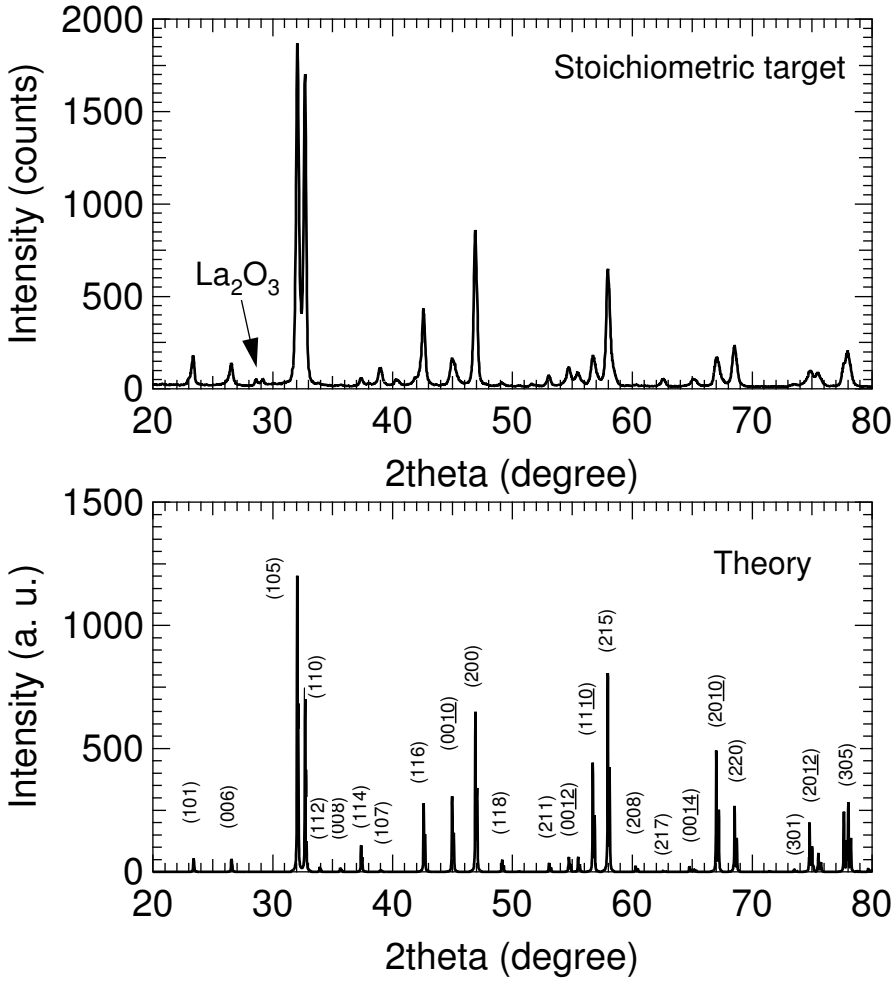

Figure 2.4: Powder XRD pattern for a $La_{1.4}Sr_{1.6}Mn_2O_7$ sputtering target containing a remanent La_2O_3 phase.

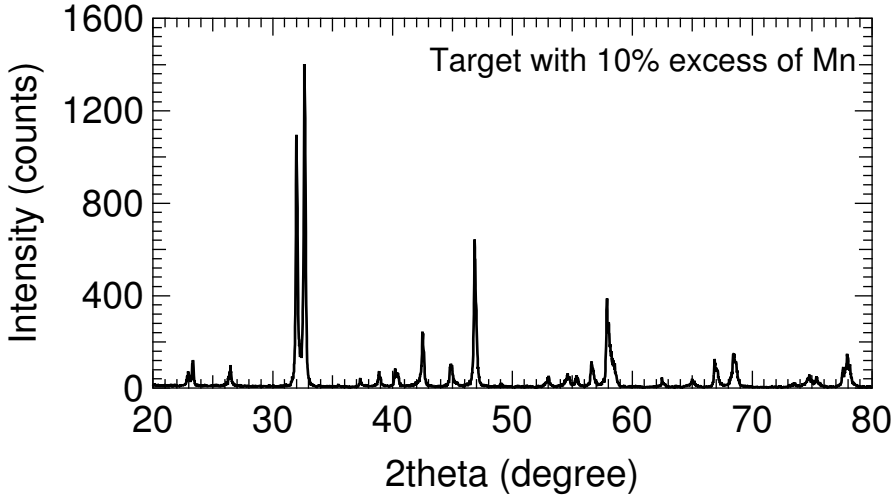

Figure 2.5: Powder XRD pattern for a sputtering target containing 10 % of Mn in excess.

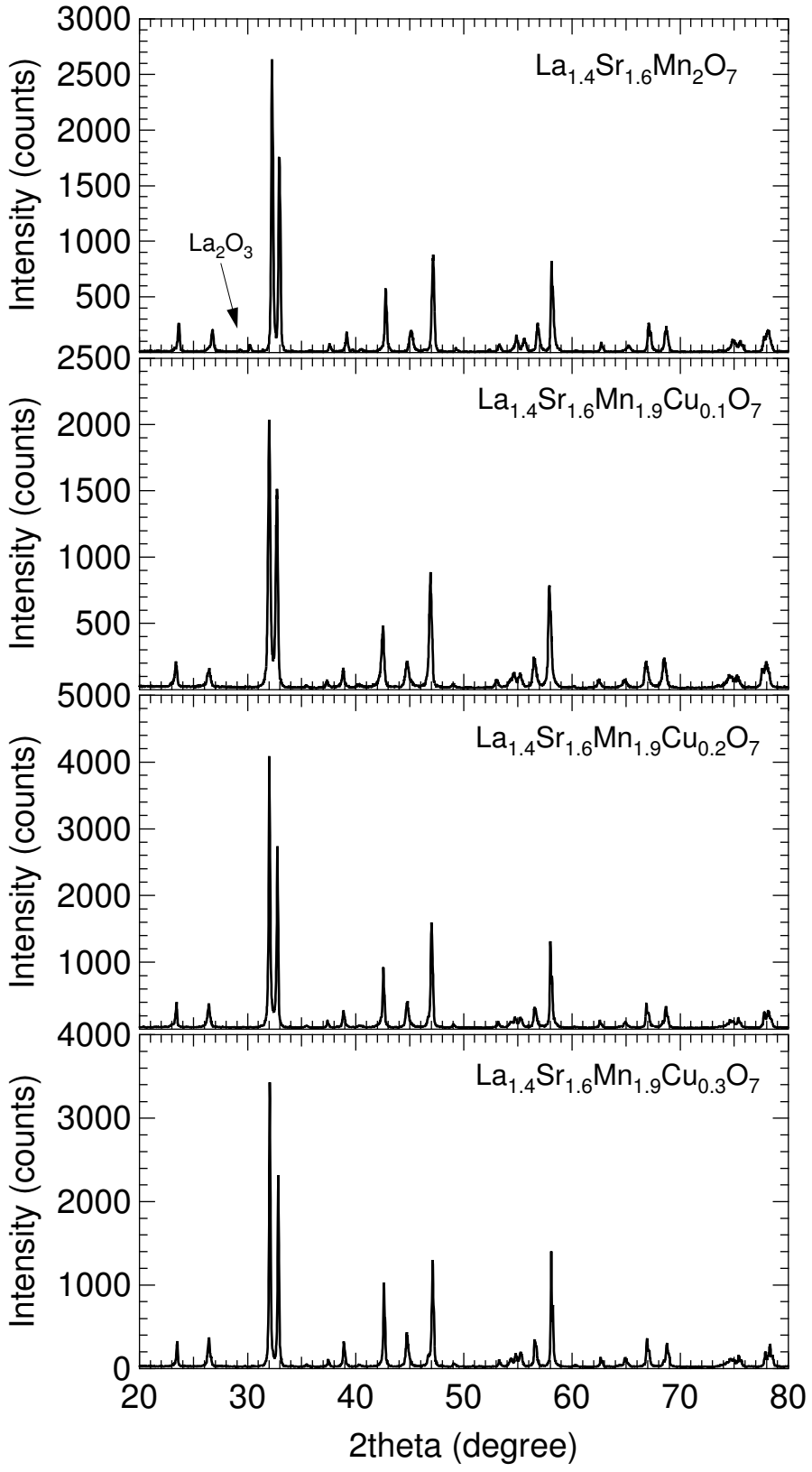

Figure 2.6: Powder XRD patterns for Cu-substituted sputtering targets.

and sintered at 1500 °C for 48 h. With this process, stable stoichiometric targets of $La_{1.4}Sr_{1.6}Mn_2O_7$ were successfully fabricated. The Mn-deficient $La_{1.4}Sr_{1.6}Mn_{1.5}O_z$ and $La_{1.52}Sr_{1.48}Mn_{1.33}O_y$ could also be fabricated (Fig. 2.7).

Before use, the targets were backed with a copper plate using a silicone bond (Toray Co., Dow Corning Silicone, JCR6101). To obtain electrical contact between the target and the copper cathode plate, it was necessary to harden the bond by heating in vacuum, at 240 °C and for 8 h.

The disc size is chosen to yield shrunk targets of $\sim$ 100 mm in diameter. The target should be flat and no greater than 7 mm in height or thickness. Table 2.1 is a list of the compositions of some successfully fabricated targets, and Fig. 2.8 shows photographs of some used targets.

2.1.3 Substrates

The kind of material for the substrate and its surface structure are imperative in epitaxial film growth. The surface should have a crystal structure similar to that of the material being grown in order to ensure its growth along that direction. Moreover, mismatches in lattice constants and thermal expansion coefficients between the film and the substrate generally induce structural changes such as strains. In this study, single crystals of $SrTiO_3$ (STO) (100) were used as substrates for the growth of manganate epitaxial thin films. STO shares the common perovskite structure with the manganates, and is suitable for epitaxial growth of these materials. The lattice constants and thermal expansion coefficients of $La_{0.7}Sr_{0.3}MnO_3$, $La_{1.4}Sr_{1.6}Mn_2O_7$, and STO are shown in Table 2.2.

Sapphire substrates (α-Al_2O_3, $(1\bar{1}02)$) were also used, but mainly for composition analysis. In the case of La-Sr-Mn-O films on STO substrates, composition analysis using the energy-dispersive X-ray spectroscopy (EDX) method is difficult for the following reasons. First, the spectral line of Sr element represents not only Sr contained in the film, but also some of that contained in the STO substrate. Second, the spectral line of La element nearly coincides with that of Ti. This renders a reliable composition analysis difficult. To get rid of these problems, La-Sr-Mn-O films were sputtered on sapphire substrates when EDX analysis was conducted. The crystal structure of sapphire is much different from that of the manganates, and as a result, all the films grown on sapphire were polycrystalline.

Before use, the substrates were inserted in an organic detergent (SCAT 20X-N) and cleaned using an ultrasound cleaner (SHARP UT-105) to remove surface contaminants. A typical image of the substrate surface cleaned in this way, taken by an atomic force microscope (AFM), is shown in Fig. 2.9.

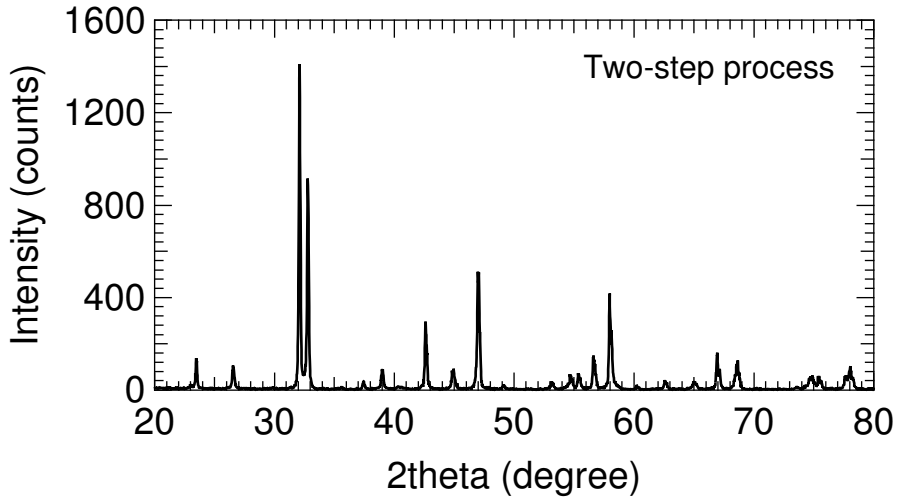

Figure 2.7: Powder XRD pattern for a $La_{1.4}Sr_{1.6}Mn_2O_7$ stoichiometric sputtering target fabricated using the two-step method.

Table 2.1: Composition of some successfully grown targets.

$La_{0.7}Sr_{0.3}MnO_{3+\delta}$	$La_{0.7}Sr_{0.34}Mn_{1.27}O_{7+\delta}$	$La_{1.4}Sr_{1.6}Mn_{2.2}O_{7+\delta}$
$La_{1.4}Sr_{1.6}Mn_{2.45}O_{7+\delta}$	$La_{1.4}Sr_{1.6}Mn_2O_{7+\delta}$	$La_{1.4}Ca_{1.6}Mn_2O_{7+\delta}$
$La_{1.52}Sr_{1.48}Mn_{1.33}O_{7+\delta}$	$La_{1.2}Sr_{1.8}Mn_2O_{7+\delta}$	$La_{1.4}Sr_{1.6}Mn_{1.5}O_{7+\delta}$
$La_{1.4}Sr_{1.6}Mn_{1.7}Cu_{0.2}O_{7+\delta}$	$La_{1.4}Sr_{1.6}Mn_2Cu_{0.3}O_{7+\delta}$	$La_{1.4}Sr_{1.6}Mn_{1.8}Cu_{0.2}O_{7+\delta}$

Figure 2.8: Photos of some targets used in this study.

Table 2.2: Lattice constants and thermal expansion coefficients of $SrTiO_3$, $La_{0.7}Sr_{0.3}MnO_3$, and $La_{1.4}Sr_{1.6}Mn_2O_7$.

	$SrTiO_3$	$La_{0.7}Sr_{0.3}MnO_3$	$La_{1.4}Sr_{1.6}Mn_2O_7$
Lattice constant a (nm)	0.390	0.388	0.387
Thermal expansion coefficient (10^{-6}/K)	11.1	11	NA

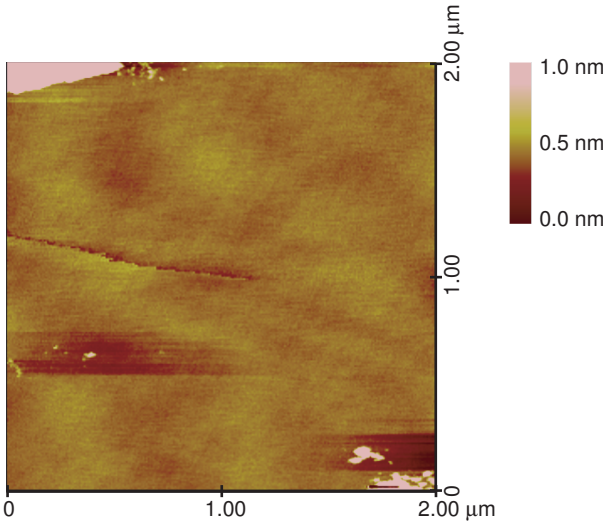

Figure 2.9: Atomic force microscopy (AFM) image of the cleaned surface of a STO (100) substrate.

2.1.4 Procedure of thin film growth

Before film deposition, the chamber was evacuated to a base pressure of approximately 4×10^{-6} Torr. Meanwhile, the substrate was heated to the desired temperature. Then, when the substrate temperature becomes stable, high purity argon and oxygen gases were introduced into the chamber with the aimed proportion. When the plasma is produced, the chamber pressure is adjusted to the desired value, and the target was presputtered for $15 \sim 20$ minutes. Then, the shutter was removed, and the film growth process was started. After sputtering, the heater power was turned off, and the film was cooled to room temperature.

Post-annealing was carried out ex-situ in an atmosphere furnace at temperatures near 900 °C for several hours in flowing oxygen (1 ℓ/min). Further details on the film treatment after deposition are indicated in the experimental descriptions included in each chapter.

2.2 Film Characterization Methods

2.2.1 Thickness measurement

The film thickness was determined with a stylus profilometer at a step edge made by chemical etching. The used etchant was a mixture of H_2O, HCl, and HNO_3 (1:2:2).

2.2.2 Composition analysis: energy-dispersive X-ray spectroscopy (EDX)

When a beam of suitably accelerated electrons hit the film surface, it ionizes the atoms. In the process, electrons in the inner shells are expelled, and the vacancy is then filled with an electron of outer shells. These electrons have higher energies than the inner shell electrons, and therefore, release the remaining energy by emitting X-rays (Fig. 2.10). These X-rays are characteristic to the atoms present in the film. Therefore, by measuring the intensity of the specific X-rays generated, the quantity of each element in the film can be calculated. In EDX, this is used to analyze the chemical composition of the film [3, 4].

The apparatus used in this study was an EDX analyzer mounted in a scanning electron microscope. The electron acceleration voltage was fixed at 20 kV. EDX was performed on films grown on sapphire (R-plane) substrates for the reasons mentioned in Section 2.1.3.

For quantitative composition analysis, the ZAF method was used. In principle, this method is accurate only for sufficiently thick specimens, and therefore, corrections for thin films are necessary [3, 4]. In this study, the as-observed composition for films thinner than 300 nm needed to be corrected. The data used for the correction is shown in Fig. 2.11.

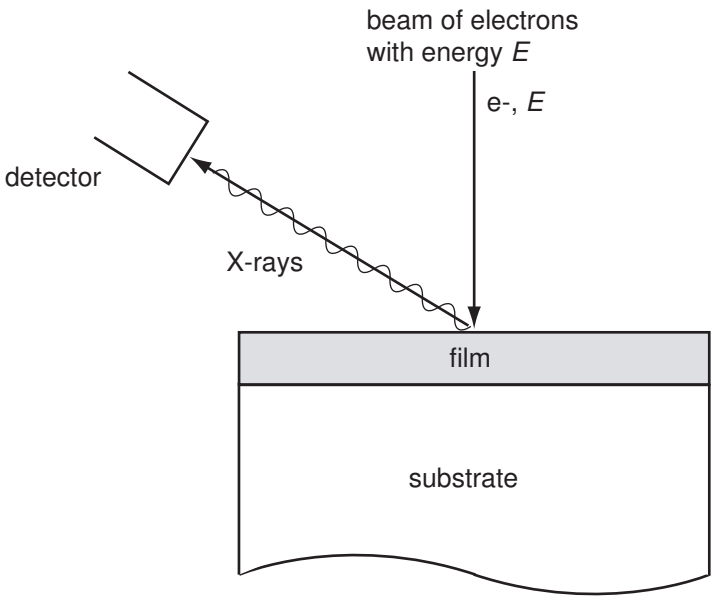

Figure 2.10: Principle of energy-dispersive X-ray spectroscopy (EDX).

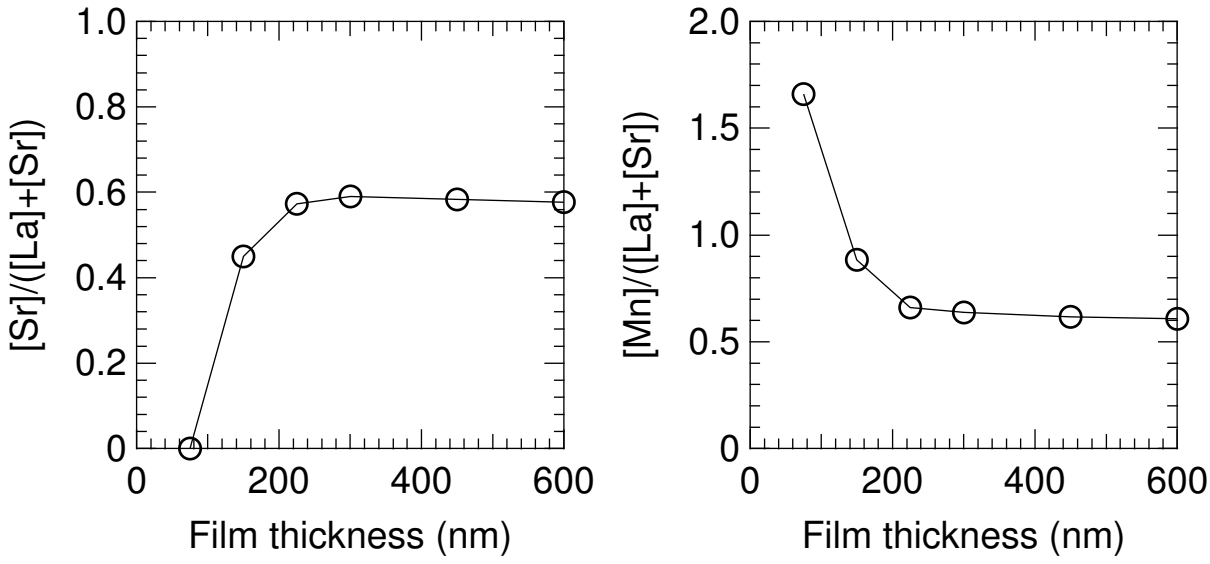

Figure 2.11: Data used for EDX correction in the case of thin La-Sr-Mn-O films.

2.2.3 Structure analysis: X-ray diffraction (XRD)

When X-rays are incident on (hkl) planes (h, k, l are integers) of a crystal, they interfere constructively when the Bragg relation holds (Fig. 2.12) [5]. Namely,

$$2d\sin\theta = n\lambda, \ (n : \text{integer}) \tag{2.1}$$

where d is the distance between successive (hkl) planes, θ is the angle between the crystal plane and X-rays, and λ is the wavelength of the X-rays. Therefore, strong X-rays signals are observed at the θ angles that satisfy Eq. (2.1). By scanning θ and determining its value at the XRD peaks, the value for d and the orientation of the film are determined.

In the case of polycrystalline materials, θ scans yield all the XRD peaks for all combinations of (hkl). Therefore, the crystal structure of the material can be determined. Such powder XRD experiments were carried out for bulk samples, such as sputtering targets, in order to identify their crystal structure and to check if they include other impurity phases.

In this study, a Rigaku X-ray diffractometer apparatus was used (RINT-2200VHF). The power used for the XRD experiments was 1.2 kW.

2.2.4 Surface analysis: high resolution scanning electron microscopy (HRSEM)

The principle of surface analysis conducted in this study using scanning electron microscopy is shown in Fig. 2.13. High-energy electrons interact with the film surface and generate many other secondary electrons. These electrons are attracted by a positively biased detector that measures the quantity of the generated electrons. Only those secondary electrons that are produced within a very short distance from the surface are able to escape from the sample. At edges on the sample surface, the quantity of the produced secondary electrons increases, and therefore, is used to generate an image of the surface morphology [6].

Because electrons impinge inside, the charge accumulates in samples that have low electrical conductivities. Therefore, the surface can not be observed clearly with SEM. In this case, about 7 nm of Au was evaporated onto the film surface.

In this study, a high resolution field emission scanning electron microscope (JSM-6500F, JEOL Co.) was used. Magnifications as high as $\times 50,000$ were routinely reached.

2.2.5 Magnetization measurement

Magnetization measurements were made with a superconducting quantum interference device (SQUID) magnetometer (Magnetic Property Measurement System, MPMS5, Quantum Design Co.). A measurement is made by moving a sample through superconducting detection coils. As the sample moves through, the magnetic moment of the sample induces an electric current in the coils. Because these coils, the connecting wires, and the SQUID

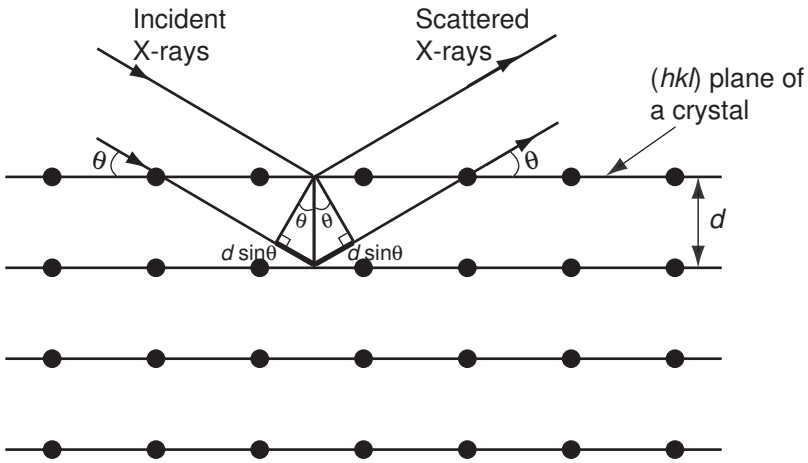

Figure 2.12: Principle of X-ray diffraction (XRD) structure analysis.

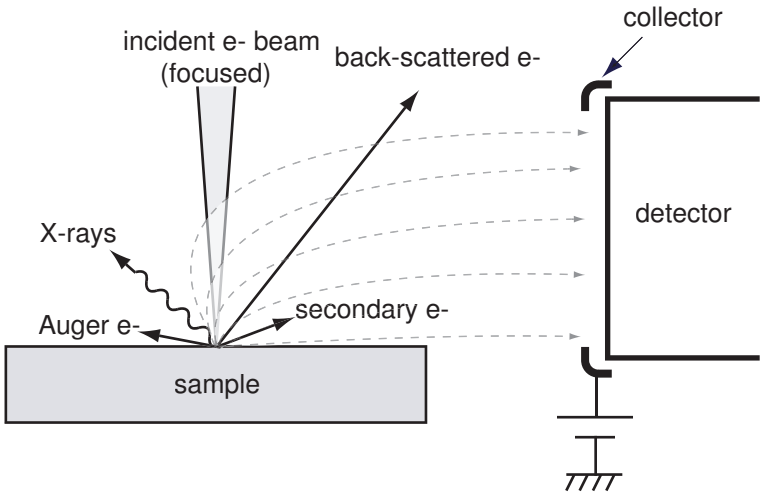

Figure 2.13: Principle of scanning electron microscopy (SEM). The quantity of secondary electrons depends on the surface topography.

input coil form a closed superconducting loop, any change of magnetic flux in the detection coils produces a change in the persistent current in the detection circuit. This change is proportional to the change in magnetic flux. Since the SQUID circuit functions as a highly linear current-to-voltage converter, variations in the detection coil's current produce corresponding variations in the SQUID output voltage, which are proportional to the magnetic moment of the sample (Fig. 2.14) [7].

The sensitivity of the instrument is approximately 1×10^{-8} emu. In this study, the magnetization measurements were carried out under applied magnetic fields of $0.5 \sim 1$ T, parallel to the film surface. The sample was fixed on the up-down sweeping holder with an adhesive (Insulating Varnish and Adhesive, General Electric Co.). The contribution from the substrate was subtracted based on dummy measurements.

For the samples showing a ferromagnetic transition, the Curie temperature T_C was determined by the $M^2 - T$ method. According to the mean field theory of ferromagnetism, $M^2 \propto T_C - T$ at temperatures close to T_C [5]. Therefore, M^2 is plotted against T and T_C is determined from the point of intersection of the T axis and the tangent to the plot near T_C.

2.2.6 Resistivity and magnetoresistance measurement

The dc resistivity was measured by the four probe method. Ag leads with 50 μm in diameter were placed on the surface of the sample using a conducting paste (Epoxy Technology Co., H20E part A, B). The lead contacts were subsequently hardened at 350 °C in air for 15 min. The measurements were carried out in a Physical Property Measurement System (PPMS, Quantum Design Co.) that is automatized with a Labview software (Fig. 2.15). The experiments were carried out in the 10–300 K temperature range in the presence of magnetic fields ranging from 0 to 9 T. Temperatures as high as 400 K were also accessible but in 0 magnetic field only, using a custom-made warmable assembled system that includes a Pt resistance for the temperature measurement. Typical injected currents were 0.1–10 μA for all the resistivity measurements. The system used could measure resistances up to 1 MΩ. The magnetoresistance was calculated as $-\Delta\rho/\rho_0 = -[\rho(B) - \rho(0)]/\rho(0)$, where ρ is the resistivity and B is the magnetic field.

References

[1] K. Wasa and S. Hayakawa, *Thin Film Technology* (Kyoritsu Publishing, Tokyo, 2002).

[2] B. Chapman, *Glow Discharge Processes* (John Wiley & Sons, Inc., New York, 1980).

[3] J. I. Goldstein, D. I. Newbury, P. Echlin, D. C. Joy, C. Fiori, and E. Lifshin, *Scanning Electron Microscopy and X-ray Microanalysis* (Plenum Press, New York and London, 1981).

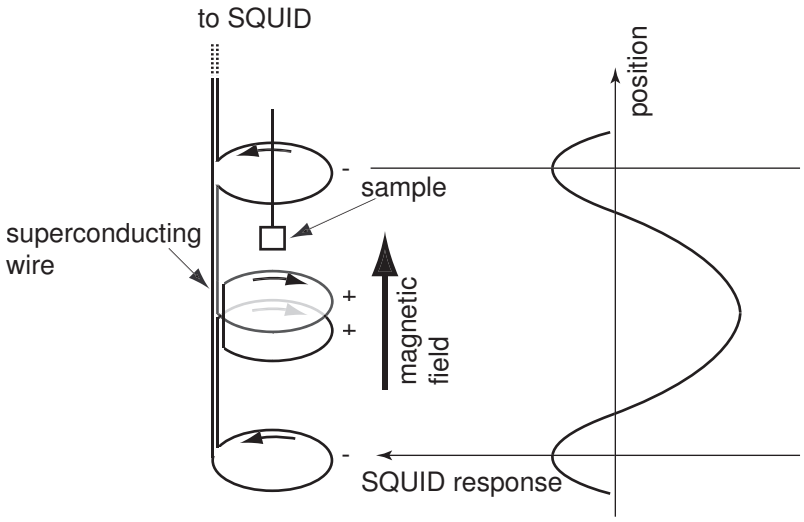

Figure 2.14: Principle of magnetization measurement using a superconducting quantum interference device (SQUID).

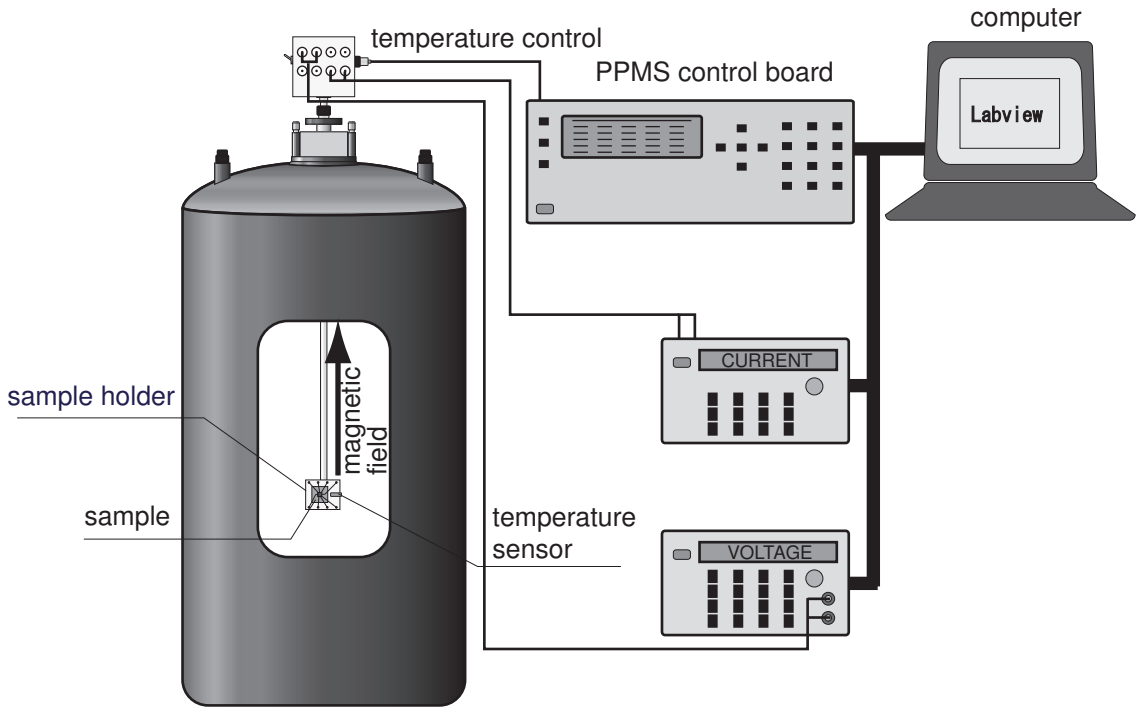

Figure 2.15: Setup for measurement of electrical resistivity and magnetoresistance.

[4] J. I. Goldstein, D. I. Newbury, P. Echlin, D. C. Joy, C. Fiori, and E. Lifshin, *Introduction to Analytical Electron Microscopy* (Plenum Press, New York, 1979).

[5] N. W. Ashcroft and N. D. Mermin, *Solid state physics* (Saunders College, 1976).

[6] *JSM-6500F High Resolution Scanning Electron Microscope: User's Manual*, JEOL Corporation.

[7] *Magnetic Property Measurement System (MPMS5): User's Manual*, Quantum Design Corporation.

Chapter 3

Epitaxial Growth and Characterization of $La_{1-x}Sr_xMnO_3$ Thin Films

3.1 Introduction

This study focuses on the bilayer manganates $(La,Sr)_{n+1}Mn_nO_{3n+1}$ with $n = 2$. In general, the layered manganates have crystal structures that are more complicated than the non-layered LSMO113 ($n = \infty$). In fact, LSMO113 is the most stable structure in the manganate system and forms easily under a wide range of conditions [1, 2]. An understanding of the properties of LSMO113 would be helpful when one will analyze the characteristics of other structures. This turns out to be the case as will be clear in the following chapters. It is mainly from this perspective that the study of LSMO113 epitaxial thin films has been undertaken, and it is the main subject of the present chapter.

$La_{1-x}Sr_xMnO_3$ also shows full spin polarization of the conduction electrons [1]. This property can be exploited to make electronic spin devices such as the ferromagnetic/superconductor spin injection device. A device of this type has been also fabricated and is discussed in Section 3.5.

3.2 Epitaxial Growth of $La_{1-x}Sr_xMnO_3$ Thin Films

The epitaxial growth of any material can be guided by the following three principles. Namely, stoichiometry of the chemical composition must be achieved in order to obtain the phase concerned. Then, an appropriate substrate temperature must be provided so that the chemical reaction between the different species to occur. Finally, a substrate with an orientation and a small lattice-mismatch must be chosen in order to achieve the desired directional growth [3].

For LSMO113 in the present study, the doping level $x = 0.3$ is targeted because it shows a Curie temperature of ~ 370 K, the highest in the system [1].

3.2.1 Conditions of thin film growth

La-Sr-Mn-O films were grown by on-axis rf-magnetron sputtering on $SrTiO_3$ (100) (STO) substrates at temperatures T_{sub} between 650 and 820 °C. 820 °C is the maximum temperature reached in the sputtering apparatus before the heater reconstruction made when the growth of LSMO327 was undertaken. Sputtering targets of stoichiometric $La_{0.7}Sr_{0.3}MnO_3$ and Mn-rich $La_{0.7}Sr_{0.34}Mn_{1.27}O_3$ were used. They were prepared by the simple solid state reaction method described in Chapter 2. The sputtering atmosphere was maintained at (Ar 70 %, O_2 30 %) with a total pressure of 1.3×10^{-2} Torr for the stoichiometric target, or 8×10^{-2} Torr for the Mn-rich target. The rf power was set at about 3 W/cm^2, and the substrate-target distance fixed at 4.5 cm. The film thickness was 180 nm for all films. The deposition rate is estimated to be around 25 nm/min. Post-treated films have been either cooled in 700 Torr of oxygen immediately after growth, or annealed for 2 hours in flowing oxygen at 900 °C.

3.2.2 Dependence of film composition on sputtering conditions

The results of EDS composition analysis performed on LSMO113 thin films grown on sapphire substrates are summarized in Table 3.1. It is seen that films sputtered from the stoichiometric target at the pressure 80 mTorr suffer from a Mn deficiency in excess of 20 %, while La and Sr contents are almost the same as the target values. This decrease in Mn content can be explained by an asymmetric scattering of the sputtered atoms by the Ar gas particles, the lighter Mn being more strongly scattered than La and Sr. Indeed, decreasing the chamber pressure resulted in more Mn incorporation into the films. At the pressure of 13 mTorr, the Mn content was nearly stoichiometric within the analysis error. We have also found that the cation (La, Sr, and Mn) compositions of films grown at different temperatures are almost identical. Films with nearly the stoichiometric composition were grown at 80 mTorr also using the Mn-rich target $La_{0.7}Sr_{0.34}Mn_{1.27}O_3$ to compensate for the Mn deficiency. Similar results were obtained for both kind of films.

3.2.3 Characterization of crystal structure

Figure 3.1 shows a typical XRD pattern for the LSMO113 epitaxial thin films grown in this study. The pattern shown is for a stoichiometric film grown at $P_s = 80$ mTorr and $T_{sub} = 820$ °C. Only the $(\ell 00)$ diffraction peaks are seen, which indicates that the films grew with the [100] direction perpendicular to the substrate plane. The film surface is also smooth as revealed by the streaky pattern observed in the RHEED image of the film, shown in Fig. 3.2.

Table 3.1: Relationship between the film composition and the sputtering pressure P_s for different target compositions.

Sputtering target	Chamber pressure	Film composition
$La_{0.7}Sr_{0.3}MnO_3$	80 mTorr	$La_{0.73}Sr_{0.27}Mn_{0.78}O_{3-\delta}$
$La_{0.7}Sr_{0.3}MnO_3$	13 mTorr	$La_{0.7}Sr_{0.3}Mn_{0.95}O_{3-\delta}$
$La_{0.7}Sr_{0.34}Mn_{1.27}O_3$	80 mTorr	$La_{0.7}Sr_{0.3}MnO_{3-\delta}$

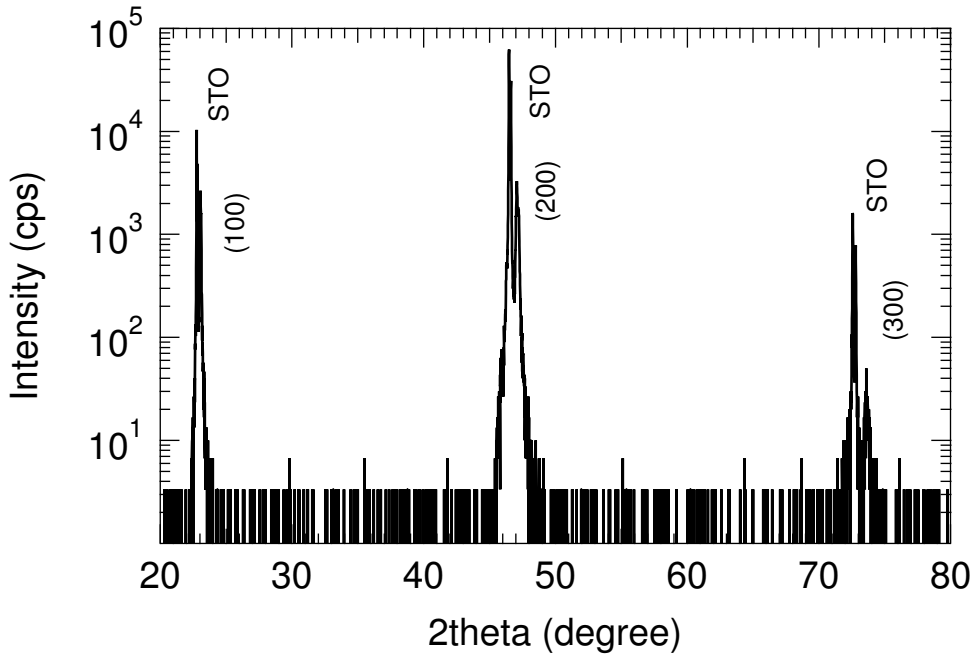

Figure 3.1: Typical XRD pattern for $La_{0.7}Sr_{0.3}MnO_{3-\delta}$ epitaxial thin films grown in this study. The pattern shown is for a film grown at $P_s = 80$ mTorr and $T_{sub} = 820\,^{\circ}C$.

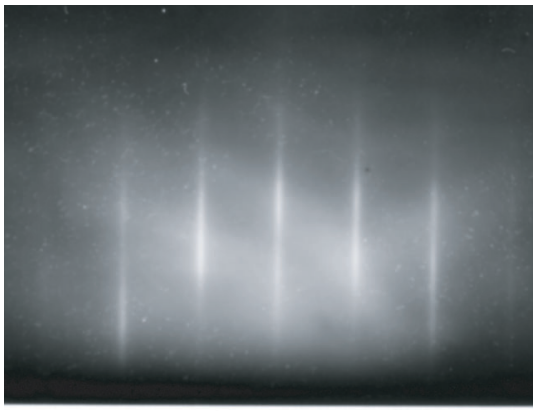

Figure 3.2: Observed RHEED pattern for a $La_{0.7}Sr_{0.3}MnO_{3-\delta}$ epitaxial thin film grown at $P_s = 80$ mTorr and $T_{sub} = 820\,^{\circ}C$ on STO.

The out-of-plane lattice constant, as calculated from the position of the XRD peaks using the Nelson-Riley method, depended on the substrate temperature at which the film was grown. The results are shown in Fig. 3.3. The lattice constant is seen to drop proportionally as the substrate temperature is increased. At 650 °C, its value was 0.391 nm, and at 820 °C, it decreased to 0.387 nm, which is nearly equal to the bulk value of 0.388 nm for the $La_{0.7}Sr_{0.3}MnO_3$ bulk. Because the lattice constant of the manganates depends sensitively on many factors, a precise explanation of this result is difficult. However, possible explanations are as follows. First, as no change in the cation content could be discerned, the observed variation in lattice constant with growth temperature cannot be explained in terms of a change neither in the doping level (Sr content) [4] nor in the Mn content [5]. Next, the possibility of a change in the oxygen content is considered. It has been reported [6] that the lattice constant of a manganate film decreases rapidly with increasing amount of the incorporated oxygen. However, this possibility is very improbable in the present case, because the oxygen content would normally decrease when the growth temperature is raised. Finally, the above results can be explained by a decrease in the density of crystal defects, such as stacking faults, with increasing growth temperature. This is similar to some reported results obtained for high-T_c superconductor films [7].

3.3 Magnetic, Electrical, and Magnetoresistive Characterization

3.3.1 Temperature dependence of magnetization and electrical resistivity

The magnetization of the grown LSMO113 films was measured in the presence of a 0.5 T field applied parallel to the film plane. Figures 3.4 and 3.5 show the temperature dependence of magnetization and electrical resistivity for films grown at different temperatures. It is seen that the effects of the substrate temperature during film growth on the electrical and magnetic properties are large. Films grown at temperatures as low as 700 °C have small magnetization and T_C, and their resistivities show semiconducting behavior in the whole temperature range measured. In contrast, films grown at higher temperatures have lower resistivities and improved ferromagnetism with higher Curie temperatures. Above T_{sub} = 770 °C, the ferromagnetic transition appears also as a sudden decrease in the electrical resistivity characteristics.

At this point, the LSMO113 films grown at 820 °C, however, showed resistivities about one order of magnitude higher than those of $La_{0.7}Sr_{0.3}MnO_3$ single crystals, with Curie temperatures smaller than the bulk value by more than 100 K. The magnetization at low temperatures is also found to be approximately 20 % smaller than the value expected from full polarization of Mn ions (3.7 μ_B/Mn). This is considered to be a consequence of oxygen

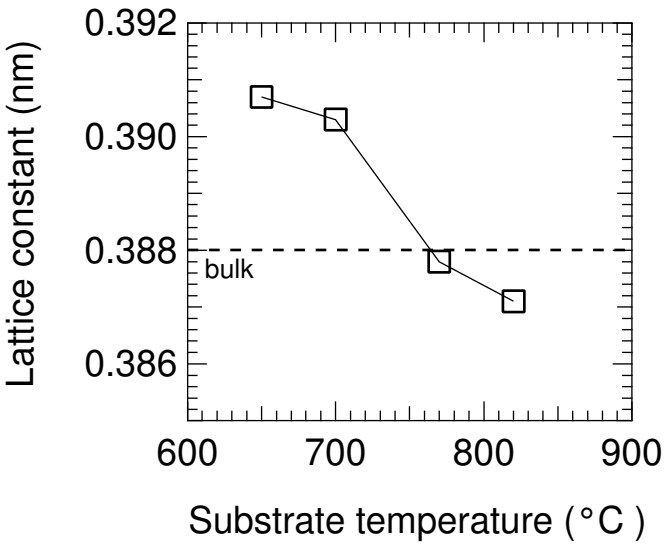

Figure 3.3: Dependence of the lattice constant on substrate temperature for LSMO113 epitaxial thin films.

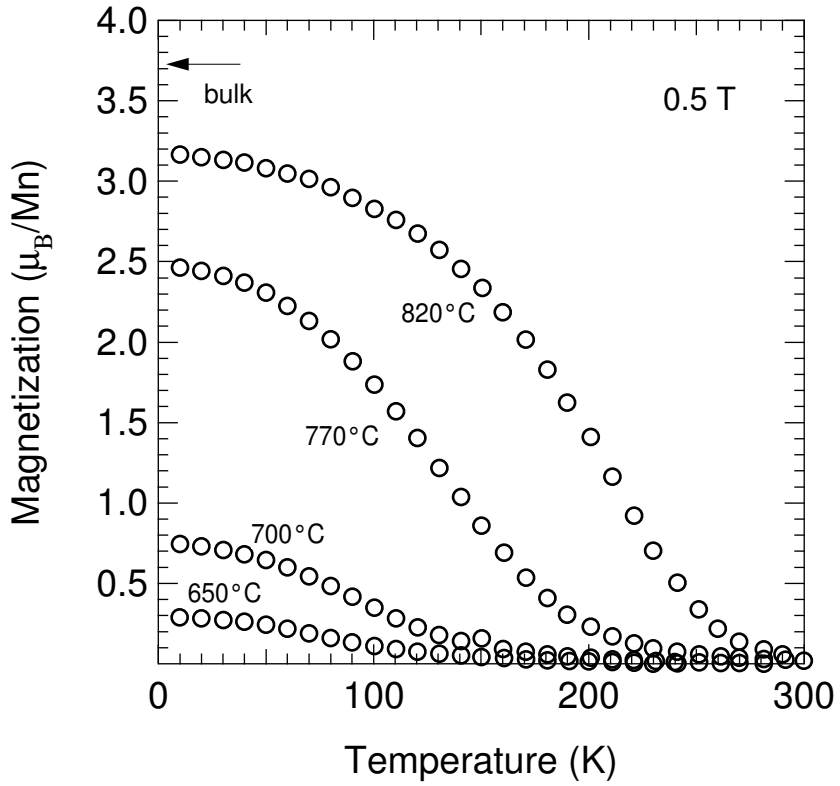

Figure 3.4: Temperature dependence of magnetization for as-grown LSMO113 epitaxial thin films grown under different substrate temperatures.

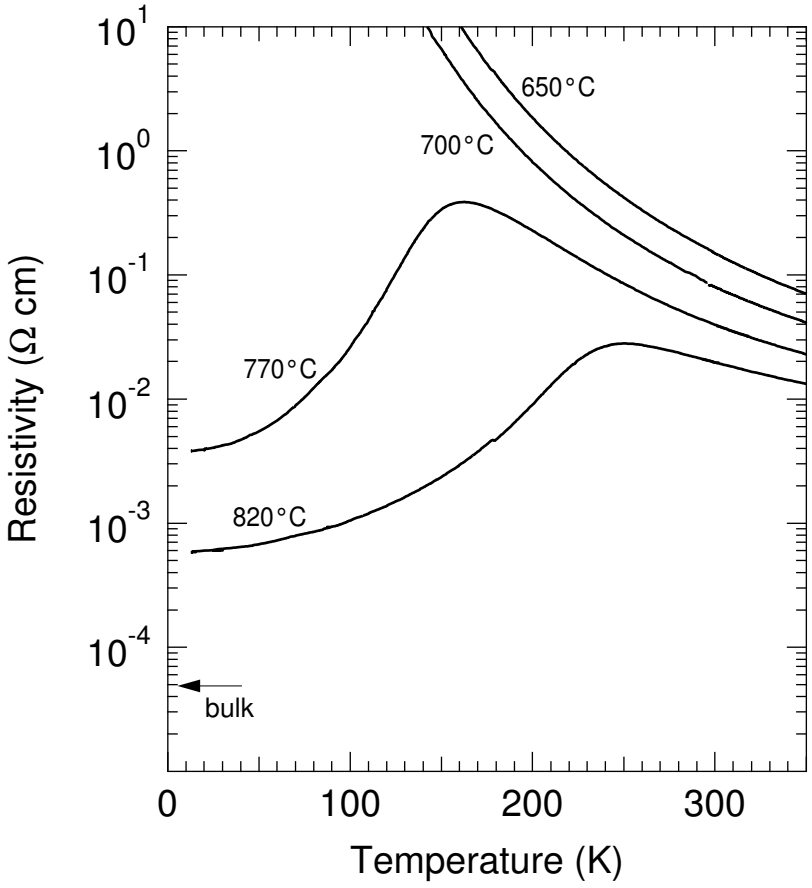

Figure 3.5: Temperature dependence of electrical resistivity for as-grown LSMO113 epitaxial thin films grown under different substrate temperatures.

deficiency in the as-grown films [1].

3.3.2 Effect of annealing in O_2

In manganates, the oxygen ion constitutes the medium over which electron hopping between neighboring sites takes place [1]. Therefore, the oxygen content in the films plays a decisive role in their electronic properties. To remove oxygen deficiency, films were annealed at 900 °C for 2 hours in flowing oxygen (1 ℓ/min). Figures 3.6 and 3.7 show magnetization and electrical resistivity characteristics for such annealed films. A large decrease in resistivity with a much higher Curie temperature is clearly observed. The films grown at 13 or 80 mTorr at 820 °C showed similar characteristics. T_C of both films was around 330 K, which is still below the bulk value of $\approx$ 370 K. The resistivity of these films, however, are of the same order as the single crystal value. Moreover, the magnetization at low temperatures is close to 3.7 μ_B/Mn, which is the value expected for full alignment of magnetic moments of Mn ions.

Increasing O_2 partial pressure ratio during sputtering to 50 % and in situ cooling in 700 Torr of oxygen immediately after growth were also tried. However, the results obtained were not superior to those described above.

3.3.3 Magnetoresistance

When magnetic fields were applied, a decrease of electrical resistivity was obtained as seen in Fig. 3.8. Data is for an as-grown film with a low T_C of approximately 250 K. In LSMO113, magnetoresistance is significant only in temperatures close to T_C, and therefore, could not be fully measured for annealed films because they have T_C's above 300 K, which was the maximum temperature reached in the measuring instrument. The MR characteristic of the figure indicates that the magnetoresistance value for the as-grown film, $-[\rho(B)-\rho(0)]/\rho(0)$, reached the maximum value of 78 % at 230 K.

With decreasing temperature, the magnetoresistance value also decreased as shown in Fig. 3.8. This behavior is typical for LSMO113 epitaxial films and single crystals. It is also understood from the mechanism of colossal magnetoresistance in these materials mentioned in Section 1.3 [1, 2].

3.4 Discussion

These results described above can be understood in terms of the double exchange model of Zener known to constitute the main physics of ferromagnetism and electron transport in the manganates [8]. According to this model, the ferromagnetic interaction occurs via the exchange of conduction electrons. The amplitude of the effective electron hopping between

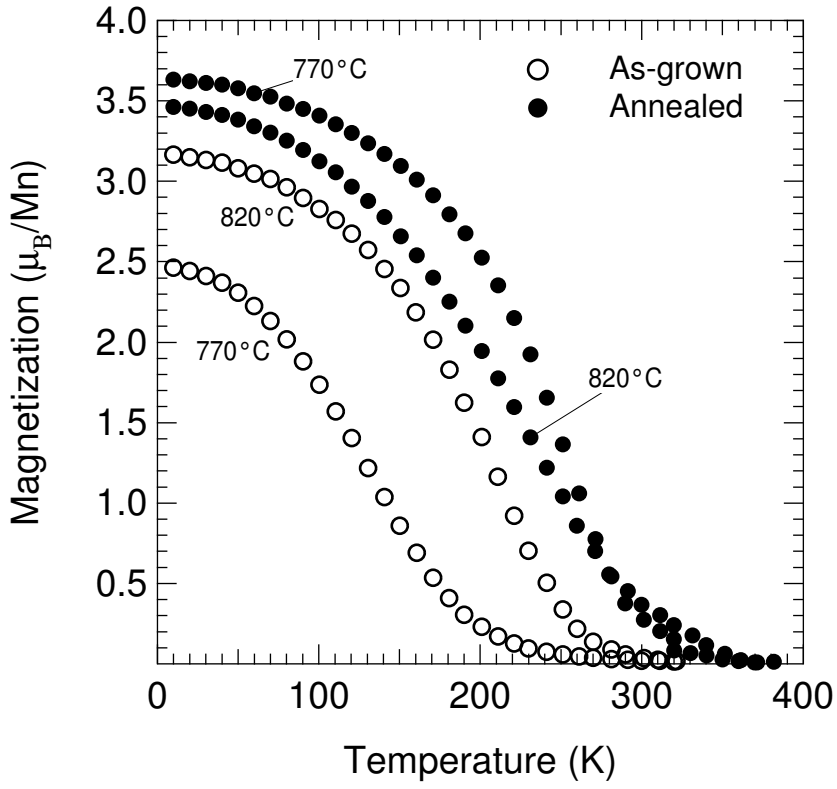

Figure 3.6: Temperature dependence of magnetization for annealed LSMO113 epitaxial thin films.

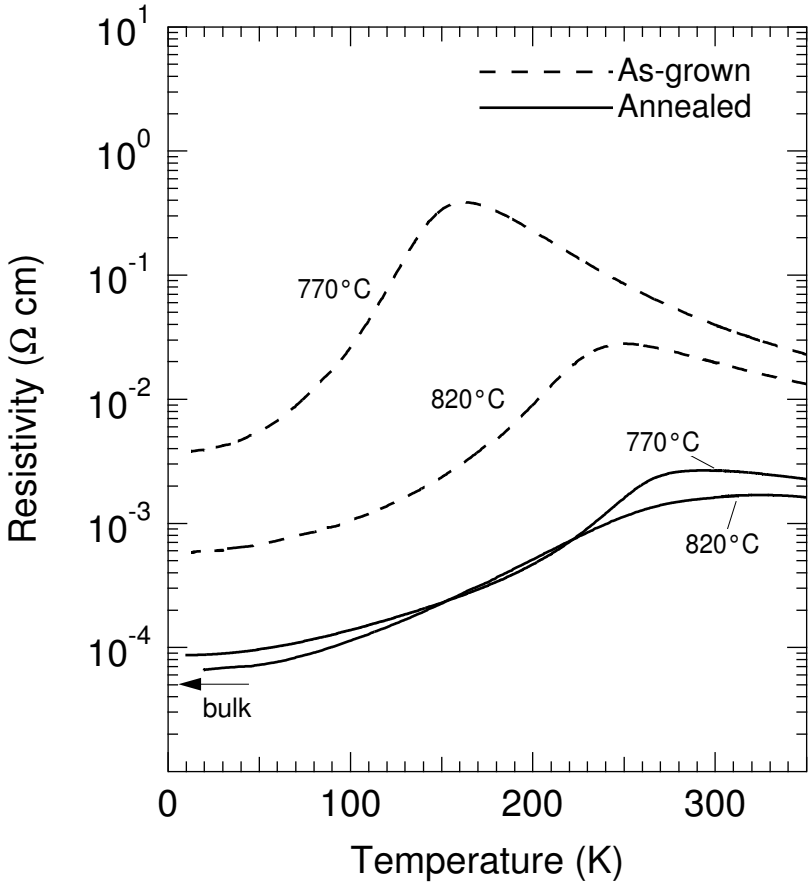

Figure 3.7: Temperature dependence of electrical resistivity for annealed LSMO113 epitaxial thin films.

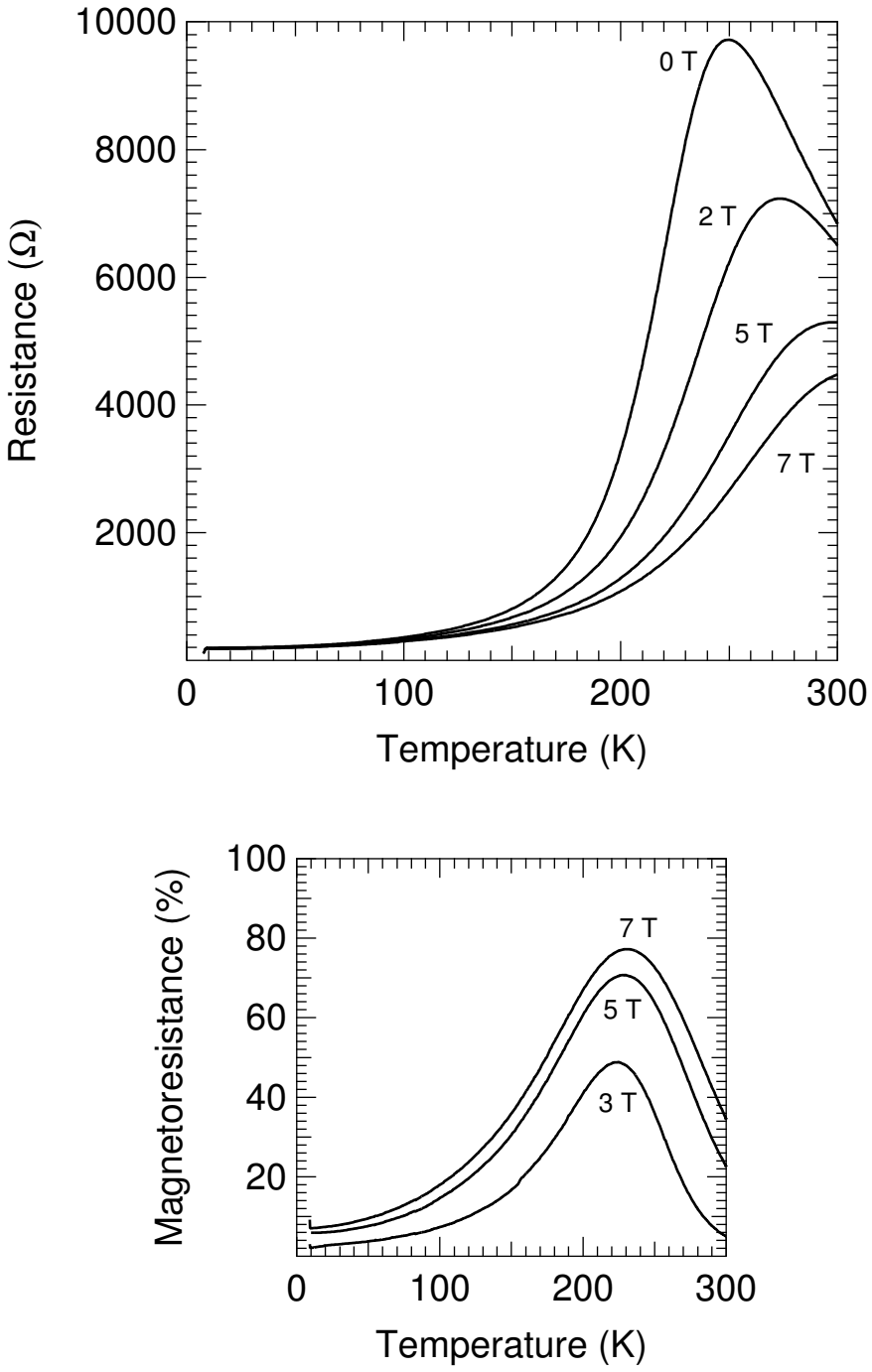

Figure 3.8: Typical magnetoresistance seen in LSMO113 epitaxial thin films.

Mn^{3+} and Mn^{4+} sites (i and j) is expressed as:

$$t_{ij} = t_{ij}^0 \cos(\theta_{ij}/2)$$

where t_{ij}^0 is the maximum hopping amplitude, and θ_{ij} the relative angle between the neighboring spins. t_{ij} depends also on both the distance between Mn and O ions and the Mn^{3+}-O-Mn^{4+} angle. The fact that higher $T_{\rm sub}$'s improve the magnetic property and lower the electrical resistivity indicates that the double exchange interaction is improved with increasing crystal quality of the film. The effect of annealing in O_2 is also accounted for using the same model as described above.

Even after annealing, $T_{\rm C}$ was short of ~ 40 K from the bulk value. This is probably due to a tensile strain exerted by STO substrate, which is manifested by the observed decrease in the out-of-plane lattice constant of these films (0.385 nm), compared with the bulk value 0.388 nm. This is consistent with reported results on strain effects in studies of manganate epitaxial thin films [2, 9].

3.5 A Spin Injection Device: Fabrication and Characterization

3.5.1 Introduction

Non-equilibrium effects in high-$T_{\rm c}$ superconductors have been a subject of interest recently because they are in intimate relation with the mechanism of superconductivity, which is not fully understood yet. They also offer a possibility of technological applications which have not been accessible so far [10, 11]. A major method for studying these non-equilibrium effects consists of injecting a spin-polarized current into a superconductor through a tunnel barrier, as mentioned in Section 1.3.4.

In such experiments, the interface between the different layers should be sharp enough to produce the intrinsic effects. Therefore, epitaxial films with a flat surface morphology are needed. For high-$T_{\rm c}$ superconductors, the ferromagnetic manganates are the most suitable because they have the same perovskite structure and fairly close lattice constants, as shown in Fig. 3.9. Moreover, they are preferable to conventional metals in that they show 100 % spin polarization [1].

In this study, epitaxial thin films for $La_{0.7}Sr_{0.3}MnO_3$ (LSMO113) and $La_{1.85}Sr_{0.15}CuO_4$ (LSCO) have been grown, and spin injection using these materials has been studied.

3.5.2 Device fabrication

$La_{0.7}Sr_{0.3}MnO_3$ (LSMO113) and $La_{1.85}Sr_{0.15}CuO_4$ (LSCO) epitaxial thin films have been grown by off-axis multi-target sputtering on $SrTiO_3$ (STO) (100) substrates. The fractional

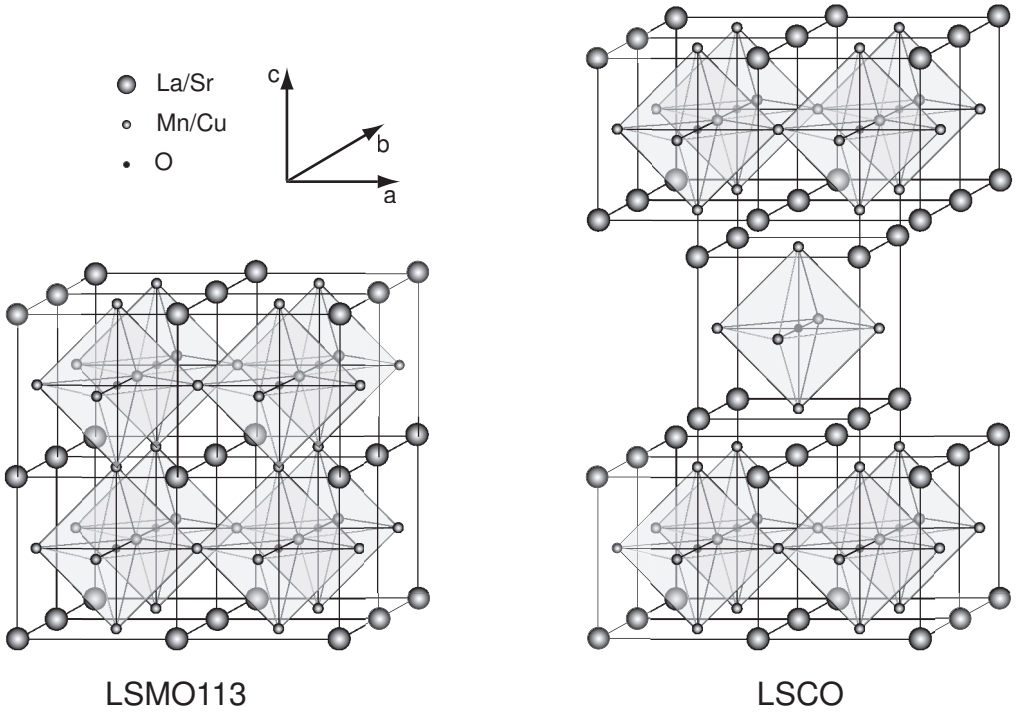

Figure 3.9: Crystal structure of the manganate LSMO113 and that of the high-T_c superconductor $La_{1-x}Sr_xCuO_4$ (LSCO).

ratio of O_2 in the mixed sputtering gas was fixed at 25 %. During the growth of LSMO113 films, the substrate temperature and the deposition rate were 860 °C and 1.1 nm/min, respectively. For LSCO both on STO and LSMO113, these parameters were adjusted to 830 °C and 0.55 nm/min, respectively. The targets used had chemical compositions of $La_{0.7}Sr_{0.3}MnO_3$ and $La_{1.85}Sr_{0.15}Cu_{1.05}O_4$. They were prepared by calcining a mixture of appropriate powders at 900–1200 °C for 12 h in air, and then sintering at 1000–1500 °C for 20 h in flowing O_2.

LSCO/LSMO113 structures were fabricated by photolithography and ion-milling. The configuration used in the spin-injection experiments is shown in Fig. 3.10. The area of the structure was 30×30 μm^2, and the film thickness was 156 and 250 nm for LSCO and LSMO113, respectively. The spin current flows from the top Au electrode into LSMO113 through LSCO.

3.5.3 Device characterization

As seen in Figs. 3.11 and 3.12, *c*-axis epitaxial films of LSCO and LSMO113 were obtained. The films had a composition of $La_{1.85}Sr_{0.15}CuO_{4+\delta}$ and $La_{0.7}Sr_{0.3}MnO_{3+\delta}$, respectively. The LSCO and LSMO113 films, which had a thickness of 125 and 250 nm respectively, show a smooth surface morphology as seen in the SEM images of Figs. 3.11 and 3.12. The surface of the films had a roughness of approximately 4.3 and 1.5 nm for LSCO and LSMO113, respectively, as determined by atomic force microscopy (AFM).

For the LSCO films, typical values for the onset of the superconducting transition temperature T_c were around 35 K as indicated in Fig. 3.11. For the present LSMO113 films grown, resistivities and transition temperatures close to the bulk value ($\approx$ 370 K) have been obtained, as seen in Fig. 3.12. When LSCO films were grown on LSMO113, an increased surface roughness was observed as seen in Fig. 3.13 (A roughness of 5.7 nm was observed by AFM). These films showed also a lower superconductivity T_c, as seen in the same figure.

Figure 3.13 shows resistivity data obtained for the LSCO/LSMO structure. When the current was increased from 1 to 10 μA, the superconducting transition temperature decreased as seen in Fig. 3.14. This decrease in T_c is considered to be due to the non-equilibrium effect induced by spin-current injection. From the large roughness value, it is inferred that the LSCO films contain many grain boundaries, where spin scattering occurs. In this case, spin polarization is reduced when the current is injected into LSCO, leading to the suppression of the non-equilibrium effect to a certain degree. As seen in Fig. 3.14, a negative resistance has been recorded. The reason for this is not sufficiently clear at present, but it may possibly be due to superficial effects coming from the structure measured. More analysis and optimization of the spin-injection structure, therefore, are needed first.

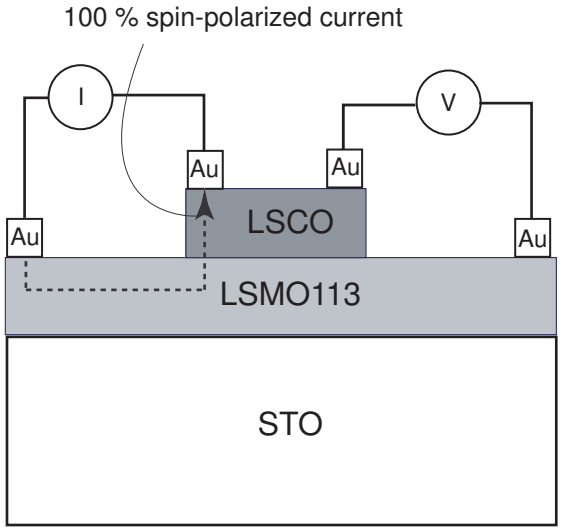

Figure 3.10: Structure of the spin-injection device fabricated in this study.

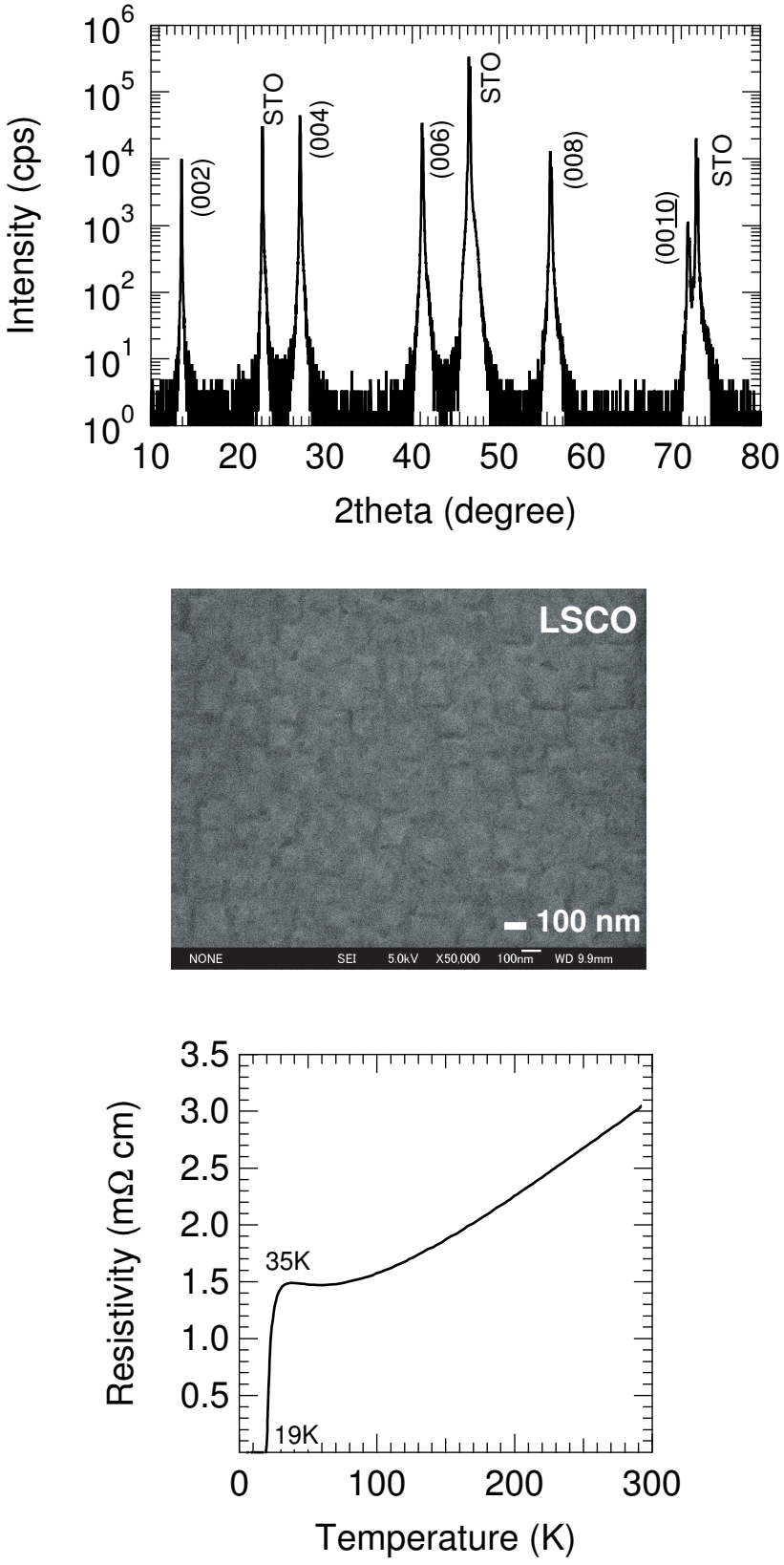

Figure 3.11: XRD pattern, HRSEM image, and temperature dependence of electrical resistivity for an LSCO film grown on STO.

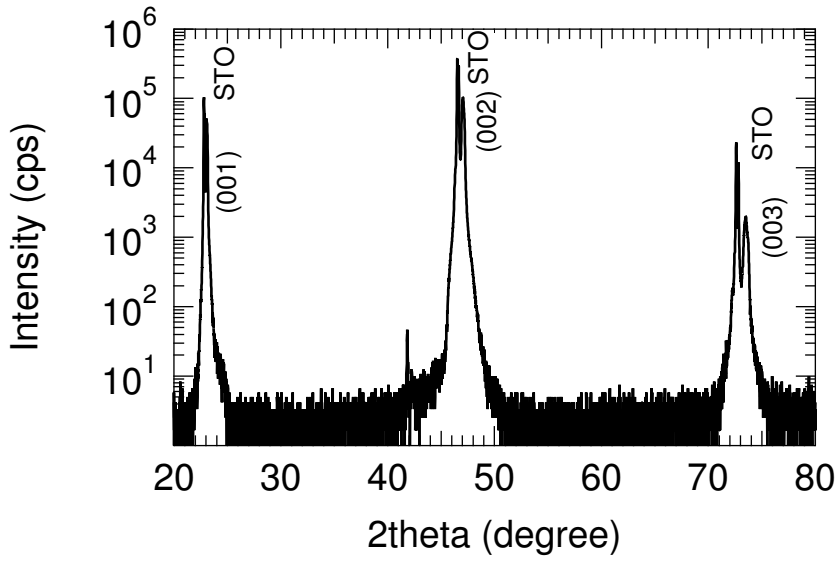

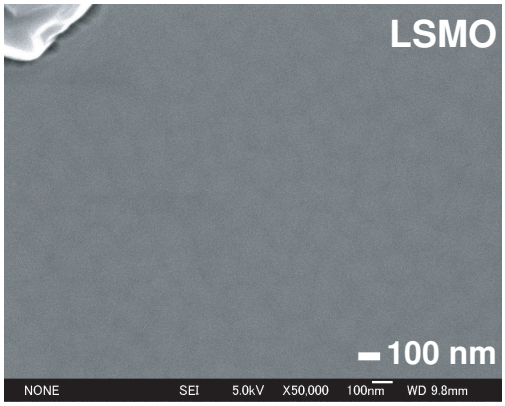

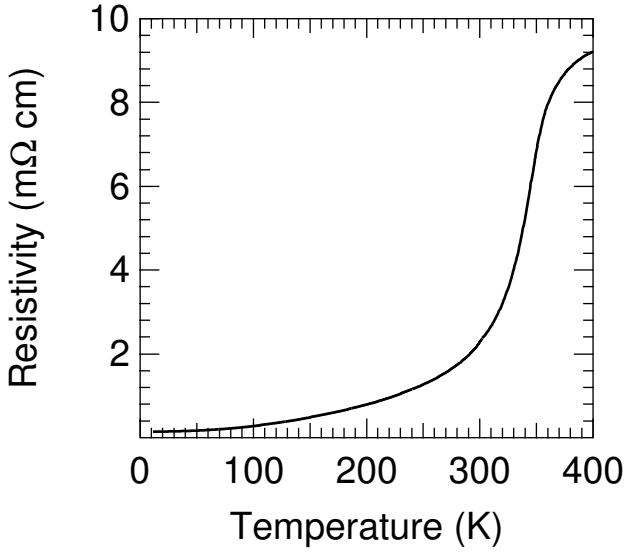

Figure 3.12: XRD pattern, HRSEM image, and temperature dependence of electrical resistivity for an LSMO film grown on STO.

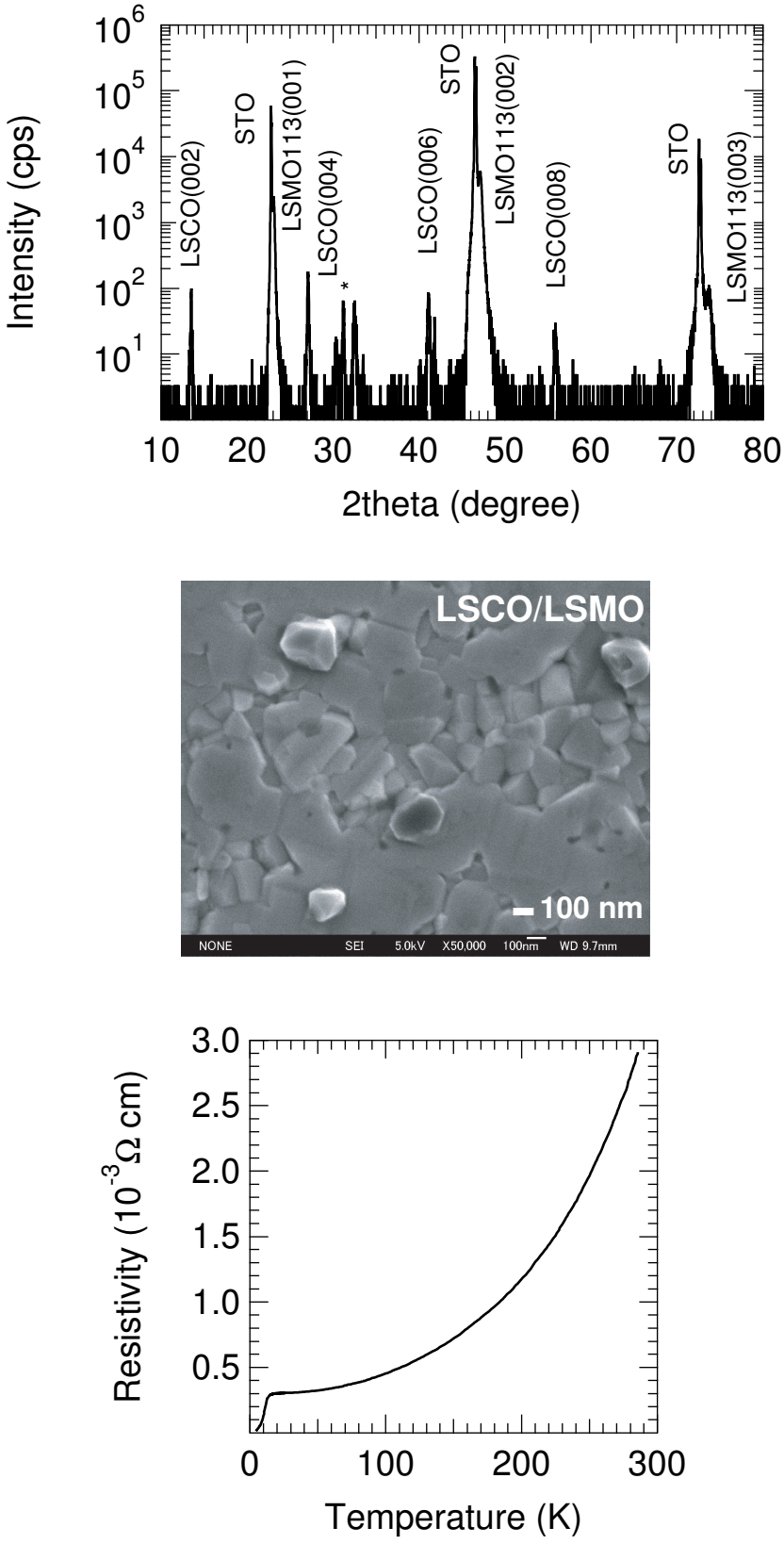

Figure 3.13: XRD pattern, HRSEM image, and temperature dependence of electrical resistivity for an LSCO/LSMO film grown on STO. The peak indicated as "∗" in the XRD pattern is unknown.

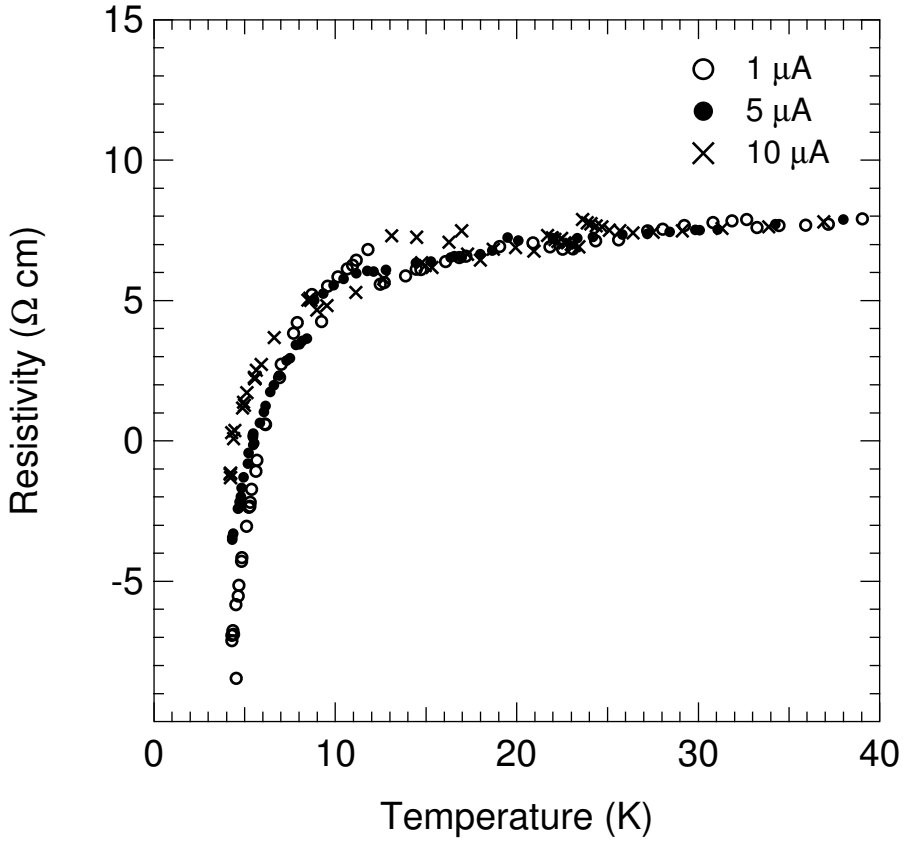

Figure 3.14: Dependence of LSCO film's electrical resistivity on the spin-current injected from LSMO113.

3.6 Summary

Epitaxial thin films of LSMO113 manganates have been grown by sputtering on $SrTiO_3$ (100) substrates at temperatures in the range $650 - 820\,^{\circ}C$. The films have been characterized using energy dispersive spectroscopy (EDS), reflection high energy electron diffraction (RHEED), x-ray diffraction (XRD), resistivity, and magnetization measurements. Films grown at $820\,^{\circ}C$ exhibited a streaky RHEED pattern indicating a smooth surface morphology. It has been found that the electrical and magnetic properties of LSMO113 epitaxial thin films are improved as the growth temperature is increased. When post-annealed in an oxygen atmosphere, films grown at $820\,^{\circ}C$ exhibited electrical resistivities at low temperatures comparable to those of the bulk, and have magnetization values reflecting the full spin alignment of Mn ions and conduction electrons.

Epitaxial thin films of LSMO113 have been also used as electrodes in a spin-injection experiment for the $(La,Sr)_2CuO_4$ high-T_c superconductor. A decrease in the superconducting transition temperature T_c has been obtained when the injected spin-current is increased, which suggests the occurrence of the non-equilibrium effect.

References

[1] Y. Tokura (Ed.), *Colossal Magnetoresistive Oxides* (Gordon and Breach, 2000).

[2] W. Prellier, P. Lecoeur, and B. Mercey, Cond-mat/0111363.

[3] K. Wasa and S. Hayakawa, *Thin Film Technology* (Kyoritsu Publishing, Tokyo, 2002).

[4] A. Urushibara, Y. Morimoto, T. Arima, A. Asamitsu, G. Kido, and Y. Tokura, Phys. Rev. B **51**, 14103 (1995).

[5] M. Kitagawa, K. K. Choi, K. Nakano, and Y. Yamazaki, J. Magn. Soc. Japan **22**, 1090 (1998).

[6] N. Sengoku and K. Ogawa, Jpn. J. Appl. Phys. **35**, 5432 (1996).

[7] C. Blue and P. Boolchand, Appl. Phys. Lett. **58**, 2036 (1991).

[8] C. Zener, Phys. Rev. **82**, 403 (1951).

[9] F. Tsui, M. C. Smoak, T. K. Nath, and C. B. Eom, Appl. Phys. Lett. **76**, 2421 (2000).

[10] V. A. Vas'ko, V. A. Larkin, P. A. Kraus, K. R. Nikolaev, D. E. Grupp, C. A. Nordman, and A. M. Goldman, Phys. Rev. Lett. **78**, 1134 (1997).

[11] S. Takahashi, H. Imamura, and S. Maekawa, Phys. Rev. Lett. **82**, 3911 (1999).

Chapter 4

c-Axis Epitaxial Growth and Characterization of Bilayer Manganate Thin Films

4.1 Introduction

The MnO_2-bilayer perovskite manganate system $La_{2-2x}Sr_{1+2x}Mn_2O_7$ (LSMO327) has been studied intensively in the past ten years because it shows colossal magnetoresistance (CMR) and intrinsic spin tunneling magnetoresistance, which are very attractive in many applications [1–7]. In order to study this intrinsic spin tunneling and its applications, c-axis epitaxial films of bilayer manganates are required.

Studies on the bilayer manganate $La_{2-2x}Sr_{1+2x}Mn_2O_7$ have been mostly performed on bulk samples. Only a few studies were conducted on c-axis epitaxial films. Furthermore, the c-axis films were grown only by pulsed laser deposition (PLD). By sputtering, on the other hand, only a-axis films were grown [8–11].

In Section 4.2, c-axis epitaxial thin film growth for the bilayer manganate LSMO327 by on-axis rf-magnetron sputtering is studied. In order to achieve c-axis epitaxial growth, the importance of controlling the deposition rate is explained. The magnetic, electrical, and magnetoresistive properties of the grown c-axis epitaxial thin films are characterized in Section 4.3. Intergrowths such as LSMO113 and LSMO214 are found to be incorporated easily into the structure of the layered manganates, and therefore, a quantitative method of characterizing these intergrowths based on X-ray diffraction (XRD) experiment and simulation is developed (Section 4.4). Finally, the obtained results on the c-axis epitaxial growth for the layered manganates and on the properties of the grown thin films are discussed in Section 4.5.

4.2 c-Axis Epitaxial Growth of $La_{2-2x}Sr_{1+2x}Mn_2O_7$ Thin Films

4.2.1 Conditions of thin film growth

LSMO327 layered manganate thin films were grown by on-axis rf-magnetron single target sputtering on sapphire ($1\bar{1}02$) and $SrTiO_3$ (STO) (100) substrates. The fractional ratio of O_2 in the mixed sputtering gas was fixed at 30 or 50 %. The sputtering pressure P_s was maintained during the film growth at a fixed value from 60 to 120 mTorr. The substrate was heated to temperatures up to 900 °C. The target used had a stoichiometric composition of $La_{1.4}Sr_{1.6}Mn_2O_7$. The substrate–target distance was 4.5 cm. Films were annealed at 900–1000 °C for 12–24 h in flowing oxygen.

In general, the deposition rate depends on sputtering conditions, i.e., the anode voltage V_a, the sputtering pressure P_s, the sputtering gas mixed ratio r_{O_2}, and the substrate temperature T_{sub}. Depending on these parameters, the deposition rate could be changed from 0.8 to 25 nm/min. The former value was attained when $V_a = 0.8$ kV, $P_s = 120$ mTorr, and $r_{O_2} = 50$ %, while the latter was attained at $V_a = 1.8$ kV, $P_s = 80$ mTorr, and $r_{O_2} = 30$ %. Eventually, the deposition rate was found to be very important to control the crystallographic orientation of LSMO327 epitaxial films, as described below.

4.2.2 Dependence of film composition on sputtering conditions

Figure 4.1 shows the dependences of the compositions [Mn]/([La]+[Sr]) and [Sr]/([La]+[Sr]) on substrate temperature T_{sub}, sputtering pressure P_s, and anode voltage V_a. It is generally seen that [Sr]/([La]+[Sr]) is almost constant, while the behavior of [Mn]/([La]+[Sr]) is complicated. The atomic ratio [Mn]/([La]+[Sr]) depends strongly on T_{sub} and P_s, while it remains nearly constant against the change in V_a. At low pressures (below 10 mTorr), the films have about 25 % of Mn in excess, while their Sr content is close to the target value. As P_s increases above 10 mTorr, [Mn]/([La]+[Sr]) decreases, and [Sr]/([La]+[Sr]) becomes slightly larger than that of the target by about 8 %. The decrease in the Mn content with increasing P_s is expected since the lighter Mn atoms are scattered more strongly than La and Sr atoms. The anode voltage dependence of film composition was found to be weak both for [Mn]/([La]+[Sr]) and [Sr]/([La]+[Sr]), as seen in Fig. 4.1.

From the above results, it follows that the Mn content tends to increase in excess at high temperatures where the epitaxial growth takes place. It was also found that Mn-rich composition causes the nucleation of the LSMO113 phase quite easily, so that it is essential that the film is stoichiometric or a little Mn-deficient. Therefore, P_s was increased in order to suppress the increase in the Mn content and to attain stoichiometry.

However, the range of available conditions for the stoichiometric film growth is significantly reduced when P_s is high. In this study, film compositions close to stoichiometry

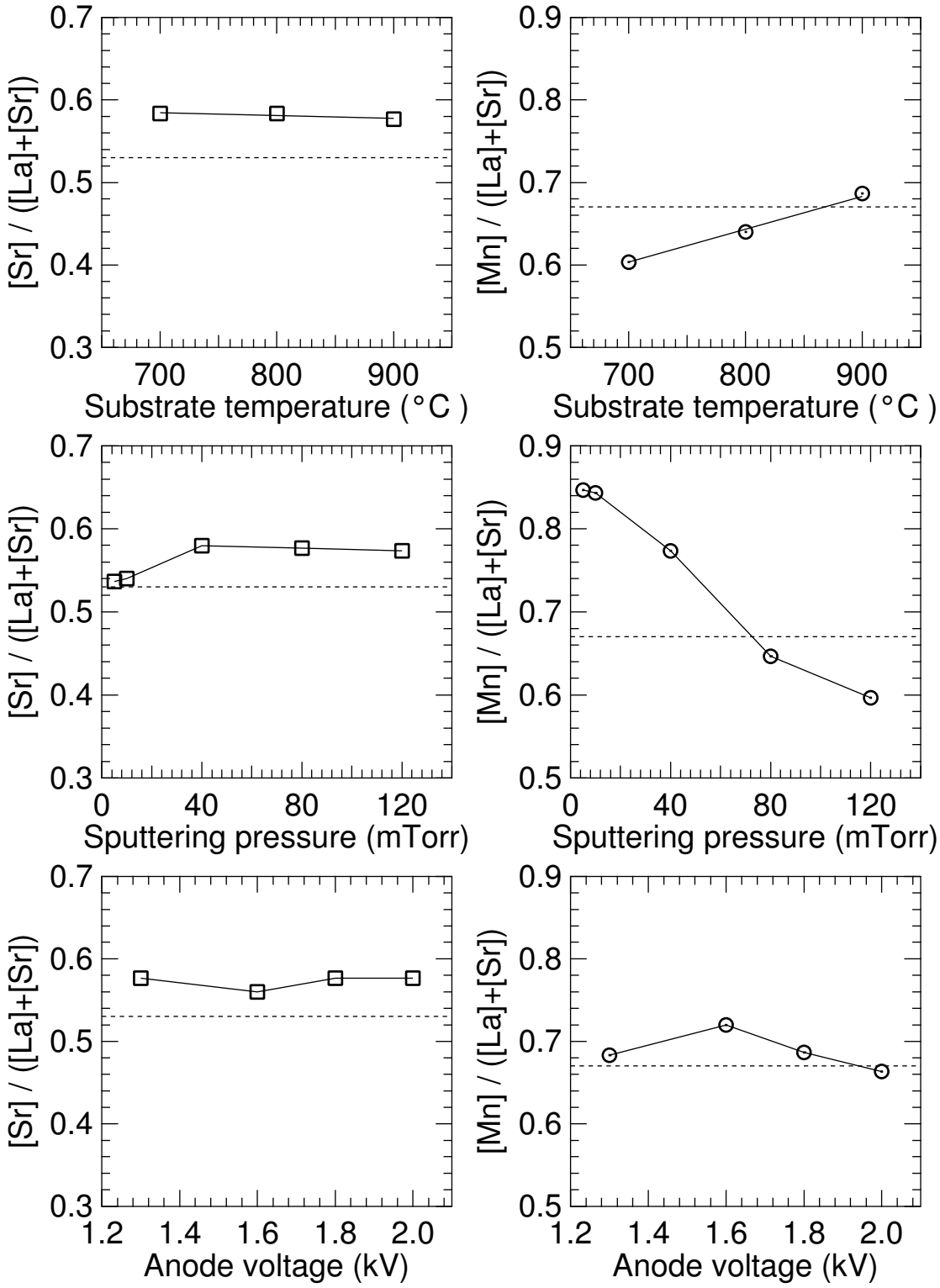

Figure 4.1: Dependence of film composition on substrate temperature, sputtering pressure, and anode voltage. The dotted line indicates the target composition $La_{1.4}Sr_{1.6}Mn_2O_7$.

were attained when $T_{\rm sub}$ was close to but below 920 °C and the growth rate was high, i.e., typically 25 nm/min at $V_{\rm a}$ = 1.8 kV. However, at the lowest rate 0.8 nm/min, attained under the conditions of $V_{\rm a}$ = 0.8 kV, $r_{\rm O_2}$ = 50 %, and $P_{\rm s}$ = 120 mTorr, the increase in the Mn content with increasing $T_{\rm sub}$ was significant and the films became Mn-rich. In this case, stoichiometry was attained only for $T_{\rm sub} \leq 760$ °C. A typical film thus obtained had a composition of $La_{1.25}Sr_{1.75}Mn_2O_{7+\delta}$.

4.2.3 Thin film growth at high deposition rates —25 nm/min—

Fig. 4.2 shows XRD patterns for stoichiometric films grown at the high deposition rate of 25 nm/min on STO substrates at $T_{\rm sub}$ in the range 760 − 920 °C. It is seen that at the lower substrate temperatures, the thin films grew in the *a*-axis growth mode. The *c*-axis growth appears only in the highest temperature $T_{\rm sub}$ = 920 °C, but the broad and low-intensity XRD peaks indicates that it is still very poor. Films grown on the sapphire substrate were polycrystalline, as shown in Fig. 4.3 for a film grown at $T_{\rm sub}$ = 760 °C.

Figure 4.4 shows HRSEM images for the above film. The films grown on STO substrates show smooth surfaces, while those grown on sapphire have a rough and grained surface.

4.2.4 Thin film growth at low deposition rates —0.8 nm/min—

When the deposition rate was lowered to 0.8 nm/min by adjusting the sputtering parameters to $V_{\rm a}$ = 0.8 kV, $P_{\rm s}$ = 120 mTorr, and $r_{\rm O_2}$ = 50 %, the film growth on STO depended on $T_{\rm sub}$ as shown in Fig. 4.5. For films grown of sapphire, a typical XRD pattern is shown in Fig. 4.6, obtained from a thin film grown at $T_{\rm sub}$ = 760 °C. As shown in Fig. 4.7, a continuous change from the *a*-axis to the *c*-axis growth was observed when $T_{\rm sub}$ was lowered from 760 to 630 °C. At $T_{\rm sub}$ = 760 °C, *c*-axis epitaxial thin films with clear XRD peaks were obtained. On the sapphire substrate, the films were polycrystalline and had probably some preferred orientation along the *c*-axis, although its signal was barely detected by XRD.

Films grown on STO, thus, exhibited distinctly different two patterns depending on the deposition rate. X-ray diffraction analysis indicated the *a*-axis growth for films grown at 25 nm/min, while it indicated the *c*-axis growth when the rate was decreased to 0.8 nm/min. Therefore, the control of deposition rate is crucial for the *c*-axis epitaxial film growth of LSMO327. The *c*-axis growth was observed when the deposition rate is lower than 2 nm/min at $T_{\rm sub}$ = 760 °C; at a deposition of 2 nm/min, the *c*-axis growth was absent and the *a*-axis growth appeared. Furthermore, it was also found that the *c*-axis growth is obtained when $T_{\rm sub} \geq 670$ °C. When the film growth rate was high, say, at 25 nm/min, *c*-axis films were obtained only when $T_{\rm sub} \approx 920$ °C. However, their XRD *c*-axis patterns were very poor as shown earlier. From these results, it is concluded that the conditions for the *c*-axis film growth are represented by low growth rates of below $\sim$ 0.8 nm/min, and substrate temperatures of above $\sim$ 760 °C. In the following sections, we focus on the *c*-axis films

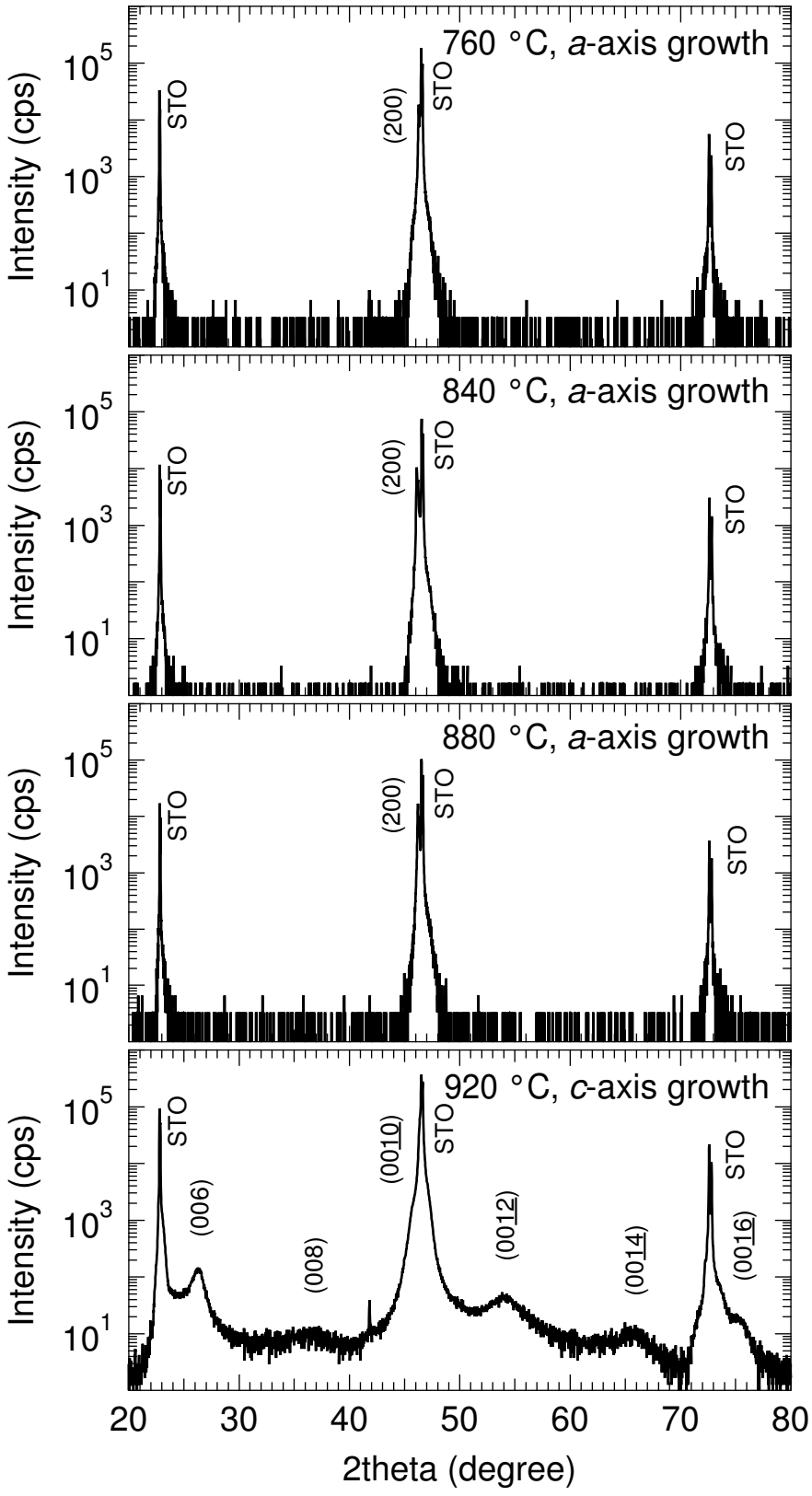

Figure 4.2: Dependence of film growth direction on substrate temperature for films grown on STO at high deposition rates of 25 nm/min .

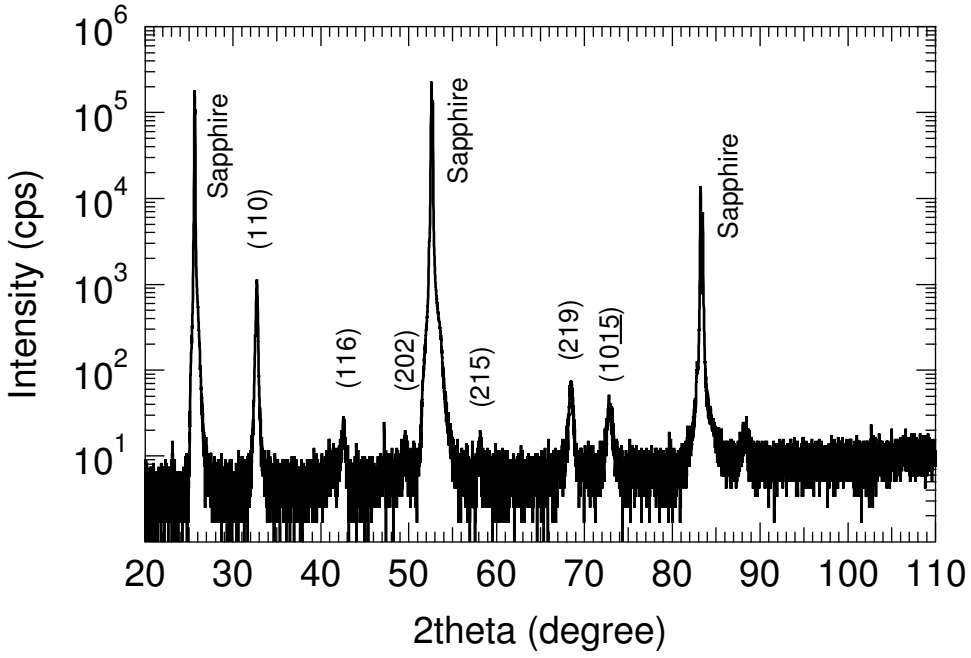

Figure 4.3: XRD pattern for a layered manganate thin film grown on sapphire $(1\bar{1}02)$ at 25 nm/min and $T_{\text{sub}} = 760\,^{\circ}\text{C}$.

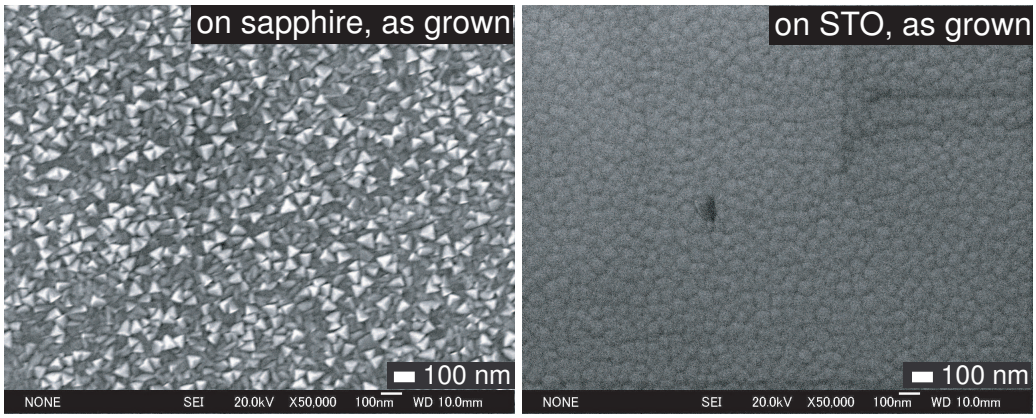

Figure 4.4: HRSEM surface images for films grown at 25 nm/min on sapphire $(1\bar{1}02)$ and STO (100) substrates.

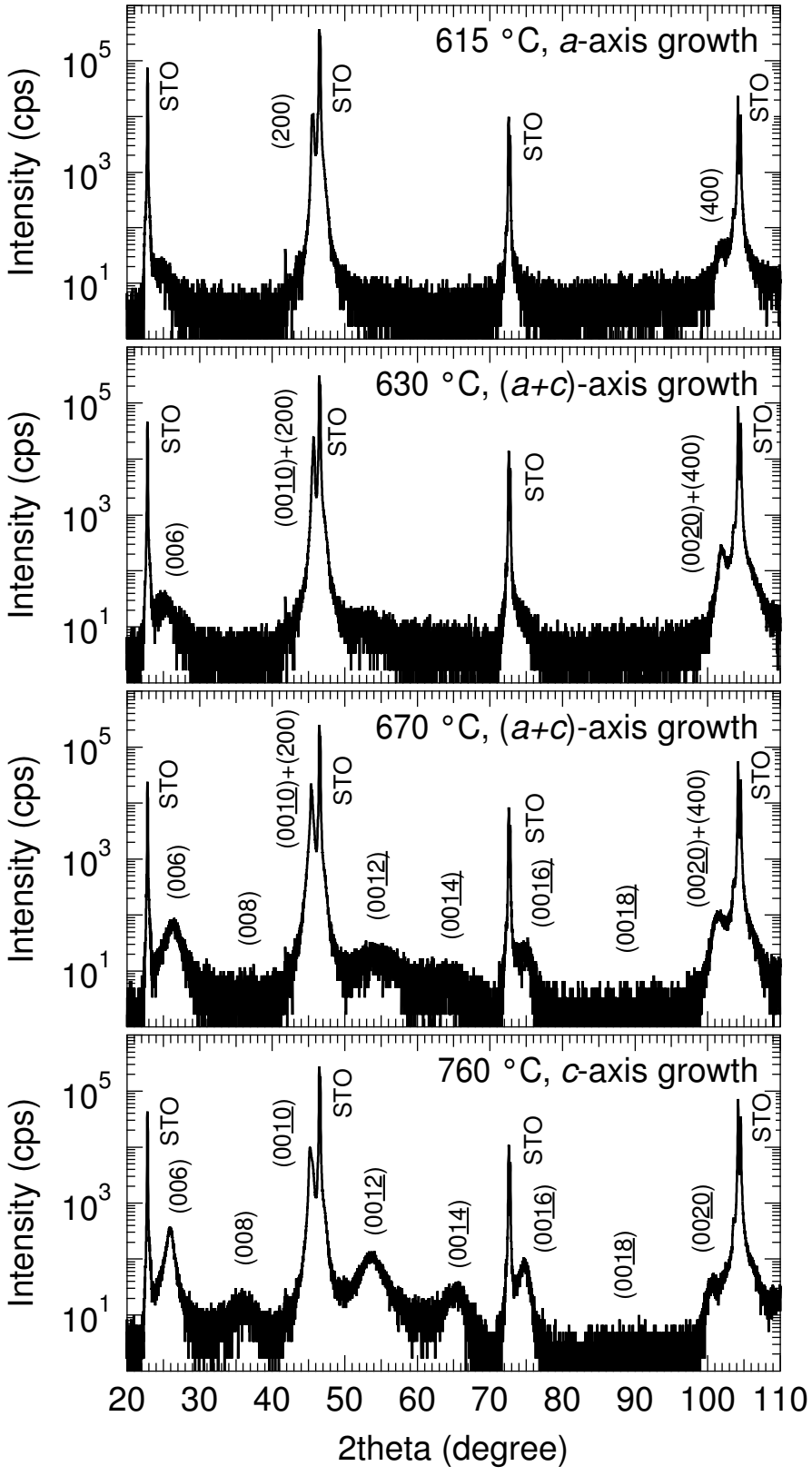

Figure 4.5: Dependence of film growth direction on substrate temperature for films grown on STO at low deposition rates of 0.8 nm/min.

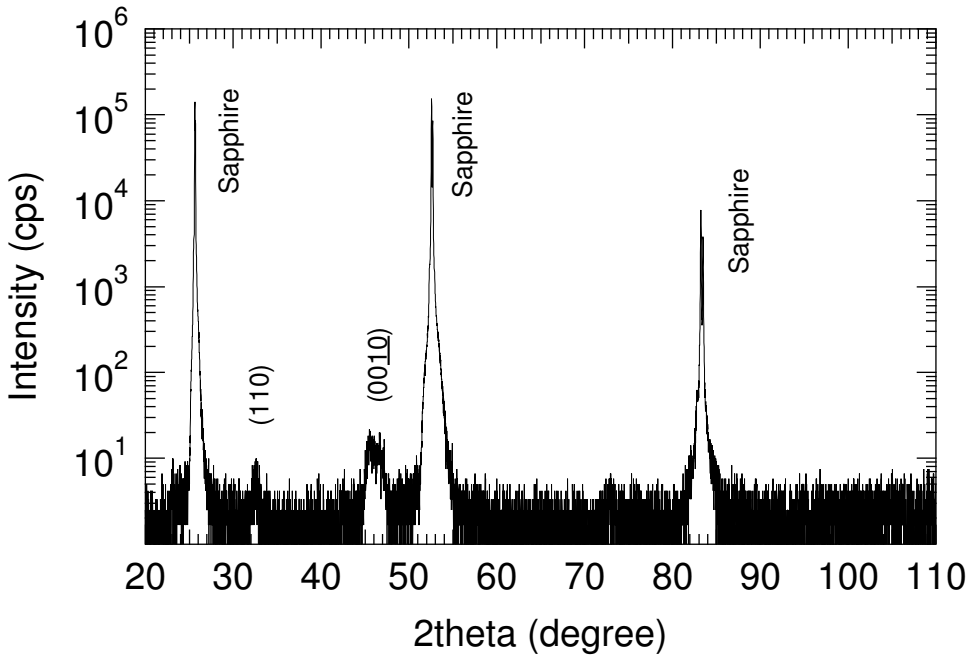

Figure 4.6: XRD pattern for a layered manganate thin film grown on sapphire (1$\bar{1}$02) at 0.8 nm/min and $T_{\text{sub}} = 760\,^{\circ}\text{C}$.

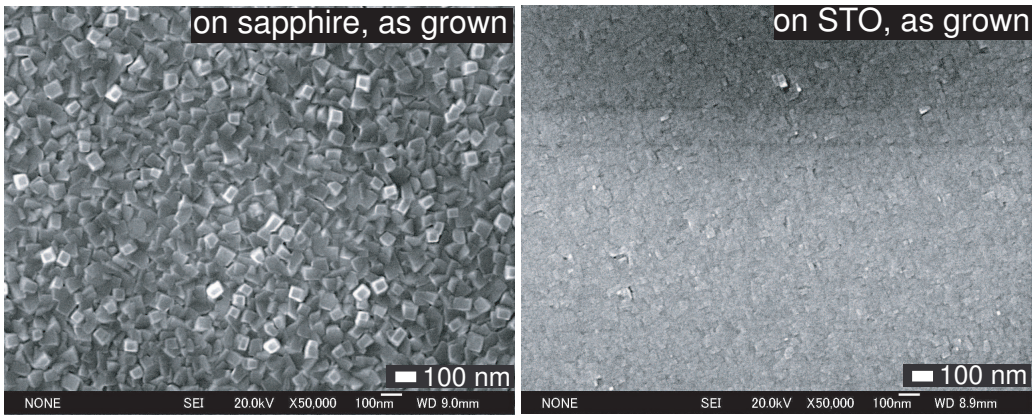

Figure 4.7: HRSEM surface images for films grown at 0.8 nm/min on sapphire (1$\bar{1}$02) and STO (100) substrates.

grown under these conditions unless otherwise noted.

Figure 4.7 shows HRSEM images for obtained as-grown films on sapphire and STO at 0.8 nm/min. For films grown on sapphire substrates, crystallites with clear crystal facets were observed on the surface. This surface morphology is different from that observed for films grown at 25 nm/min, and suggests some preferred crystalline orientation. Films grown on STO substrates show smooth surfaces. It is seen, however, that the film grown at 0.8 nm/min, compared with that grown at 25 nm/min is smoother and shows coalescence to a greater degree.

The c-axis lattice constant for the LSMO327 c-axis epitaxial films was evaluated to be 2.006 nm from the position of the main peak (00$\underline{10}$). This value is slightly smaller than the bulk value of 2.020 nm. The positions of the other (00ℓ) peaks are shifted largely ($\sim$ 0.04 nm when converted to the lattice constant) from each position expected from the above c-axis lattice constant. This shift occurs both in the negative and in the positive direction depending on each diffraction peak. Also, the films show large values for the full width at half maximum (FWHM), ranging from $\sim 0.5°$ for the diffraction peak (00$\underline{10}$) to $\sim 3.0°$ for (008). These characteristics are likely due to the intergrowth of other phases, e.g., LSMO113 or LSMO214 of the Ruddelsden-Popper series, as discussed later.

4.2.5 Effect of annealing in O_2

To compensate for a possible oxygen deficiency and to release residual strain, films were annealed at 900 °C for 24 h in flowing oxygen. By this annealing, the lattice constant decreased as shown in Fig. 4.8. For the c-axis epitaxial film, c decreased from 2.006 nm to 1.976 nm.

After annealing, the surface of all the films was degraded irrespective of the kind of substrate material, showing many precipitates as seen in Fig. 4.9. EDS results showed that these precipitates are Mn deficient, from which it is inferred that they are probably of the LSMO214 ($n = 1$) phase.

4.3 Magnetic, Electrical, and Magnetoresistive Characterization

4.3.1 Temperature dependence of magnetization

Figure 4.10 shows magnetization measurements for films as grown at 0.8 nm/min on STO (100) and sapphire (1$\bar{1}$02), together with the characteristics for annealed films. The values for magnetization per Mn atom were calculated from the observed magnetic moment of the samples, by assuming that the films are composed of the LSMO327 phase only. As can be seen, the magnetization for as-grown films shows a relatively weak temperature dependence. In contrast, the magnetization for annealed films shows an abrupt increase around 350 K

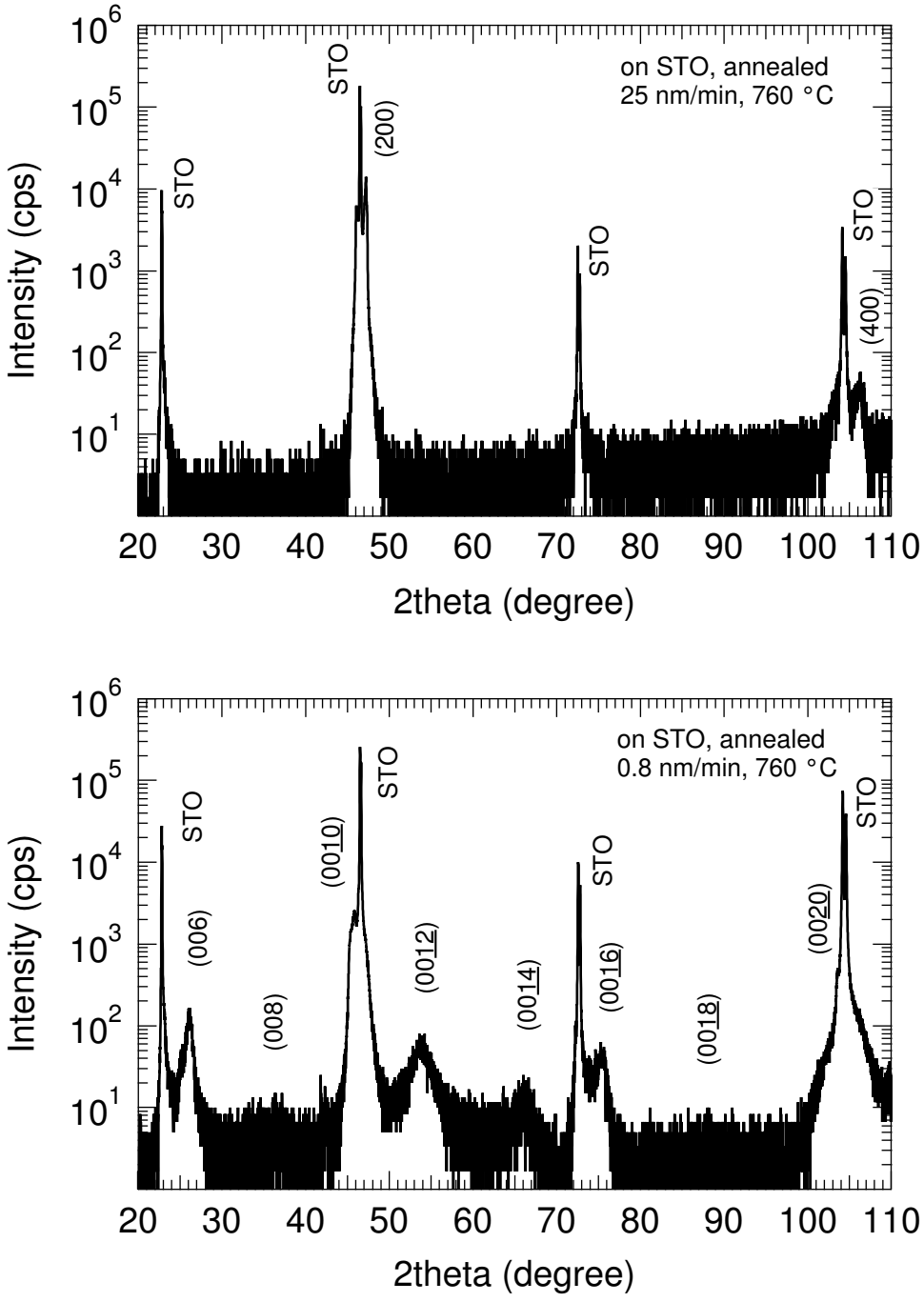

Figure 4.8: XRD patterns for annealed films grown at two different deposition rates, 25 and 0.8 nm/min, on STO (100) substrates. Annealing was conducted at 900 °C for 24 h in flowing oxygen.

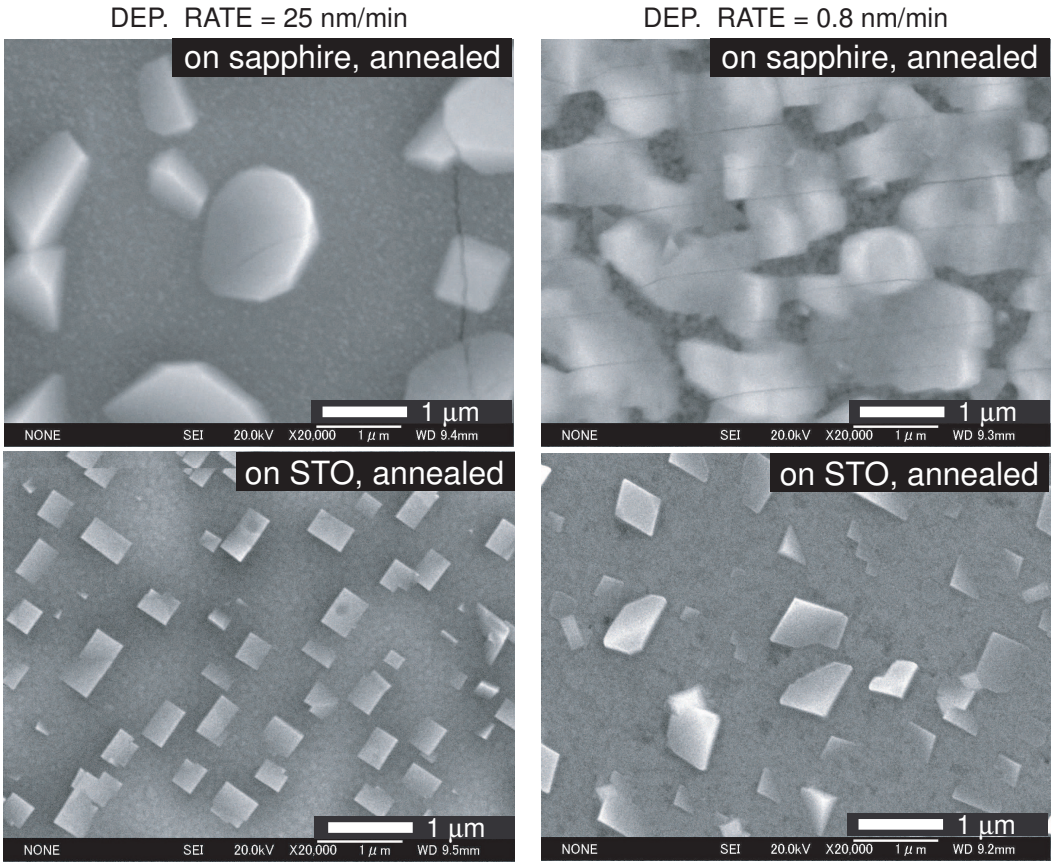

Figure 4.9: HRSEM surface images for annealed films grown at 25 and 0.8 nm/min on sapphire ($1\bar{1}02$) and STO (100) substrates.

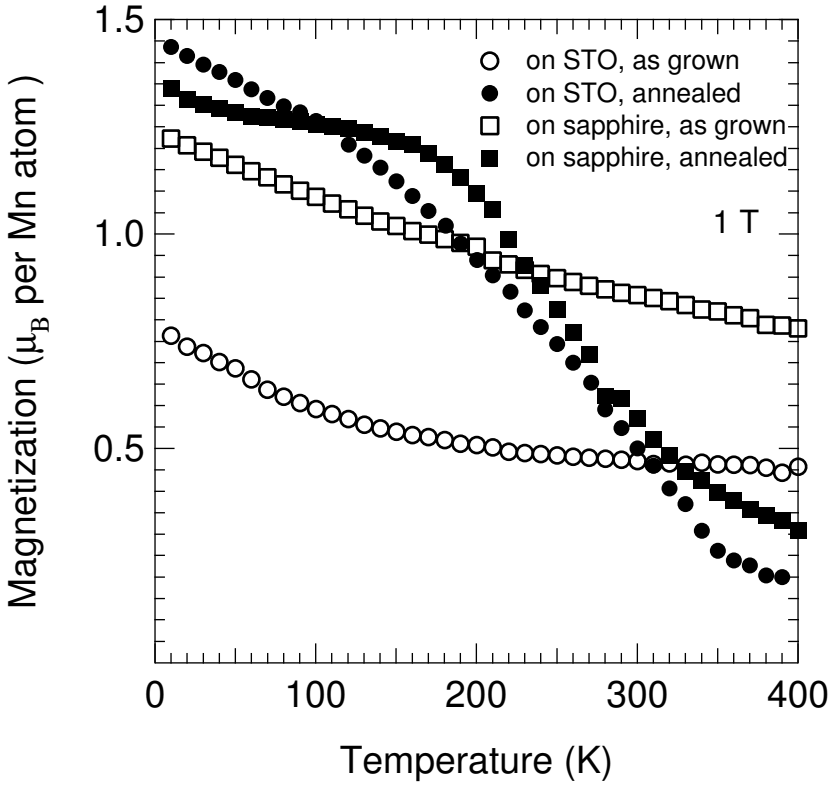

Figure 4.10: Temperature dependence of magnetization for annealed films grown at 0.8 nm/min on sapphire ($1\bar{1}02$) and STO (100), under an applied magnetic field of 1 T parallel to the film surface.

as T is decreased. Also, after annealing, the magnetization at low temperatures is higher than that of as-grown films, and is about 1.40 μ_B per Mn atom. This value is, however, much smaller than the theoretical value of 3.625 μ_B expected from full spin polarization.

Upon annealing in O_2, all the c-axis XRD peaks shifted to the high-angle direction, indicating a decrease in the c-axis lattice constant as shown in Fig. 4.8. This decrease is assumed to occur as oxygen vacancies in the crystal structure are filled substantially. This is because the anion O^{2-} present in the lattice functions to reduce the electrostatic repulsion between the cation species (here La^{3+}, Sr^{2+}, and Mn^{3+} or Mn^{4+}), which otherwise tends to stretch the structure. A decrease in the lattice constant with increasing O content was confirmed experimentally [12]. Considering that a relief of strain is also possible after annealing, the annealing effect on the magnetization of the films can be explained similarly as follows. According to Zener's double exchange model [13], the ferromagnetic interaction occurs via the exchange of conduction electrons between Mn ions through O ions. The amplitude of the effective electron hopping between Mn^{3+} and Mn^{4+} (i and j sites) is expressed as

$$t_{ij} = t_{ij}^0 \cos(\theta_{ij}/2),$$

where t_{ij}^0 is the maximum hopping amplitude, and θ_{ij} the relative angle between the neighboring spins. t_{ij} depends both on the distance between Mn and O ions and on the Mn^{3+}-O-Mn^{4+} angle. Therefore, the Curie temperature T_C is reduced in LSMO films which contain a large amount of O vacancies and strain. When as-grown films are oxygenated by annealing, T_C is expected to increase since t_{ij} increases.

It is also seen from Fig. 4.10 that the magnetization for as-grown films is quite large when contrasted with those for annealed films. For the reason for this result, it may be considered that the ferromagnetic interaction still remains in oxygen-poor as-grown films. In that case, a large magnetization might be induced in the presence of a magnetic field of $B = 1$ T even if T_C is diminished. However, it appears anomalous that the magnetization is still large even at 400 K, which is higher than $T_C = 370$ K for LSMO113, and the reason for this has yet to be known.

For the annealed films, the Curie temperature T_C was about 350 K and 330 K for films on STO and sapphire substrates, respectively. These values are much higher than that for the bulk (~ 115 K) [3], and they represent, supposedly, T_C values for the intergrowth phase.

4.3.2 Temperature dependence of electrical resistivity

Figure 4.11 shows electrical resistivity measurements for the annealed films on STO and sapphire substrates. For both films, the temperature dependence of resistivity has a peak that indicates a metal-insulator (MI) transition at 237 K and 142 K, respectively. These temperatures are lower than the corresponding T_C's determined from the magnetization, especially for the polycrystalline film on sapphire substrates. The resistivity of polycrystalline films grown on sapphire $(1\bar{1}02)$ had a resistivity more than one order of magnitude

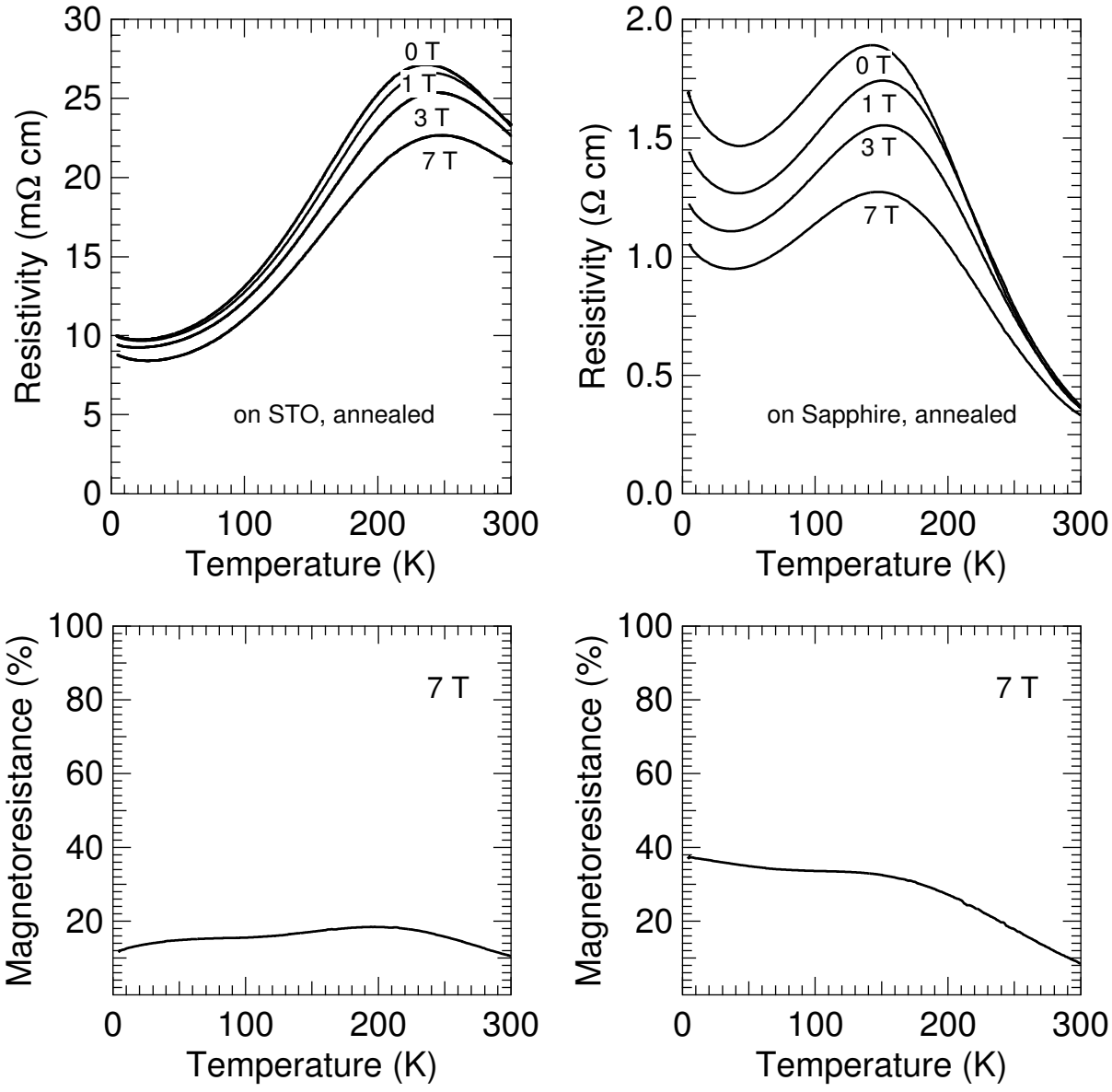

Figure 4.11: Temperature dependence of electrical resistivity for annealed films grown at 0.8 nm/min on sapphire ($1\bar{1}02$) and STO (100) in the presence of different magnetic fields.

larger than that for films on STO (100), presumably due to grain boundary scattering.

4.3.3 Magnetoresistance

When magnetic fields were applied, a decrease of resistivity was seen in the whole temperature range measured, as seen in Fig. 4.11. The MR characteristics of the same figure indicate that the magnetoresistance value, $-[\rho(B) - \rho(0)]/\rho(0)$, was 16 and 33 % for the films grown on STO and sapphire at 7 T at the MI transition temperature of 237 K and 142 K, respectively. These values are much smaller than a reported value of, say, 98 % at 7 T observed for *c*-axis films grown by pulsed laser deposition [8].

With decreasing temperature, the magnetoresistance values remained almost constant down to low temperatures. This behavior has been seen in layered manganate single crystals [3]. However, as discussed later, this behavior observed here and the observed low magnetoresistance values are probably related to intergrowth phases contained in the films.

4.4 Intergrowth Characterization by XRD Simulation

4.4.1 Introduction

The XRD patterns for the *c*-axis LSMO327 epitaxial films showed broad peaks that were shifted as discussed in 4.2 and as indicated in Fig. 4.12. Moreover, the surface of the films after annealing was degraded, showing many precipitates as was shown in Fig. 4.9. This is supposedly due to the presence of intergrowths such as LSMO113 and LSMO214. The crystal structure of these phases is similar to that of LSMO327 and they differ only in composition. Therefore, local composition deviations also can induce the growth of phases other than the bilayer manganate phase. In order to figure out this possibility, XRD patterns from intergrowth-included LSMO327 structures were numerically calculated using XRD simulations with an appropriate model to reproduce the observed characteristics. By comparing the calculation with the experimental results, the amount of intergrowth in the grown films was evaluated.

4.4.2 Simulation method

In this study, the one-dimensional kinematic X-ray diffraction model developed for superlattices by Fullerton *et al.* was used for XRD simulation [14]. The intergrowth phases considered were the cubic LSMO113 and the layered LSMO214 ($n = 1$). These and the crystal structure units used in the simulation are shown in Fig. 4.13. As can be seen, the LSMO113, LSMO214, and LSMO327 blocks consist of (La,Sr)O-MnO_2, (La,Sr)O-MnO_2-(La,Sr)O, and (La,Sr)O-MnO_2-(La,Sr)O-MnO_2-(La,Sr)O stacks, respectively.

Our *c*-axis films were modeled as a stack of 50 blocks consisting of LSMO327 and the intergrowth phases LSMO113 and LSMO214. In the simulation, they were stacked randomly,

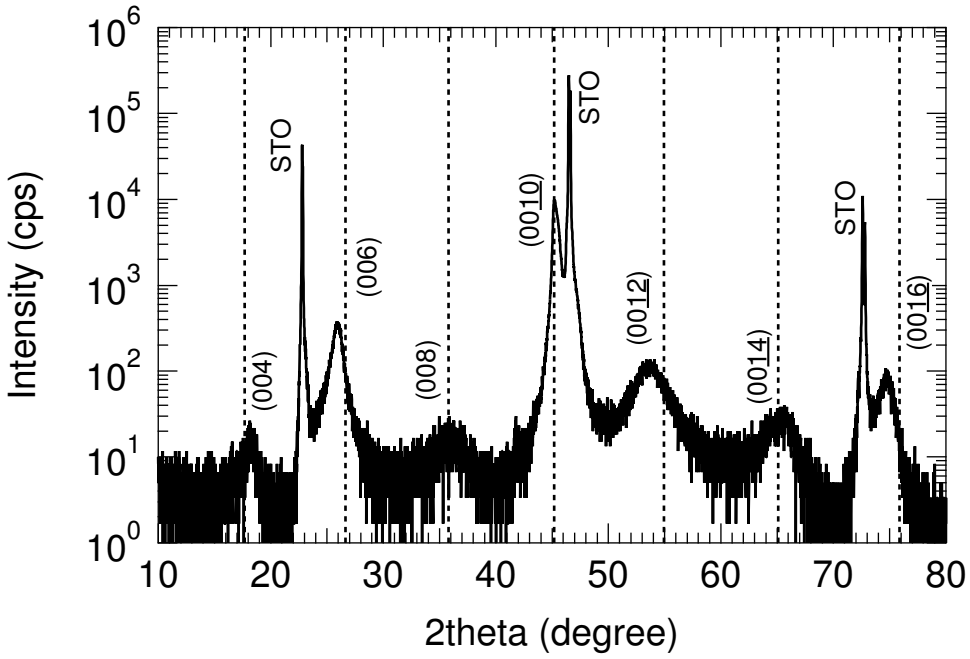

Figure 4.12: XRD pattern for a c-axis epitaxial layered manganate thin film, showing the shift of the XRD peaks from their positions calculated using the (00$\underline{10}$) peak (dotted lines).

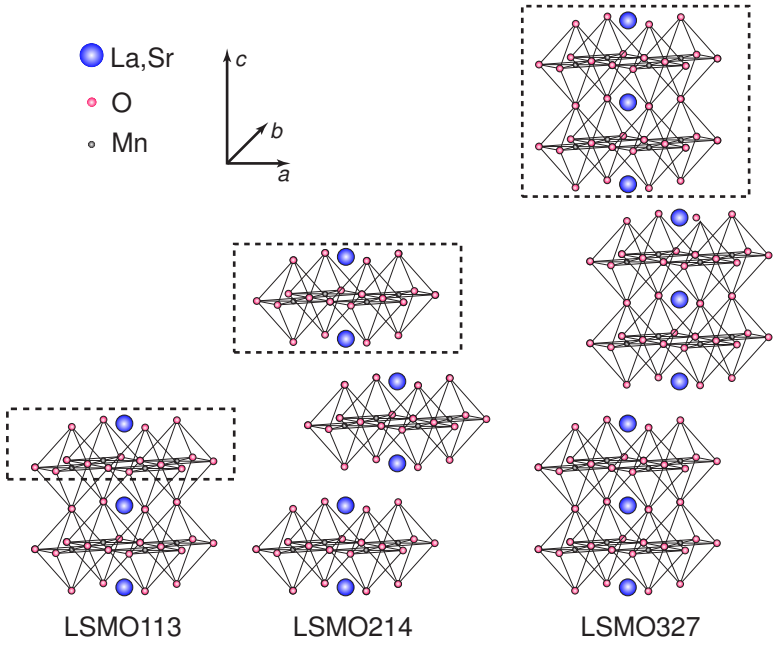

Figure 4.13: Crystal structure of LSMO113 ($n = \infty$), LSMO214 ($n = 1$), and LSMO327 ($n = 2$). For each phase, the crystal structure block used in the simulation is indicated by the dashed frame.

and the calculations were averaged over 100 random structures.

Let F_{113}, F_{214}, and F_{327} be the structure factors of the LSMO113, LSMO214, and LSMO327 blocks, respectively. Then the structure factor of the whole stack can be written as [15]:

$$F_{\text{total}} = \sum_{j=1}^{50} F_{\alpha(j)} \exp\left(4\pi i \frac{\sin(\theta)}{\lambda} D_j\right), \tag{4.1}$$

where $\alpha(j) =$ "113", "214", or "327" depending on the phase of the j-th block. D_j is the distance from the first to the j-th block, and is calculated as $D_j = D_{j-1} + c_{\alpha(j-1)} (D_1 = 0)$. c_{113} is the lattice constant of LSMO113. c_{214} and c_{327} are half the lattice constants of LSMO214 and LSMO327, respectively. θ is the incidence angle, and λ is the wavelength for Cu Kα_1 X-rays.

The structure factor for each block is:

$$F_{113} = (f_{(\text{La,Sr})} + f_{\text{O}}) + (f_{\text{Mn}} + 2f_{\text{O}}) \exp\left(4\pi i \frac{\sin(\theta)}{\lambda} s\right), \tag{4.2}$$

$$F_{214} = (f_{(\text{La,Sr})} + f_{\text{O}}) + (f_{\text{Mn}} + 2f_{\text{O}}) \exp\left(4\pi i \frac{\sin(\theta)}{\lambda} s\right) + (f_{(\text{La,Sr})} + f_{\text{O}}) \exp\left(4\pi i \frac{\sin(\theta)}{\lambda} 2s\right), \tag{4.3}$$

$$F_{327} = (f_{(\text{La,Sr})} + f_{\text{O}}) + (f_{\text{Mn}} + 2f_{\text{O}}) \exp\left(4\pi i \frac{\sin(\theta)}{\lambda} s\right) + (f_{(\text{La,Sr})} + f_{\text{O}}) \exp\left(4\pi i \frac{\sin(\theta)}{\lambda} 2s\right) + (f_{\text{Mn}} + 2f_{\text{O}}) \exp\left(4\pi i \frac{\sin(\theta)}{\lambda} 3s\right) + (f_{(\text{La,Sr})} + f_{\text{O}}) \exp\left(4\pi i \frac{\sin(\theta)}{\lambda} 4s\right), \tag{4.4}$$

where f_{Mn} and f_{O} are the atomic scattering factors for Mn and O, respectively. $f_{(\text{La,Sr})}$ is taken as the average atomic scattering factor corresponding to the La:Sr ratio in the chemical composition of the film. s is the distance between the (La,Sr)O plane and the neighboring MnO_2 plane. The anomalous scattering corrections are included. The actual numerical values can be found in [16].

The X-ray scattering intensity for the whole film is thus given by $F_{\text{total}} F^*_{\text{total}}$, where F^*_{total} is the complex conjugate of F_{total}. The average of this value over 100 random stacks was taken as the simulated X-ray scattering intensity for the corresponding film.

4.4.3 Simulation results

Figure 4.14 shows the dependence of the XRD pattern on the intergrowth phase and its amount. In the results shown , the atomic scattering factors were set equal among the different elements for the sake of simplicity. The real values were precisely taken into account in the quantitative results mentioned later. The simulation shows that, as the amount of intergrowth increases, the diffraction peak positions systematically shift. It is seen that, as the intergrowth of LSMO113 increases, the (004), (008), and (00$\underline{10}$) peaks shift to higher angles, while the (006) and (00$\underline{12}$) peaks shift to lower angles. In the case of

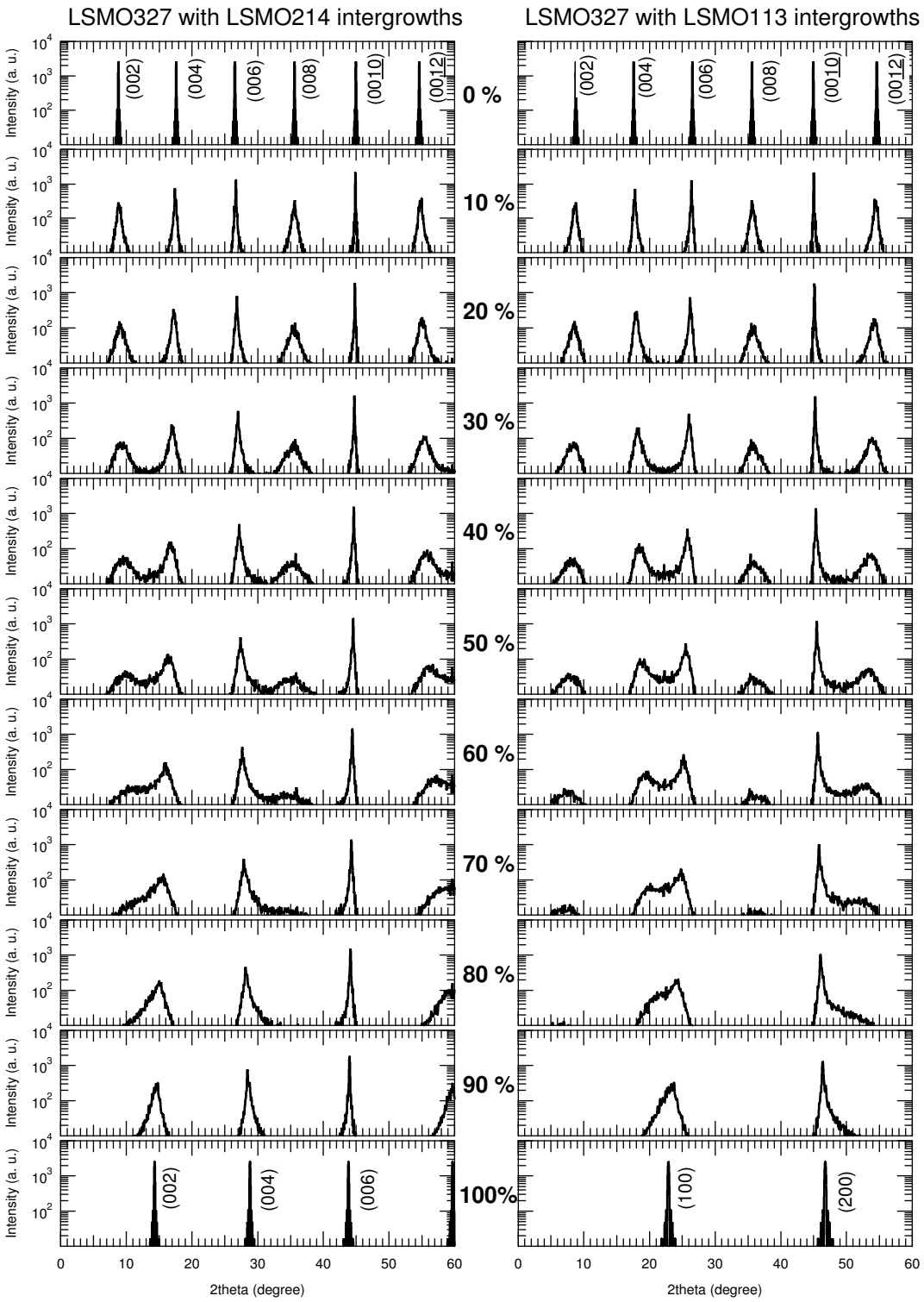

Figure 4.14: XRD simulation results for intergrowth-containing LSMO327 *c*-axis structures. In these results, the atomic scattering factors were set equal among the different elements for the sake of simplicity.

the LSMO214 intergrowth, (004), (006), and (008) peaks shift to higher angles, while the (00$\underline{1}$0) and (00$\underline{1}$2) peaks shift to lower angles. Therefore, the (006) and (00$\underline{1}$0) peaks shift in the different directions depending on the kind of intergrowth.

Figure 4.15 shows the equivalent lattice constant shift for several diffraction peaks, where the equivalent lattice constant shift for a given peak indicates the change in the lattice constant c from the value given by the (00$\underline{1}$0) peak when calculated from that peak's position via the Bragg equation. The atomic scattering factors are now set to their real values. It is seen that the direction and the magnitude of the shift depend strongly on each XRD peak and on the intergrowth crystal structure. This was used to characterize quantitatively intergrowths in the grown c-axis epitaxial thin films of layered manganates.

4.4.4 Quantitative evaluation of intergrowths in c-axis $La_{2-2x}Sr_{1+2x}Mn_2O_7$ epitaxial thin films

The dashed lines in Fig. 4.15 show the equivalent lattice constant shift for the peak considered observed in the as-grown c-axis epitaxial thin films. When the intergrowth consists wholly of LSMO214, the direction and the magnitude of the calculated shifts deviate significantly from the observed values, as seen in the left panel of the figure. In contrast, good coincidence is obtained when the intergrowth content is about 30 % of LSMO113, as seen in the right panel of the same figure. Furthermore, an addition of up to 10 % of LSMO214 phase yielded a better XRD pattern in view of relative peak intensities with the shift almost unchanged. We estimate, then, that the grown films contain about 40 % of intergrowth (30 % from the LSMO113 phase and 10 % from the LSMO214 phase). The simulated pattern for this amount of intergrowth is shown in Fig. 4.16. It is seen that the simulated result reproduces the experimental XRD pattern pretty well, including the large broadening of the XRD peaks, even in the above simplified XRD model. As for FWHM, the simulation result ranges from $\sim 0.25°$ for (00$\underline{1}$0) to $\sim 3.5°$ for (008), which are comparable with the experimental results.

We have also estimated the amount of LSMO113 intergrowth in the films after annealing using the above simulation. From the experimental XRD pattern for the annealed film shown in Fig. 4.8, it was found that the equivalent lattice constant shift for the peaks (006) and (00$\underline{1}$2) are 0.065 nm and 0.066 nm, respectively. In Fig. 4.15, this corresponds roughly to an LSMO113 intergrowth amount of 40 %. Therefore, it turns out that the LSMO113 intergrowth increases from 30 % to about 40 % by annealing. The free energy for the layered crystal structures of the manganates (Ruddelsden-Popper series) are probably quite similar, which leads to the formation of intergrowths during film growth or annealing, as in the present case.

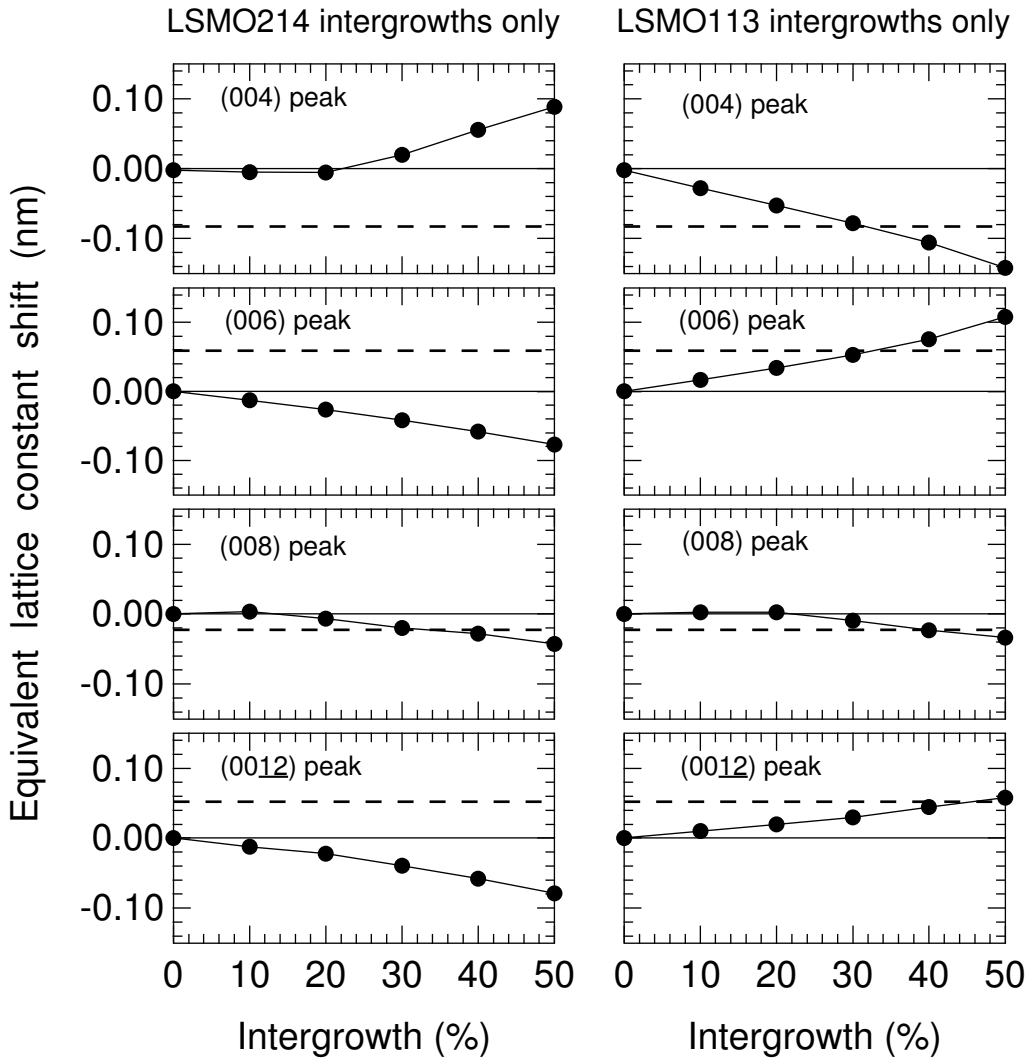

Figure 4.15: Dependence of the equivalent lattice constant shift from the value calculated from the (00$\underline{10}$) peak on intergrowth content. The dashed lines represent the experimental values obtained in the c-axis epitaxial layered manganate thin films.

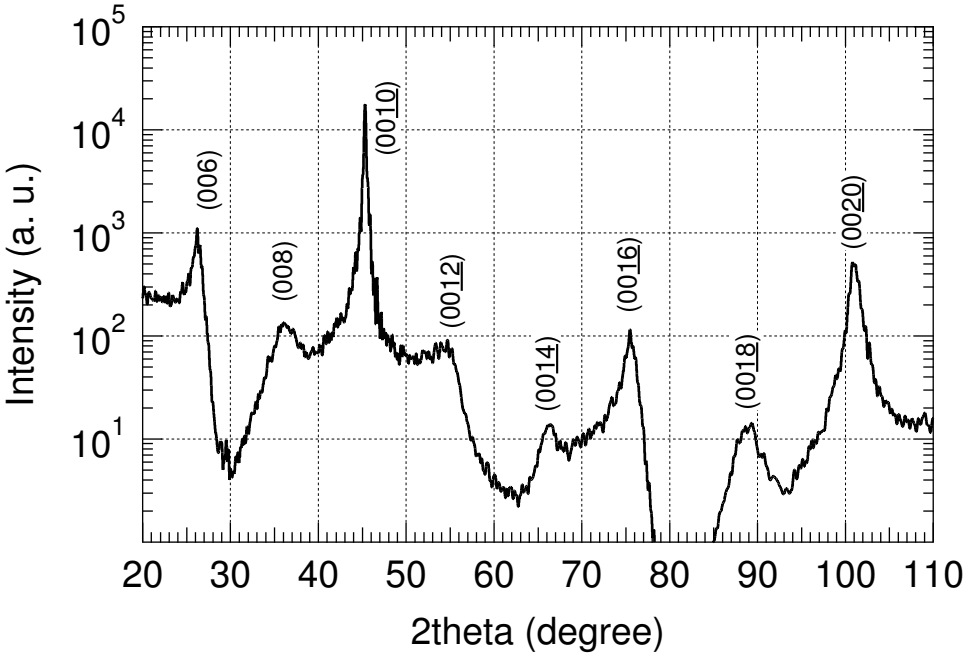

Figure 4.16: Simulated XRD pattern for a *c*-axis epitaxial layered manganate thin film with 40 % of intergrowths (30 % of LSMO113 and 10 % of LSMO214).

4.5 Discussion

4.5.1 Deposition rate and *c*-axis epitaxial growth

The bilayer manganate $La_{2-2x}Sr_{1+2x}Mn_2O_7$ has a layered structure and is strongly anisotropic. In such a structure, the crystal growth rate is generally slow in the *c*-axis direction. To grow *c*-axis films, therefore, a sufficiently low deposition rate is necessary when the growth rate in the *ab*-plane direction is limited as in the present case [17]. In the experiments, it is found that the maximum deposition rate is ~ 0.8 nm/min for the LSMO327 *c*-axis growth at 760 °C. The crucial role of the deposition rate has also been known in the crystal growth of layered materials. For example, large single crystals of the $Bi_2Sr_2Ca_2Cu_3O_{10}$ (Bi2223), a CuO_2 triple layered high-T_c superconductor, had not been grown until very low growth rates were accessible [18].

4.5.2 Magnetic and magnetotransport properties

Among the intergrowth phases considered, LSMO214 is an antiferromagnetic insulator ($T_N < 130$ K) or a spin glass depending on Sr content [3, 19, 20]. Therefore, its contribution to the magnetization can be neglected. LSMO113 is, in contrast, known to show metallicity and ferromagnetism with a high T_C of 370 K [19]. It is likely that this LSMO113 intergrowth phase raises T_C to 350 K, which is much higher than that for LSMO327, in consistence with the results of Section 4.3.

The existence of many intergrowth phases in the films suggests that the films are, most probably, composed of many ferromagnetic and non-ferromagnetic regions. This probably explains the magnetization value 2.2 μ_B shy of the full polarization observed in the experiments (Fig. 4.10). It also gives a qualitative explanation of the observed low magnetoresistance values and their temperature dependences, since the conductivity for LSMO113 is much larger than that for LSMO327 and dominant to give large magnetoresistance. The persistent magnetoresistance at low temperatures is probably due to spin-dependent tunneling between the ferromagnetic grains, indicating that even the epitaxial films on STO are polycrystalline in the present experiment.

4.6 Summary

c-Axis epitaxial thin films of a layered manganate $La_{2-2x}Sr_{1+2x}Mn_2O_7$ have been grown on $SrTiO_3$ (100) substrates by on-axis rf-magnetron sputtering. It was shown that the film chemical composition is sensitive to the deposition parameters, and that a small deviation of composition or deposition condition causes nucleation of the (La,Sr)MnO_3 structure. It is found that the deposition rate is crucial for the *c*-axis film growth; stoichiometric *c*-axis $La_{2-2x}Sr_{1+2x}Mn_2O_7$ films have been grown under limited conditions of a low rate of

0.8 nm/min, an (Ar, O_2 50 %) atmospheric pressure of 120 mTorr, and a substrate temperature of 760 °C. An XRD simulation method has been developed in order to characterize intergrowths in *c*-axis layered manganate epitaxial thin films. From the simulation results, it is inferred that the grown *c*-axis $La_{2-2x}Sr_{1+2x}Mn_2O_7$ films contain intergrowths comprised of (La,Sr)MnO_3 and presumably (La,Sr)$_2MnO_4$ structures, and the total intergrowth fraction amounts to about 40 %.

References

[1] T. Kimura, Y. Tomioka, H. Kuwahara, A. Asamitsu, M. Tamura, and Y. Tokura, Science **274**, 1698 (1996).

[2] Y. Moritomo, Y. Tomioka, A. Asamitsu, Y. Tokura, and Y. Matsui, Phys. Rev. B **51**, 3297 (1995).

[3] T. Kimura and Y. Tokura, Ann. Rev. Mater. Sci. **30**, 451 (2000).

[4] H. Asano, J. Hayakawa, and M. Matsui, Phys. Rev. B **56**, 5395 (1997).

[5] T. Kimura, A. Asamitsu, Y. Tomioka, and Y. Tokura, Phys. Rev. Lett. **79**, 3720 (1997).

[6] T. G. Perring, G. Aeppli, T. Kimura, Y. Tokura, and M. A. Adams, Phys. Rev. B **58**, R14693 (1998).

[7] S. Heim, T. Nachtrab, M. Mö, R. Kleiner, R. Koch, S. Rother, O. Waldmann, P. Müller, T. Kimura, and Y. Tokura, Physica C **367**, 348 (2002).

[8] Y. Konishi, T. Kimura, M. Izumi, M. Kawasaki, and Y. Tokura, Appl. Phys. Lett. **73**, 3004 (1998).

[9] J. B. Philipp, J. Klein, C. Recher, L. Alff, and R. Gross, Phys. Stat. Sol. A **189**, 367 (2002).

[10] K. Takahashi, N. Kida, and M. Tonouchi, Autumn Meeting of the Physical Society of Japan **430**, 6pXD-15 [in Japanese] (2002).

[11] H. Asano, J. Hayakawa, and M. Matsui, Appl. Phys. Lett. **70**, 2303 (1997).

[12] N. Sengoku and K. Ogawa, Jpn. J. Appl. Phys. **35**, 5432 (1996).

[13] C. Zener, Phys. Rev. **82**, 403 (1951).

[14] E. E. Fullerton, I. K. Schuller, H. Vanderstraeten, and Y. Bruynseraede, Phys. Rev. B **45**, 9292 (1992).

[15] N. W. Ashcroft and N. D. Mermin, *Solid state physics* (Saunders College, 1976).

[16] E. Prince (Ed.), *International Tables for Crystallography, Vol. C* (Kluwer Academic Publishers, Dordrecht/Boston/London, 2004).

[17] H. Asano, Dr. Thesis, Nagoya University, Nagoya, Japan, 1992 [in Japanese].

[18] T. Fujii, T. Watanabe, and A. Matsuda, J. Cryst. Growth **223**, 175 (2001).

[19] Y. Tokura (Ed.), *Colossal Magnetoresistive Oxides* (Gordon and Breach, 2000).

[20] S. Larochelle, A. Mehta, L. Lu, P. K. Mang, O. P. Vajk, N. Kaneko, J. W. Lynn, L. Zhou, and M. Greven, Phys. Rev. B **71**, 024435 (2005).

Chapter 5

Improved c-Axis Epitaxial Growth of Bilayer Manganate Thin Films by Cu-Substitution

5.1 Introduction

In order to study the intrinsic tunneling found in layered manganates and its potential applications, it is necessary to grow layered manganate c-axis epitaxial thin films. However, the c-axis epitaxial growth for these layered materials is not necessarily easy, as discussed in Chapter 4. Therefore, a technique that facilitates the c-axis growth is desired. Expecting such a technique, the effect of substituting Mn with Cu on the c-axis epitaxial growth for LSMO327 has been explored. The results are described in the present chapter. This technique is particularly of a practical value if Cu-doping does not affect the magnetic properties of the bilayer manganates as has been reported for some isotropic manganates (Fig. 5.1) [1].

Cu-substitution lowers the melting point of the manganates. Therefore, the atom's migration is fostered at the growing film surface. This is of crucial importance for c-axis epitaxial growth [2], as discussed in Section 4.5. It is, then, expected that the c-axis epitaxial growth is improved when Mn is partially replaced with Cu. Cu-substitution facilitates also the fabrication of sputtering targets for the manganates, as described in Section 2.1.2.

A quantitative comparison between c-axis epitaxial films of Cu-doped and non-doped bilayer manganates is carried out in Section 5.2. The enhancement of c-axis growth by Cu-doping found therein is discussed. The effect of Cu-doping on the magnetic and magnetoresistive properties for $La_{2-2x}Sr_{1+2x}Mn_{2-y}Cu_yO_7$ bilayer manganates is also described and discussed.

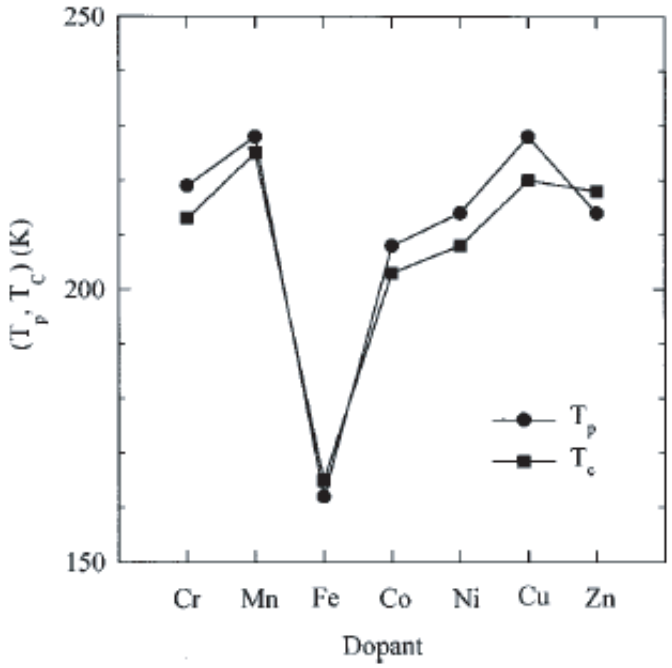

Figure 5.1: Dependence of the metal-insulator transition temperature T_{p} and the Curie temperature T_{C} on the doping element in the manganate $La_{0.7}Ca_{0.3}MnO_3$ by Ghosh *et al.* [1]

5.2 *c*-Axis Epitaxial Growth of Cu-Substituted $La_{2-2x}Sr_{1+2x}Mn_2O_7$ Thin Films

5.2.1 Conditions of thin film growth

Bilayer manganate thin films of $La_{2-2x}Sr_{1+2x}Mn_2O_7$ and Cu-doped $La_{2-2x}Sr_{1+2x}Mn_{1.8}Cu_{0.2}O_7$ were grown on STO(100) substrates as in Chapter 4. The sputtering atmosphere was a mixed gas of Ar (70 %) and O_2 (30 %). Sputtering was performed under a pressure of 110 mTorr at an anode voltage of 1.2 kV. The substrate was heated to temperatures up to 920 °C. The targets used had nominal compositions of $La_{1.4}Sr_{1.6}Mn_{2.2}O_7$ and $La_{1.4}Sr_{1.6}Mn_{1.8}Cu_{0.2}O_7$. They were prepared using the solid state reaction technique as described in Section 2.1.2. 10 % of Mn was added to the non-doped target for chemical stabilization. The Cu-doped stoichiometric target, in contrast, was about 6 % denser and robust against aging. The deposition rate was approximately 8 nm/min. The film thickness was approximately 250 nm. Energy dispersive x-ray spectroscopy (EDX) analysis revealed a typical film composition of $La_{1.3}Sr_{1.7}Mn_2O_{7+\delta}$ and $La_{1.3}Sr_{1.7}Mn_{1.8}Cu_{0.2}O_{7+\delta}$ for unsubstituted and substituted films, respectively.

5.2.2 Characterization of *c*-axis epitaxial growth

Figures 5.2 and 5.3 show XRD patterns for films of non-doped $La_{2-2x}Sr_{1+2x}Mn_2O_7$ and Cu-doped $La_{2-2x}Sr_{1+2x}Mn_{2-y}Cu_yO_7$ ($y = 0.2$), grown at 800 and 920 °C, respectively. At a substrate temperature of $T_{sub} = 800$ °C, films for both compositions grew with the *a*-axis perpendicular to the substrate (i.e., *a*-axis films). When T_{sub} was increased to 920 °C, the film growth orientation changed from the *a*-axis to the *c*-axis. In the XRD patterns for the *c*-axis epitaxial films, it is clearly observed that the Cu-substituted films have much stronger diffraction peaks than the unsubstituted films. Moreover, the full widths at half maximum (FWHM) of the XRD peaks are smaller for the Cu-substituted film, as shown in Table 5.1. This indicates improvements in the film epitaxial growth brought about by the Cu-substitution. The resistivity for this film is 0.5 Ω cm at room temperature. This value is 4 times smaller than that of the bulk, which also shows semiconductive temperature dependence, as will be described in Section 5.3.

For both *c*-axis films, the *c*-axis lattice constant could not be determined as a single value because it changed from one peak to the other, and this change was both in the plus and minus directions. This is due to the presence of intergrowth phases such as LSMO113 in the film crystal structure. The scattering in the lattice constant when calculated from each XRD peak was larger in the non-doped films, which indicates a decrease in intergrowth content as Cu is introduced into the film.

To quantify this improvement in film crystallinity by Cu-doping, the numerical XRD simulation method developed in Chapter 4 was used. Figure 5.4 shows the simulation result

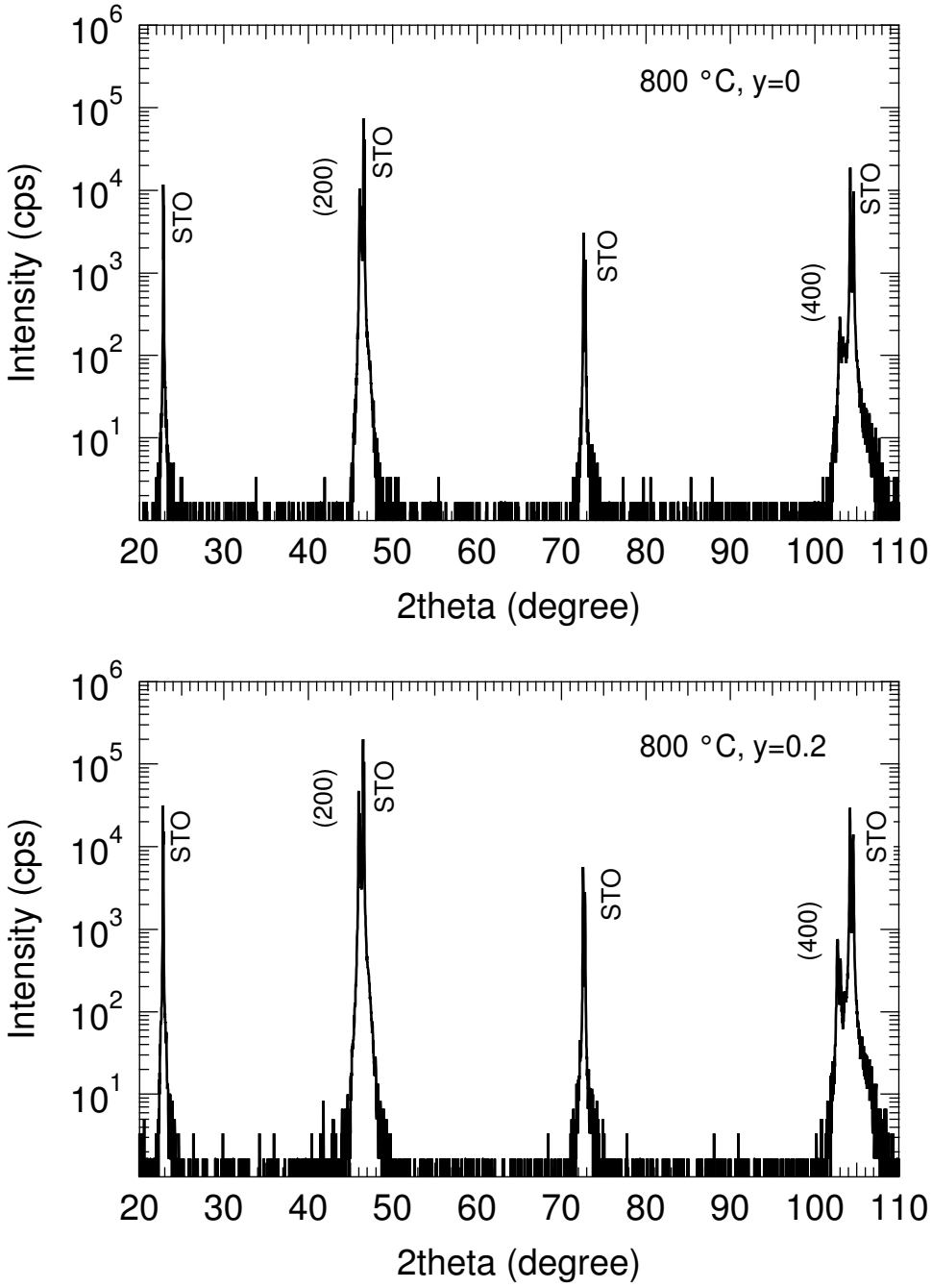

Figure 5.2: XRD patterns for non-doped $La_{2-2x}Sr_{1+2x}Mn_2O_7$ and Cu-doped $La_{2-2x}Sr_{1+2x}Mn_{2-y}Cu_yO_7$ ($y = 0.2$) films grown on STO at 800 °C.

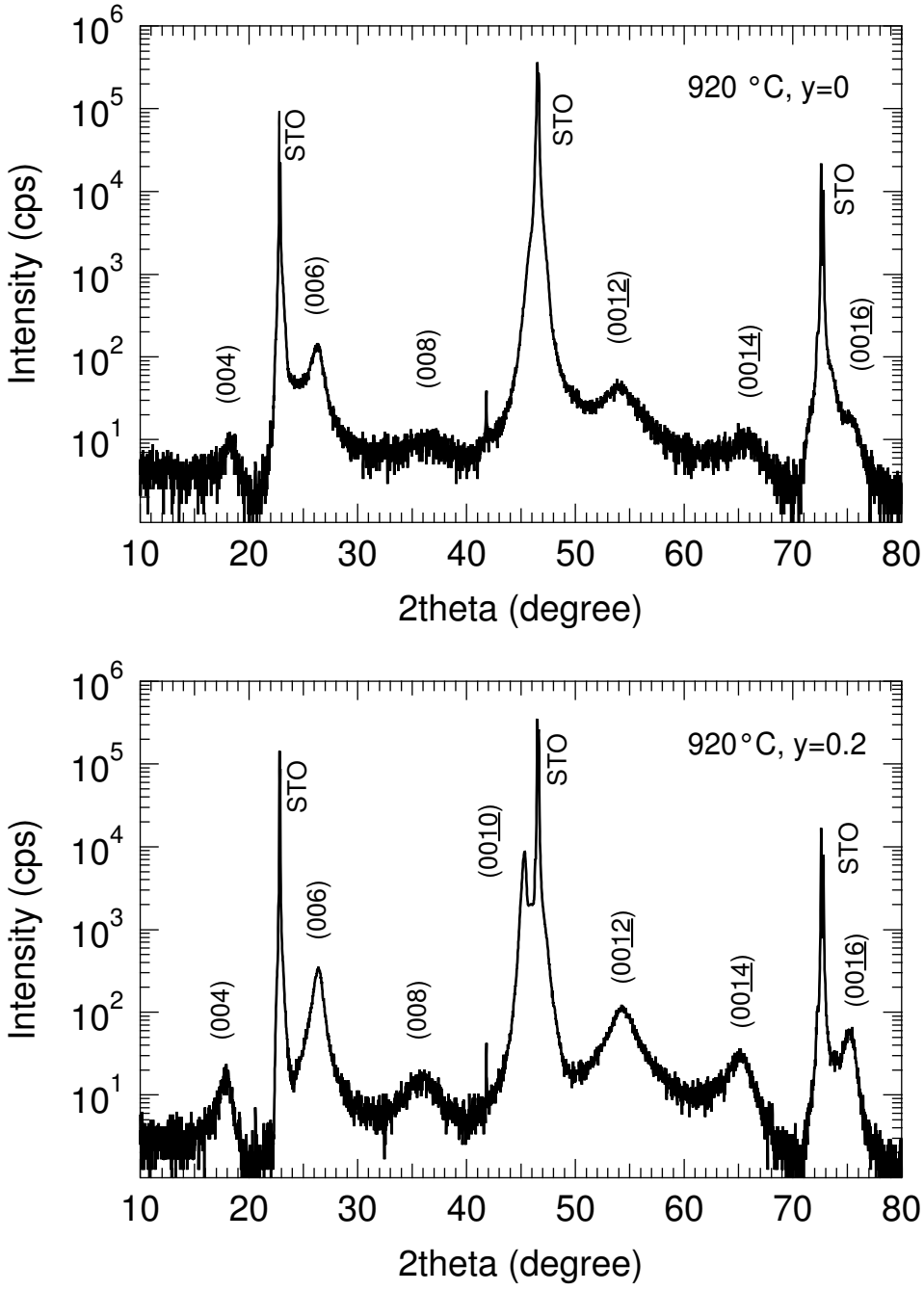

Figure 5.3: XRD patterns for non-doped $La_{2-2x}Sr_{1+2x}Mn_2O_7$ and Cu-doped $La_{2-2x}Sr_{1+2x}Mn_{2-y}Cu_yO_7$ ($y = 0.2$) films grown at 920 °C.

Table 5.1: FWHM of the XRD peaks for unsubstituted and Cu-substituted c-axis layered manganate thin films.

Cu	(004)	(006)	(008)	(00$\underline{1}$0)	(00$\underline{1}$2)	(00$\underline{1}$4)	(00$\underline{1}$6)
0 %	0.90 ^{o}	1.20 ^{o}	6.80 ^{o}	-	3.70 ^{o}	5.00 ^{o}	-
10 %	0.86 ^{o}	0.84 ^{o}	4.20 ^{o}	0.35 ^{o}	2.24 ^{o}	2.76 ^{o}	1.24 ^{o}

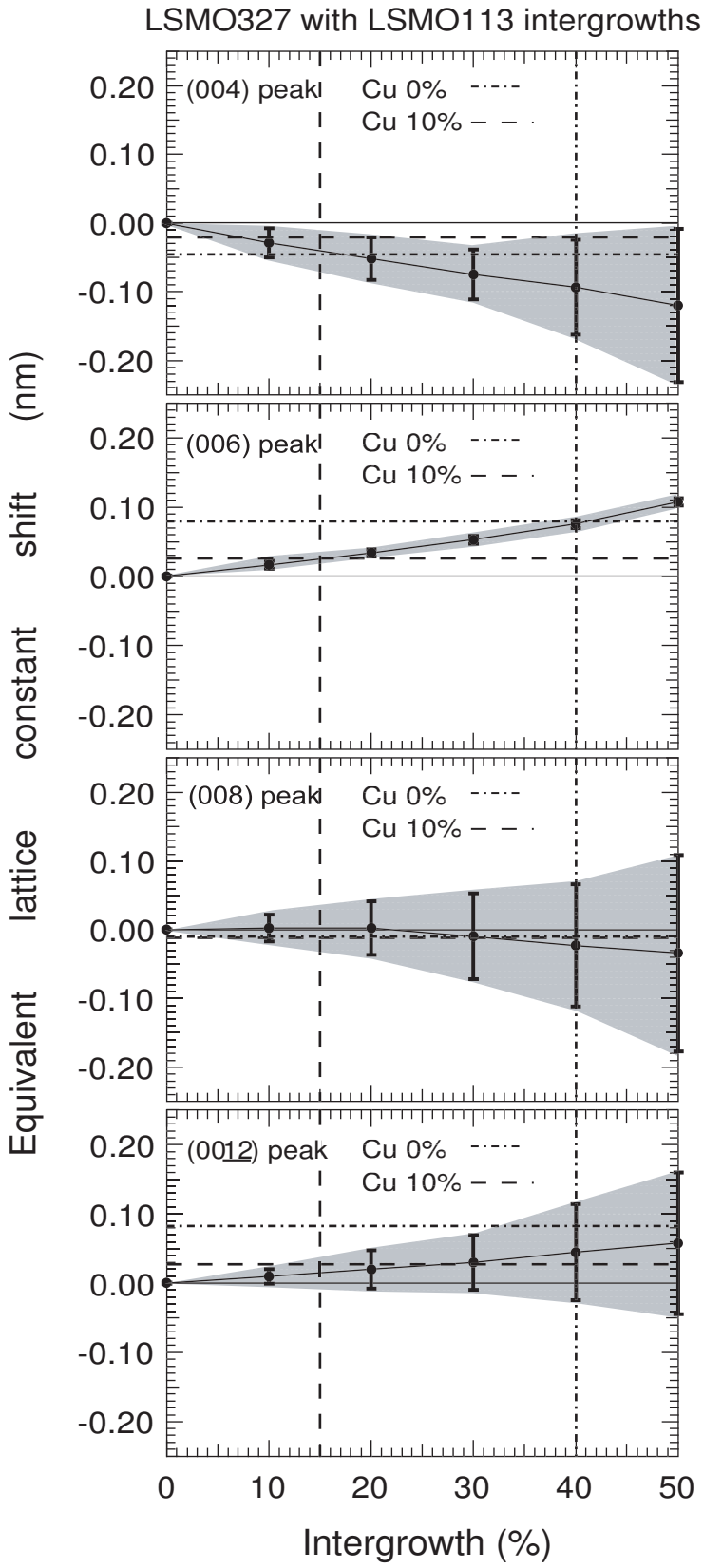

Figure 5.4: Simulation result on the dependence of the equivalent lattice constant shift (ELCS) on the LSMO113 intergrowth content. The error bars in the ELCS are due to the uncertainties in the lattice constants of the considered phases (5 %).

on the intergrowth dependence of the equivalent lattice constant shift (ELCS) for several diffraction peaks, where ELCS for a given peak indicates the change in the lattice constant c from the value determined by the (00$\underline{1}$0) peak when the value for c is calculated from the single peak position via the Bragg equation. Depending on the values for c used in the simulation, the ELCS value changed. If a $\pm$ 5 % variation of $c = 0.388$ nm for LSMO113 and $c = 2.00$ nm for LSMO327 is incorporated, the ELCS value varies within the error bar or in the shaded area shown in Fig. 5.4. It is seen that the ELCS for (006) shows a systematic shift with increasing intergrowth content. This peak, in contrast to the others, includes only a negligible error due to uncertainties in the value for c of the different phases. Therefore, the intergrowth content included in the grown films is determined dominantly by the (006) ELCS. The dashed and dash-dotted lines in the figure show, respectively, the observed equivalent lattice constant shift for the different peaks indicated, for the unsubstituted and Cu-substituted films. It is seen that a good agreement with the experiments is obtained when the intergrowth content is roughly 40 % and 15 % in the unsubstituted and the Cu-substituted films, respectively. Therefore, it is estimated that approximately half of the intergrowth is reduced by the Cu-substitution.

5.3 Effect of Cu-Substitution on Magnetic, Electrical, and Magnetoresistive Properties

In order to study the effect of Cu-doping on the magnetic properties of layered manganates, small polycrystalline bulk pellets of $La_{1.4}Sr_{1.6}Mn_{2-y}Cu_yO_7$ ($y = 0.0$, 0.1, 0.2, and 0.3) were fabricated. They were prepared by calcining at 800 °C for 12 h in air and then sintering at 1450 °C for 20 h in flowing O_2. The sintering process was repeated several times.

Except for the non-doped sample, all the bulk polycrystal samples were single phase as revealed by powder XRD. The non-doped sample showed some impurity phase of La_2O_3, which destroyed the non-doped pellets within a few days due to its strong water-absorption property. The crystal structure for all the samples could be indexed according to the $Sr_3Ti_2O_7$-type tetragonal structure ($14/mmm$). The obtained powder XRD patterns are similar to those shown in Section 2.1.2.

As Cu was gradually introduced, the lattice constants of the crystal structure changed correspondingly as shown in Fig. 5.5. It is seen that, with Cu-doping, the a-axis lattice constant a decreased, while the c-axis lattice constant c increased.

5.3.1 Effect of Cu on magnetization

Figure 5.6 shows the temperature dependence of magnetization $M - T$ for $La_{1.4}Sr_{1.6}Mn_{2-y}Cu_yO_7$ ($y = 0.0$, 0.1, 0.2, 0.3) bulk polycrystals under a magnetic field of 1 T. For the non-doped $La_{1.4}Sr_{1.6}Mn_2O_7$, an abrupt increase in magnetization is seen

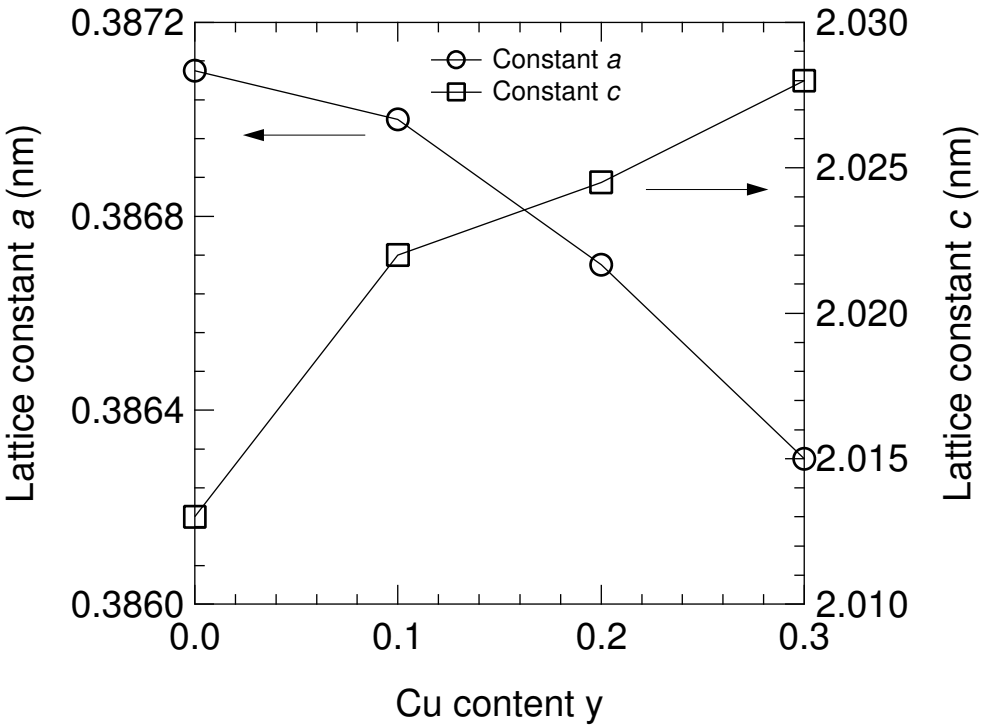

Figure 5.5: Dependence of the a and c lattice constants on the Cu content y for $La_{1.4}Sr_{1.6}Mn_{2-y}Cu_yO_7$ bulk polycrystals.

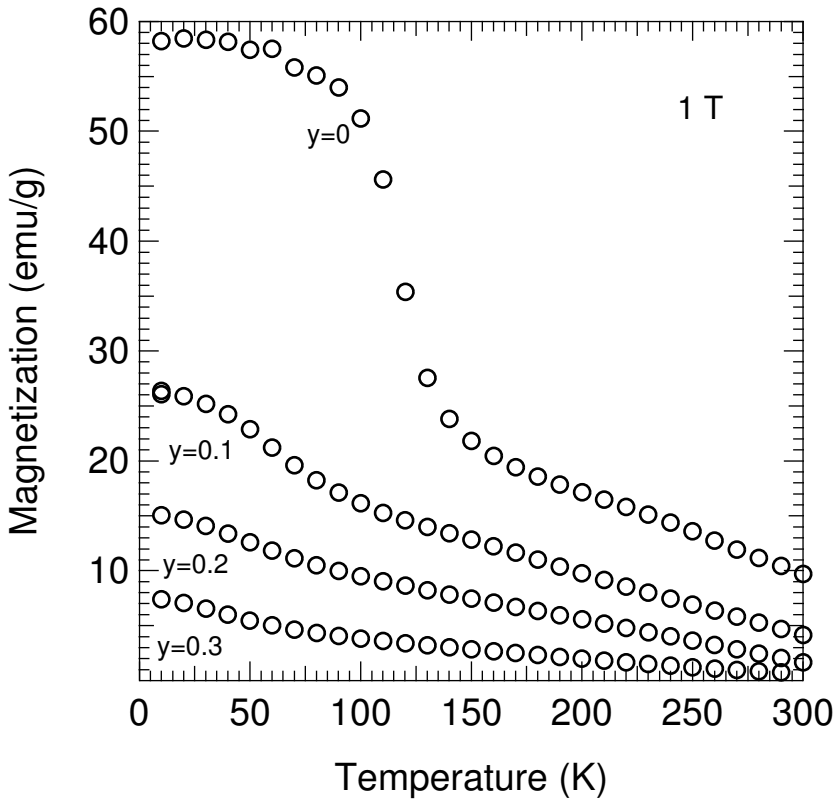

Figure 5.6: Temperature dependence of magnetization for $La_{1.4}Sr_{1.6}Mn_{2-y}Cu_yO_7$ ($y = 0.0$, 0.1, 0.2, 0.3) bulk polycrystals, under a magnetic field of 1 T.

near 120 K, indicating the onset of the ferromagnetic ordering. Above this temperature, a signal presumably due to a remnant LSMO113 phase is observed. This is similar to results reported in other studies.

As can be seen in Fig. 5.6, the magnetic order gradually vanishes and the value of the magnetization decreases as Cu is introduced into the crystal structure. From the above results, it is clear that Cu-doping destroys strongly ferromagnetism in the bilayer manganate system. This effect seems to be stronger than that in cubic Ca-doped manganates of the LSMO113 type. It has been reported that 5 % of Cu-doping in $La_{0.7}Ca_{0.3}MnO_3$ manganates affected their magnetic properties only negligibly (Fig. 5.1) [1].

5.3.2 Effect of Cu on electrical resistivity

The above suppression of magnetic properties for layered manganates when Cu is doped is reflected in the temperature dependence of their electrical resistivity, as shown in Fig. 5.7. As is known for double exchange metallic systems [3], a metal-insulator (MI) transition associated with the onset of ferromagnetism is seen for $y = 0$ and 0.1, near 120 and 70 K, respectively. For $y = 0.2$ and 0.3, however, a semiconducting behavior with no MI transition is seen down to the lowest temperature measured.

5.3.3 Effect of Cu on magnetoresistance

Upon application of magnetic fields, a decrease in resistivity is seen down to low temperatures, as shown in Fig. 5.7. At 9 T, the magnetoresistance value $-[\rho(B) - \rho(0)]/\rho(0)$, was 90% and 95.5% for LSMO327 with $y = 0$ and $y = 0.1$ at the MI transition temperature of 120 K and 70 K, respectively. Although 5 % of Cu-doping decreased T_C by nearly 50 K, it slightly enhanced the magnetoresistance. Moreover, this enhancement became substantial at low temperatures, as seen in Fig. 5.8.

5.4 Discussion

5.4.1 Enhancement of *c*-axis epitaxial growth by Cu-substitution

As explained in Chapter 4, the *c*-axis film growth in the anisotropic layered manganates can be considered to occur as follows. The crystal growth is much slower in the *c*-axis direction than along the *ab*-direction. Therefore, when the substrate temperature is low and/or the rate is high, the film has to adjust its slow *c*-axis growth in parallel to the surface and the fast *a*-axis growth along the deposition direction, because the atom migration at the surface is weak. Thus, at low substrate temperatures, the *a*-axis film growth is preferred. By the same reasoning, when the substrate temperature is raised and/or the deposition rate is lowered, the fast *a*-axis growth becomes possible along the substrate surface, and the *c*-axis growth is obtained [2].

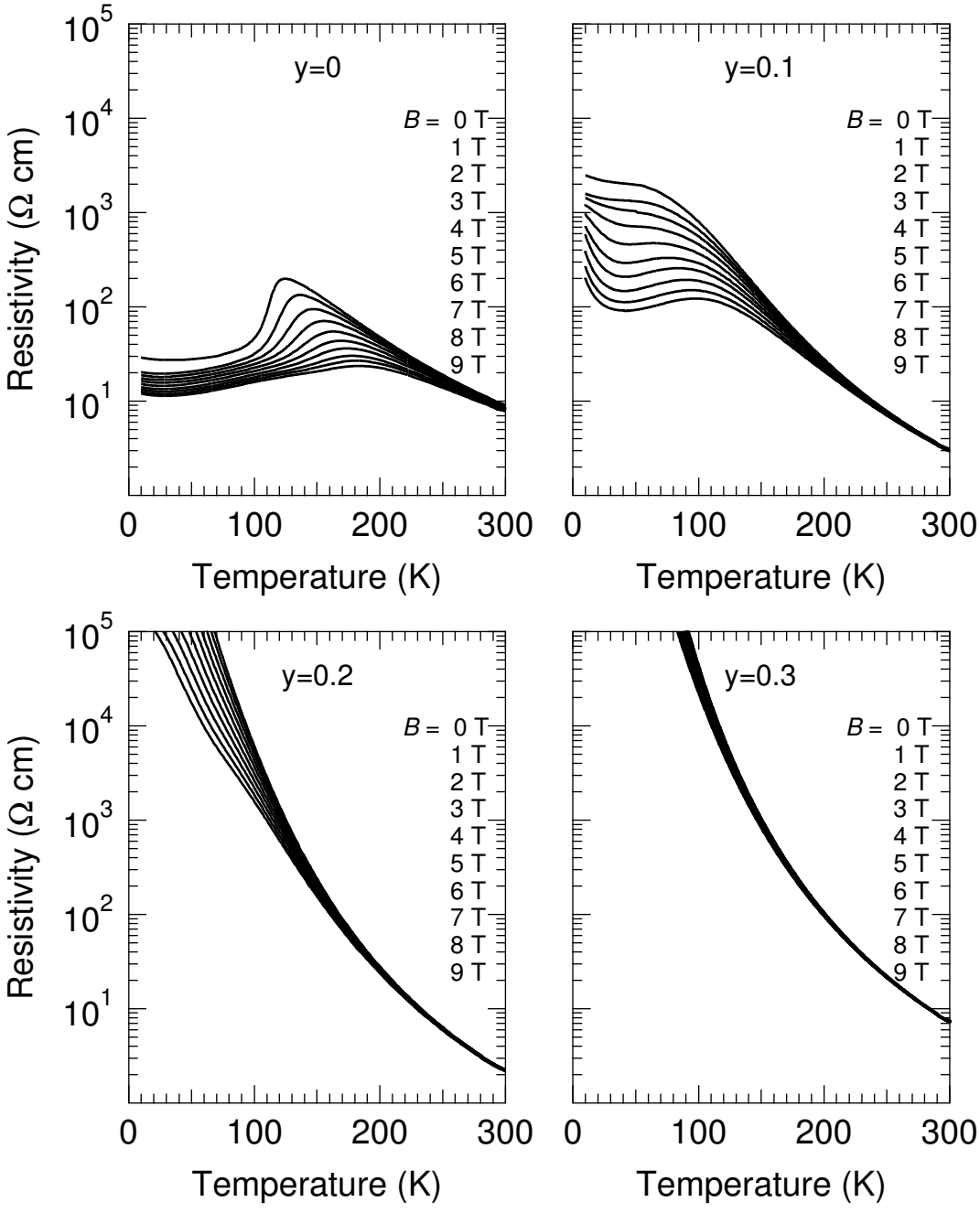

Figure 5.7: Temperature dependence of electrical resistivity for $La_{2-2x}Sr_{1+2x}Mn_{2-y}Cu_yO_7$ ($y = 0.0, 0.1, 0.2, 0.3$) bulk polycrystals, under different magnetic fields in the range $0-9$ T.

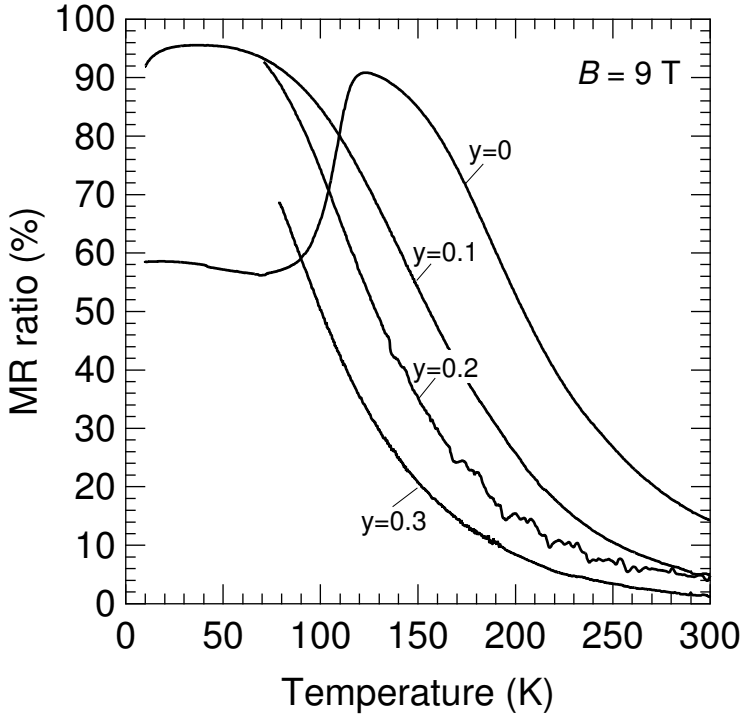

Figure 5.8: Magnetoresistance (MR) ratio for $La_{1.4}Sr_{1.6}Mn_{2-y}Cu_yO_7$ (y = 0.0, 0.1, 0.2, 0.3) bulk polycrystals in the presence of a magnetic field of 9 T.

The improvement of the c-axis epitaxy by Cu-substitution is considered to be due to the lowering of the melting point and to the increase in the atomic migration at the substrate surface, which is necessary for the c-axis epitaxial growth. As a result, the amount of LSMO113 intergrowth structure was suppressed by 50 % in Cu-substituted films.

5.4.2 Suppression of magnetic and electrical properties by Cu-substitution

The manganates are mainly double-exchange systems. According to Zener's double exchange (DE) model [3], the ferromagnetic interaction occurs via the exchange of conduction electrons between Mn ions through O ions. The amplitude of the effective electron hopping between Mn^{3+} and Mn^{4+} (i and j sites) is expressed as:

$$t_{ij} = t_{ij}^0 \cos(\theta_{ij}/2),$$

where t_{ij}^0 is the maximum hopping amplitude, and θ_{ij} is the relative angle between the neighboring site spins. t_{ij} depends both on the distance between Mn and O ions and on the Mn^{3+}-O-Mn^{4+} angle.

With Cu-doping, the a-axis lattice constant decreased and the c-axis lattice constant increased as shown in Fig. 5.5. Therefore, in the MnO_2 bilayers, the Mn^{3+}-O-Mn^{4+} angle probably became larger, and thus, the DE interaction was suppressed. Moreover, because the distance between the MnO_2 bilayers became also larger, it is possible that the ferromagnetic coupling between the bilayers became weaker as Cu was introduced. The Cu-substitution for Mn also creates Cu-O-Mn bonds with no DE interaction, which certainly destroys more or less the magnetic properties of the manganates. This effect, however, seems to be weak in some manganates of the LSMO113 type as reported by other studies [1], but a large change in the crystal structure with Cu-doping did not take place as was the case for the present bilayer manganates.

5.5 Summary

In summary, the effect of Cu-substitution of the Mn site in layered manganates on the c-axis epitaxial growth of these materials has been studied. It is found that Cu-substitution is found effective in improving the c-axis epitaxial growth for $La_{2-2x}Sr_{1+2x}Mn_2O_7$ bilayer manganates. Compared with non-substituted films, the amount of LSMO113 intergrowth structure was suppressed by 50 % in Cu-substituted films.

The magnetic, electrical, and magnetoresistive properties of Cu-doped bilayer manganates $La_{2-2x}Sr_{1+2x}$- $Mn_{2-y}Cu_yO_7$ ($x = 0.3$, $y = 0.0$, 0.1, 0.2, 0.3) also have been studied. It is found that although Cu-doping suppresses the magnetic properties of the bilayer manganates, it enhances fairly their magnetoresistance at small dopings.

Cu-substituted films with suppressed magnetic and electrical properties can serve as buffer layers or as tunnel barriers in multilayer manganate structures.

References

[1] K. Ghosh, S. B. Ogale, R. Ramesh, R. L. Greene, T. Venkatesan, K. M. Gapchup, R. Bathe, and S. I. Patil, Phys. Rev. B **59**, 533 (1999).

[2] H. Asano, Dr. Thesis, Nagoya University, Nagoya, Japan, 1992 [in Japanese].

[3] C. Zener, Phys. Rev. **82**, 403 (1951).

Chapter 6

A New Sputtering Configuration for c-Axis Bilayer Manganate Epitaxial Thin Films with Reduced Intergrowths

6.1 Introduction

To study the unusually high magnetoresistance effect seen in the bilayer manganates, high-quality c-axis epitaxial thin films are necessary [1–7]. c-Axis epitaxial films were demonstrated in Chapter 4, where a growth rate of as low as 0.8 nm/min was found necessary. These films grown by conventional sputtering, however, contained large amounts of intergrowths ($\sim 40\,\%$). A partial Cu-substitution of the Mn site helps to improve the crystallinity of the films to some extent, but it degrades their magnetic properties as shown in Chapter 5.

Considering the layered structure of these materials, one can say that their growth needs a special care. Namely, one has to be sure that the layered structure formed during the growth is not destroyed by energetic events such as the bombardments of the film by high-energy particles that normally exist in the sputtering of oxides such as negative oxygen ions (Fig. 6.1) [8]. In the case of LSMO327, the bombardment of energetic particles may cause stacking faults which lead to the intergrowth of the $La_{1-x}Sr_xMnO_3$ (LSMO113) structure or the $La_{2-x}Sr_xMnO_4$ (LSMO214) structure. The latter LSMO214 is an antiferromagnetic insulator [3, 9, 10]. Therefore, the intergrowth of LSMO214 is undesirable among others. It is also important to ensure a stable substrate temperature during the whole growth process. In the conventional sputtering configuration, the substrate temperature is inevitably lowered when the shutter is opened. This change in the substrate temperature is also undesirable and should be eliminated.

These drawbacks of conventional sputtering are largely eliminated by placing an intermediate plate between the target and the substrate. In Section 6.2, this modification of

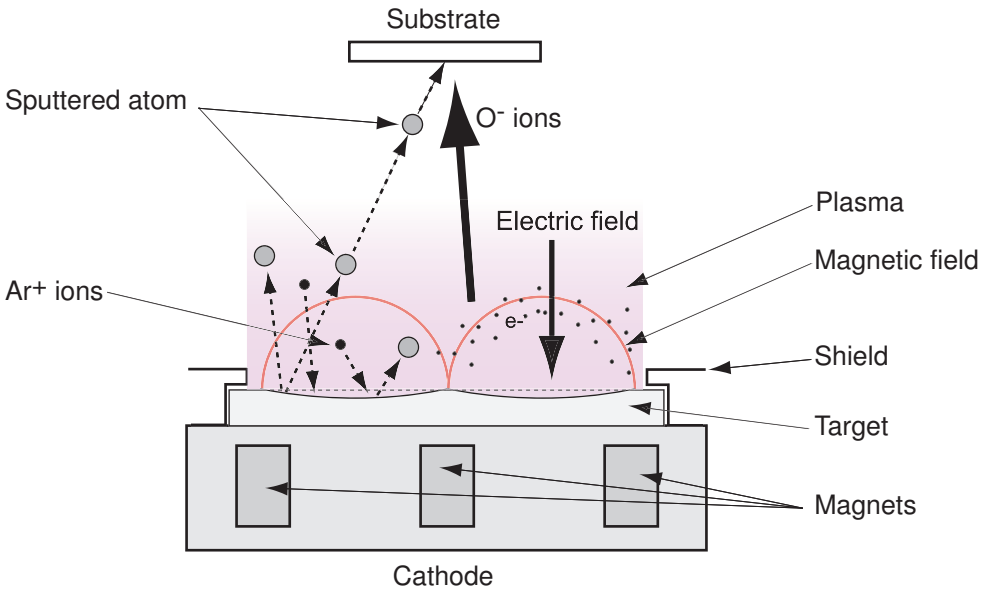

Figure 6.1: Conventional on-axis magnetron sputtering configuration.

sputtering configuration is described. By using this technique, *c*-axis LSMO327 epitaxial thin films with reduced intergrowths have been achieved. This is reported in Section 6.3. Film properties are described in Section 6.4.

6.2 Modification of Sputtering Configuration

6.2.1 Sputtering with intermediate plate configuration

The proposed sputtering configuration is shown schematically in Fig. 6.2. An intermediate stainless steel plate is placed between the target and the substrate. The plate has 42 holes of 8 mm in diameter in the peripheral area, as shown in Fig. 6.2(b). The substrate–plate and plate–target distances are 50 and 25 mm, respectively. In this configuration, it is expected that the high energy particles that hit the substrate are reduced in numbers significantly because nearly direct paths which involve a small number of scatterings are hindered in the presence of the intermediate plate. The effect of this intermediate plate manifests itself as the reduction in the composition deviation of the films. The inserted plate also ensures a stable substrate temperature even at the instant when the shutter is opened.

6.2.2 Advantages of sputtering with intermediate plate configuration

Figure 6.3 shows the substrate temperature (T_{sub}) dependence of the film compositions, [Mn]/([La]+[Sr]) and [Sr]/([La]+[Sr]), in the presence or in the absence of the intermediate plate. Although a slight increase in the [Mn]/([La]+[Sr]) ratio is seen, the film composition remains essentially constant when the plate is used. This is sharply contrasted with the result that a considerably large increase in the Mn content is observed in the absence of the plate. The Sr content also clearly decreases with increasing T_{sub} when the plate is absent, while it remains constant in the presence of the plate. It is presumed that this stability in the film composition is achieved because the plate eliminates the bombardment of the film by the high-energy particles that exist during sputtering, e.g., negative O ions. The effect of the bombardment is usually enhanced at higher substrate temperatures. It can be said that the film composition, in this case, is determined mainly by the scattering characteristics of the sputtered atoms during their transport from the target to the substrate through the holes of the plate. The atoms sputtered from the target reach the substrate after being scattered a number of times. The number of the scatterings increases with increasing atmosphere pressure. The scattering amplitude is a function of the scattering angle and its function differs among different kinds of atoms. Therefore, it is generally inevitable that the composition of the film differs from that of the target. The excessiveness of the Mn and Sr atoms in Fig. 6.3 implies that Mn and Sr atoms are scattered more widely than La atoms. In the presence of the plate, the resputtering effect, which largely causes the composition

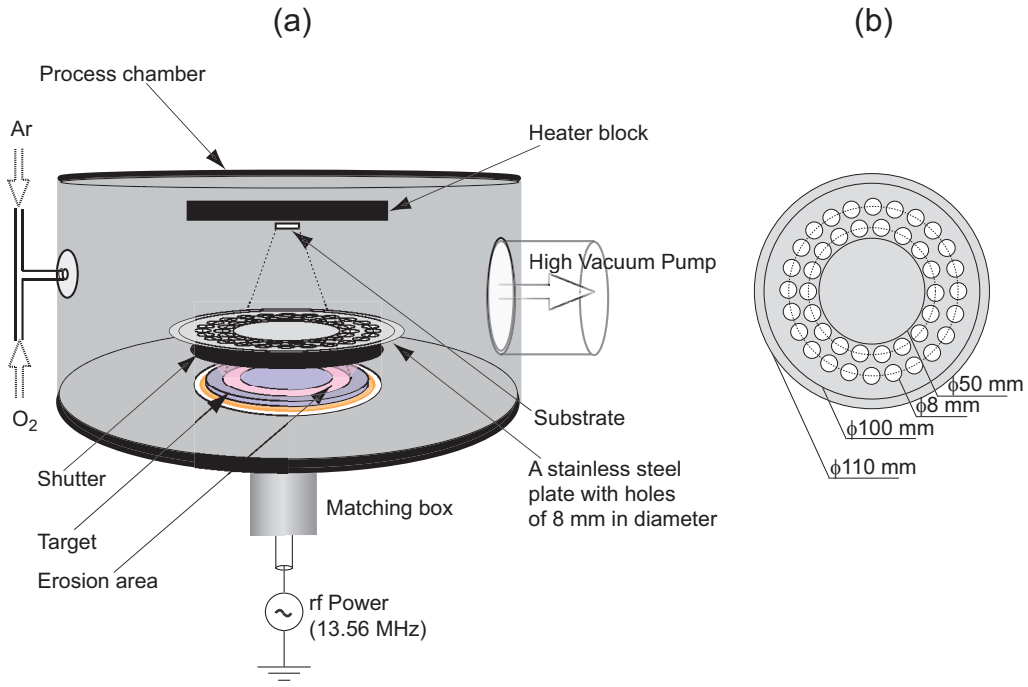

Figure 6.2: (a) Schematic of the new sputtering configuration. An intermediate plate made from stainless steel with holes of 8 mm diameter drilled in the periferal area is placed between the target and the substrate. (b) Schematic of the intermediate plate's structure.

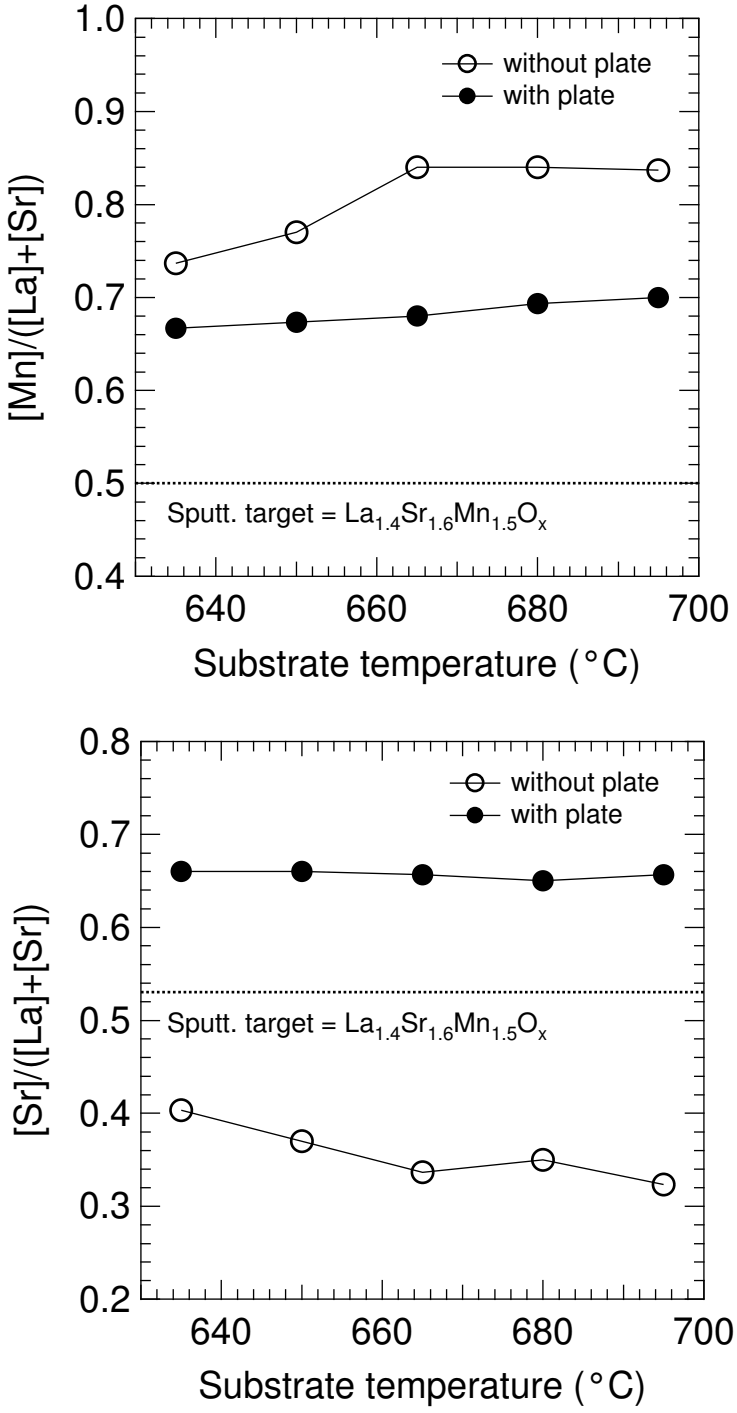

Figure 6.3: Dependence of film composition on substrate temperature. The open and filled circles correspond to the sputtering configurations with and without the intermediate plate, respectively. The anode voltage was 2.0 kV, and the chamber gas pressure was 20 mTorr.

deviation, is almost suppressed, as supposed from the nearly constant substrate temperature dependence of the composition shown in Fig. 6.3.

There is another advantage for this configuration. The insertion of the intermediate plate eliminates the temperature drop of about 20 °C, which is always seen after the shutter opening in the absence of the intermediate plate. In the present experiments, the temperature remains unchanged irrespective of shutter positions. This obviously improves the quality of crystal growth.

6.3 *c*-Axis Epitaxial Growth of $La_{2-2x}Sr_{1+2x}Mn_2O_7$ Thin Films

6.3.1 Conditions of thin film growth

c-Axis LSMO327 epitaxial thin films were grown on $SrTiO_3$ (STO) (100) substrates in the modified sputtering configuration described above. The substrate temperature was 670 °C. High purity Ar and O_2 gases were used as sputtering atmosphere, where the fractional ratio of O_2 in the mixed gas was fixed at 20 %. The sputtering pressure P_s was maintained during the film growth at 40 mTorr. The anode voltage was 2.3 kV. Films were annealed at 900 °C for 9 h in flowing oxygen.

With or without the intermediate plate, it is clear that the film's Mn composition becomes much higher than that of the target, as seen in Fig. 6.3. Therefore, Mn-deficient targets are necessary to grow films with a stoichiometric Mn content. The Sr composition of the target must also be adjusted so that the Sr composition of the film be in the ferromagnetic range ($0.3 \leq x \leq 0.4$). Thus, the *c*-axis films grown here were sputtered from a $La_{1.52}Sr_{1.48}Mn_{1.33}O_y$ target, which is 33.5 % Mn-deficient. Energy dispersive spectroscopy (EDX) analysis, conducted on films grown on sapphire substrates ($1\bar{1}02$), revealed a typical film composition of $La_{1.3}Sr_{1.7}Mn_2O_{7+\delta}$. The film thickness was approximately 250 nm, and the deposition rate was approximately 0.6 nm/min.

6.3.2 Characterization of *c*-axis epitaxial growth

Figure 6.4 shows an XRD pattern for an almost stoichiometric film grown using the above sputtering configuration on an STO (100) substrate at $T_{sub} = 670$ °C. The same figure shows also an XRD pattern when a film similar to the one mentioned above is annealed at 900 °C in flowing oxygen. In both patterns, only (00ℓ) peaks are seen, which indicates that the films are grown in the *c*-axis direction (*c*-axis films). Below this substrate temperature, it was found that the *a*-axis and *c*-axis growth modes coexist.

The *c*-axis lattice constant for the as-grown LSMO327 *c*-axis epitaxial films was evaluated to be 2.032 nm from the position of the main peak (00$\underline{10}$). This value is slightly larger than the bulk value of 2.020 nm [3]. The positions of the other (00ℓ) peaks also coincide almost

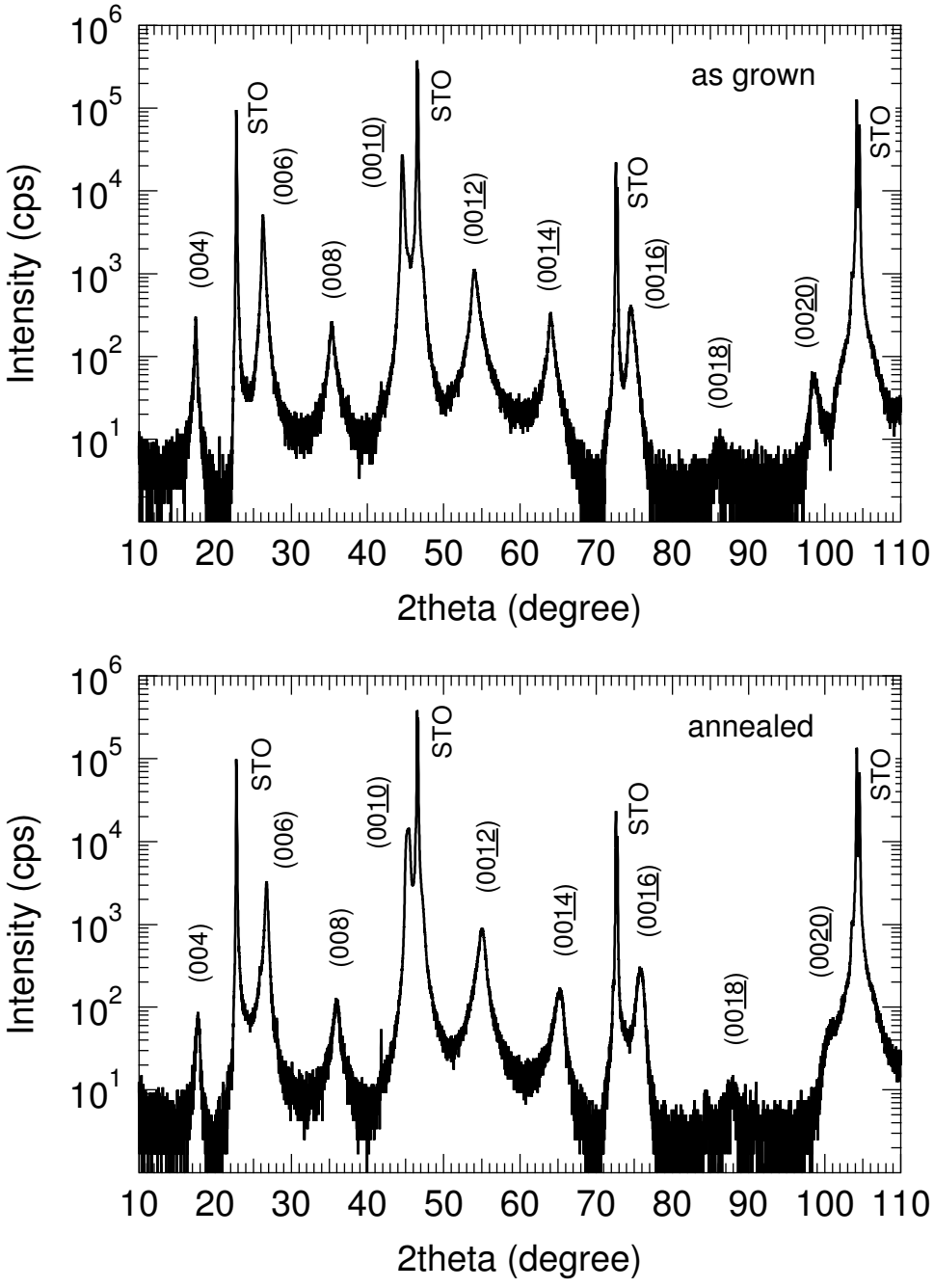

Figure 6.4: XRD patterns for bilayer manganate c-axis epitaxial thin films grown on STO substrates at $T_{\text{sub}} = 670\,^{\circ}\text{C}$ using the new sputtering configuration.

exactly with the positions expected from this value, as shown in Table 6.1. This was not the case in films grown by the conventional sputtering method, in which a large amount of intergrowths ($\sim$ 40 %) causes the shift of the diffraction peaks. This implies that the intergrowths in the present films are reduced appreciably. From XRD simulation analysis, of which the methodology was outlined in Chapter 4, it is deduced that the intergrowth content is less than 20 % (10 % of LSMO113 and 10 % of LSMO214). The simulated XRD pattern for a film which includes this amount of intergrowths is shown in Fig. 6.5. It is seen that the simulation result is in good agreement with the experimental result. The present films show much smaller values for the full width at half maximum (FWHM) than the films grown previously. For example, the FWHM value is $\sim 0.3°$ for the diffraction peak (00$\underline{1}$0) and $\sim 0.6°$ for (008), while they were $\sim 0.5°$ and $\sim 3.0°$, respectively, for films of Chapter 4. The values of the shift of the XRD peak position and those for FWHM are listed in Table 6.1 and Table 6.2 for as-grown and annealed films together with the simulation result. As is seen in Table 6.2, a general agreement between the experimental and simulated FWHM data is obtained. However, large deviations from the simulation results are seen for the peaks (004), (008), (00$\underline{1}$6), (00$\underline{1}$8), and (00$\underline{2}$0). These peaks are sensitive to the lattice constants of the included intergrowths as described in Section 5.2. It is supposed that a better agreement can be obtained by taking into account the uncertainty in the lattice constants of the included LSMO113 and LSMO214 phases.

After annealing the film in O_2, the c-axis lattice constant decreased to 2.001 nm, presumably due to oxygen incorporation and strain relief, and the FWHM values slightly increased as shown in Table 6.2. However, the intergrowth content evaluated as above almost remained the same even after the annealing.

Film surfaces observed by HRSEM are shown in Fig. 6.6 both for the as-grown film and for the annealed film described above. The as-grown films show a relatively smooth surface, but when annealed, the surface becomes a little rougher with a small amount of precipitates.

6.4 Magnetic, Electrical, and Magnetoresistive Characterization

6.4.1 Magnetic properties

Magnetization measurements were made under an applied magnetic field of 1 T parallel to the film surface. Figure 6.7 shows the temperature dependence of magnetization M for as-grown and annealed films. The negative values of M for the as-grown film are due to errors of the background subtraction using a dummy substrate. The values for M per Mn atom were calculated from the observed magnetic moment of the samples by assuming that the films are composed of the LSMO327 phase only. As can be seen, the magnetization for

Table 6.1: Shift of the experimental 2θ value for each XRD peak from the corresponding 2θ value calculated using (00$\underline{10}$) peak.

Film	(004)	(006)	(008)	(00$\underline{10}$)	(00$\underline{12}$)	(00$\underline{14}$)	(00$\underline{16}$)	(00$\underline{18}$)	(00$\underline{20}$)
as-grown	0.01 °	−0.03 °	−0.02 °	0.00 °	−0.09 °	−0.05 °	−0.11 °	0.19 °	−0.08 °
annealed	0.05 °	0.08 °	0.08 °	0.00 °	0.02 °	0.03 °	−0.19 °	0.11 °	0.13 °
simulation	0.31 °	−0.03 °	−0.50 °	0.00 °	−0.30 °	−0.27 °	−0.01 °	−0.59 °	0.03 °

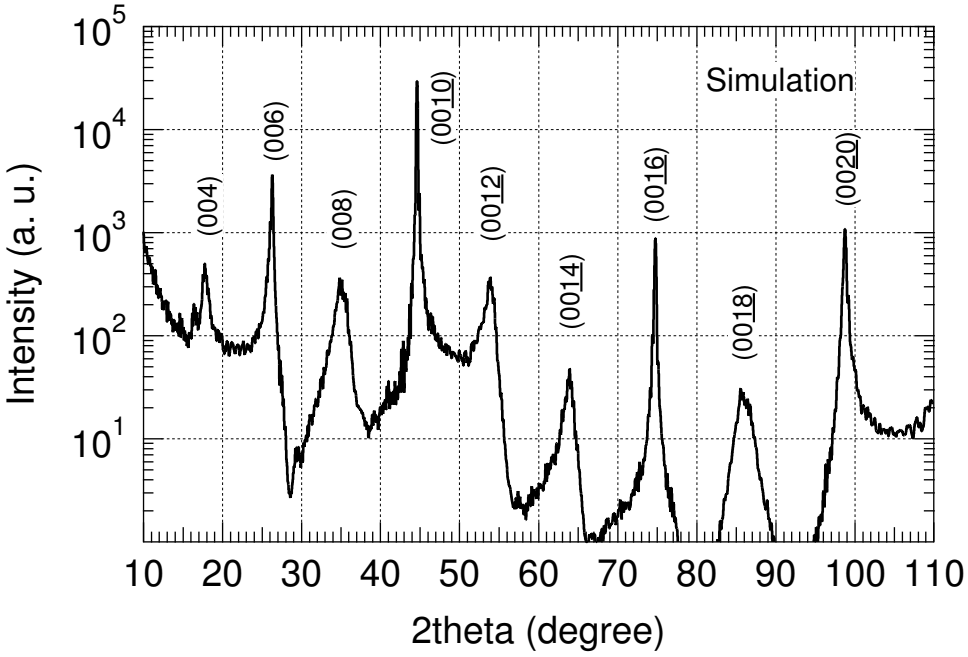

Figure 6.5: Simulated XRD pattern for a *c*-axis bilayer manganate film with 20 % of intergrowths (10 % of LSMO113 and 10 % of LSMO214).

Table 6.2: FWHM of the XRD peaks for as-grown, annealed, and simulated *c*-axis LSMO327 epitaxial thin films.

Film	(004)	(006)	(008)	(00$\underline{10}$)	(00$\underline{12}$)	(00$\underline{14}$)	(00$\underline{16}$)	(00$\underline{18}$)	(00$\underline{20}$)
as-grown	0.23 °	0.31 °	0.56 °	0.34 °	0.79 °	0.56 °	0.69 °	1.09 °	1.30 °
annealed	0.47 °	0.35 °	0.77 °	0.63 °	0.92 °	1.06 °	0.97 °	1.75 °	-
simulation	0.75 °	0.23 °	1.24 °	0.21 °	1.09 °	0.89 °	0.25 °	1.71 °	0.34 °

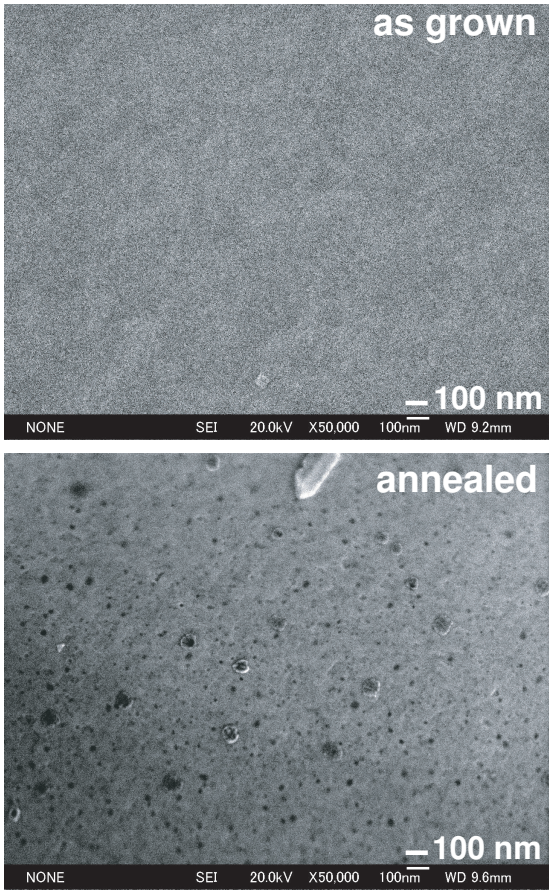

Figure 6.6: HRSEM surface images for LSMO327 *c*-axis epitaxial films grown on STO (100) substrates using the new sputtering configuration.

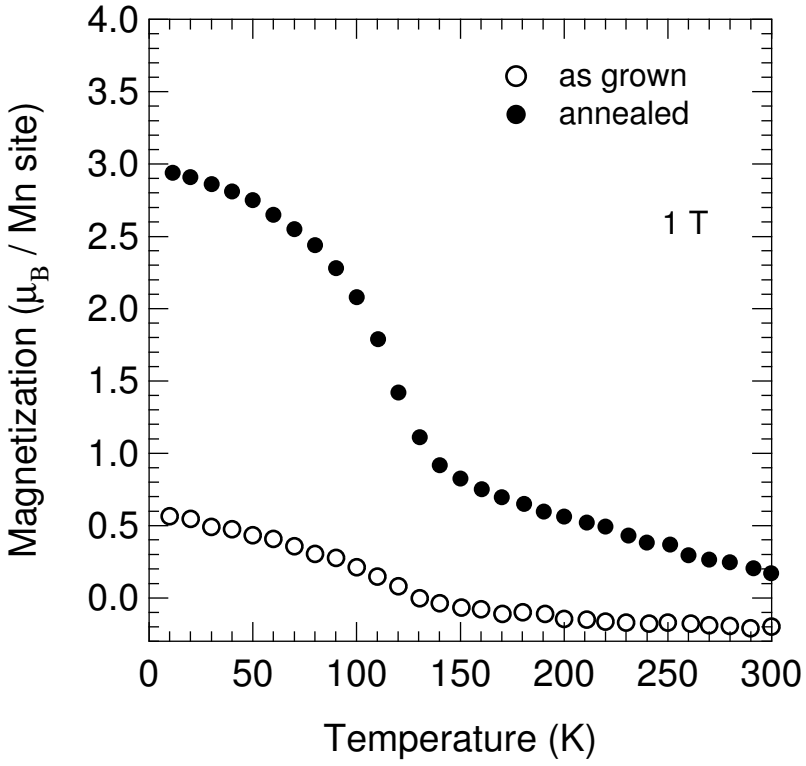

Figure 6.7: Temperature dependence of magnetization for *c*-axis LSMO327 epitaxial thin films grown using the new configuration. The negative magnetization seen at high temperatures for the as-grown film is considered to be due to relatively large errors in the dummy measurements because of feeble measurement signals.

both films shows an abrupt increase around 140 K as T is decreased. The magnetization value for the annealed film is, however, much higher than that for the as-grown one, and is about 3.0 μ_B per Mn atom at low temperatures.

This value is close to the theoretical value of 3.65 μ_B expected for the full spin polarization. As the ferromagnetic interaction occurs via the exchange of conduction electrons between Mn ions through O ions [11], the low magnetization values for the as-grown film can be attributed to oxygen vacancies and other lattice imperfections.

The Curie temperature T_C is about 140 K for both as-grown and annealed films, respectively. These values are slightly higher than that for the bulk ($\sim$ 115 K), possibly due to some remnant LSMO113 intergrowth phase. The contribution from these phases is clearly seen in the range between 140 K and room temperature.

6.4.2 Electrical properties

Figure 6.8 shows the temperature dependence of electrical resistivity for the annealed film. Those for as-grown films are not shown here, as they are semiconducting in the whole temperature range measured, with a room temperature resistivity ranging from 0.07 to 0.15 Ω cm. From Fig. 6.8, it is seen that the temperature dependence of resistivity for the annealed film has a peak that indicates the metal-insulator (MI) transition at 144 K. These temperatures are very close to the corresponding T_C's determined from the above magnetization measurements. The resistivity of the films at room temperature is nearly equal to that observed in the bulk [3].

6.4.3 Magnetoresistance

Upon application of magnetic fields, a decrease in resistivity is observed in the whole temperature range measured, as shown in Figure 6.8. At a magnetic field of 7 T, the magnetoresistance $-\Delta\rho/\rho_0$, defined as $-\Delta\rho/\rho_0 = -[\rho(B) - \rho(0)]/\rho(0)$, reached the highest value of more than 60 % around 120 K. The magnetoresistance is greater than 50 % at all temperatures below the MI transition temperature of 144 K. These values are much larger than those obtained in the sputtered films of Chapter 4, but smaller than the value of 98 % observed at 7 T for a c-axis film grown by pulsed laser deposition [12].

6.5 Discussion

The lanthanum manganate crystallizes in different crystal structures of the Ruddelsden-Popper series, $(La,Sr)_{n+1}Mn_nO_{3n+1}$ [9]. (La,Sr)MnO_3 (LSMO113), in the case of $n = \infty$, has a cubic perovskite structure, and is the most stable and easily formed one under wide range of conditions. For $n \geq 1$, the crystal structure can be regarded as a stack of n consecutive LSMO113 layers and a (La,Sr)O layer along the c-axis, showing crystallographic anisotropy.

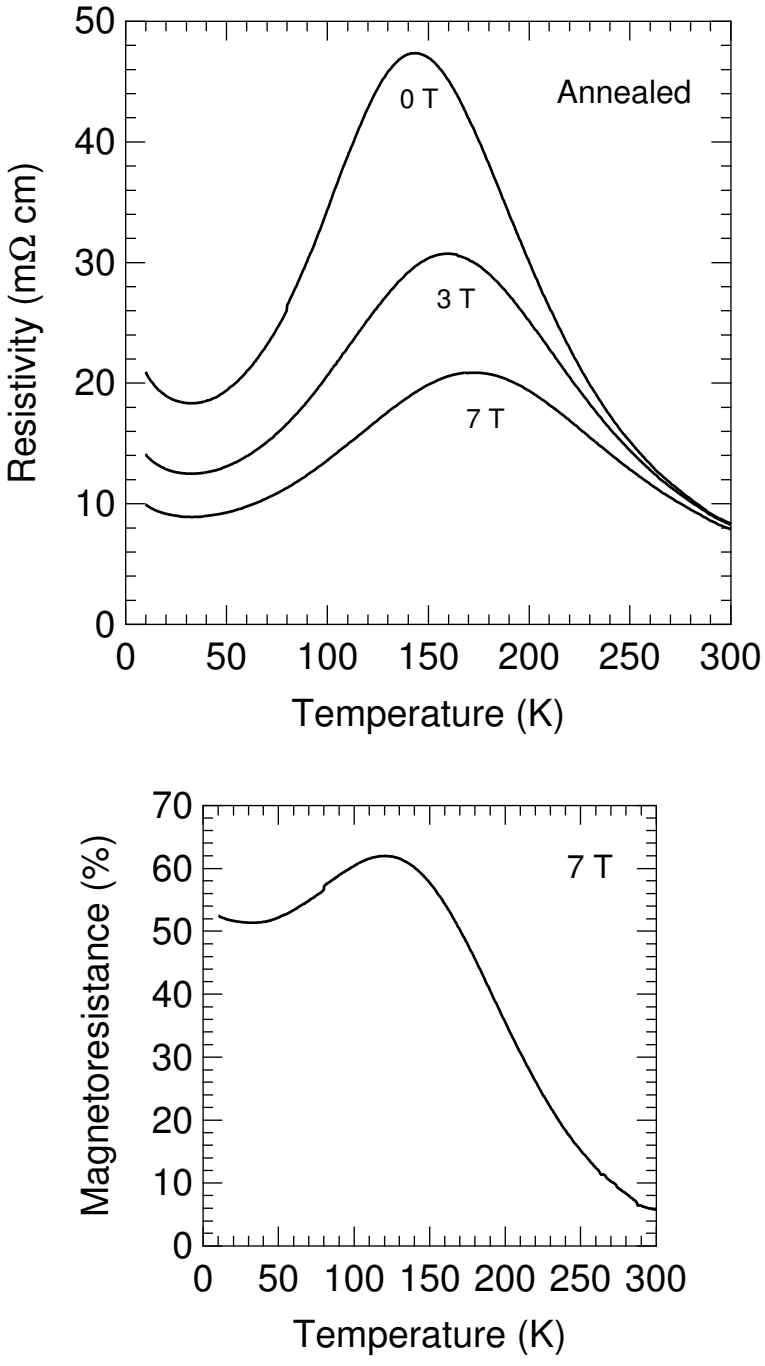

Figure 6.8: Temperature dependence of electrical resistivity and magnetoresistance for *c*-axis epitaxial LSMO327 films. The magnetic fields were parallel to the film surface. The films were grown on STO (100) using the new sputtering configuration, and subsequently annealed in O_2.

One can clearly imagine that any disturbance of a such layered structure easily results in the inclusion of an additional LSMO113 layer, i.e., an LSMO113 intergrowth. In the case of LSMO327, an increase in the number of the MnO_2 layers causes LSMO113 intergrowths, while a decrease in the number of MnO_2 layers leads to LSMO214 intergrowths. These intergrowths are caused by composition fluctuations, particle bombardments of the growing film, and so on. These must be avoided in order to grow high-quality layered manganates free of intergrowths. In the case of sputtering, high-energy particles always exist, and these must be eliminated before hitting the growing film [8]. Moreover, in order to provide a stable environment for the epitaxial growth, one must circumvent the disturbances coming from the substrate temperature drop commonly seen during the initial stage of the film growth due to the shutter opening. In the present experiment, the new sputtering configuration in which an intermediate plate is placed between the substrate and the target plays both of the above roles, yielding c-axis epitaxial films for the bilayer manganates LSMO327 with much less intergrowths. Using this method, films with intergrowth contents below 20 % have been successfully grown. This result presents a sharp contrast with those for the films of Chapter 4 grown using the conventional sputtering configuration, which contain ~ 40 % of intergrowths.

In accordance with the improved crystallinity results mentioned above, the magnetic and magnetoresistance properties of the films show characteristics comparable with those for the bulk ones. The fact that the magnetization increases significantly after annealing implies that the as-grown films contain rather a large amount of oxygen vacancies, which is compensated by annealing. It is seen in Fig. 6.7 that the magnetization increases significantly after the annealing while the Curie temperature T_C remains near 140 K. It is reasonably understood that the oxygenation by the annealing increases the Mn sites at which the double exchange interaction is effective, leading to an increase in the magnetization. The increase in the magnetization is also observed above T_C after the annealing. This is interpreted to be caused by an increase in the LSMO113 phase intergrowth. This is also reflected by the results that the FWHM values also increased after the annealing, as seen in Table 6.2.

On the other hand, T_C is primarily determined in terms of $J_{i,j}$, the exchange coupling coefficient, and z, the configuration number, within the framework of the mean field theory. These values are basically unchanged when the oxygen content is increased. However, when the amount of LSMO113 intergrowths increases, it is possible that the average value for z increases to a small extent, because in the layered manganates, $J_{i,j}$ is known to be large within the MnO_2 bilayers and small between the same bilayers in the c direction due to the crystal anisotropy, while in the isotropic LSMO113, $J_{i,j}$ is the same in the c-axis direction. This may lead to an increase in T_C. The observed value of $T_C = 140$ K, which is higher than that of the bulk by 25 K, may reflect this effect of the intergrowth on the Curie temperature.

6.6 Summary

To summarize, c-axis $La_{2-2x}Sr_{1+2x}Mn_2O_7$ epitaxial films have been grown using a new sputtering configuration. Films with reduced intergrowth contents less than 20 % have been obtained. This has been achieved by the insertion of an intermediate plate between the substrate and target. The plate suppresses the high-energy particle effects that exist in normal sputtering, and eliminates the temperature drop seen after the shutter opening. These films show also good magnetic and magnetoresistive properties. They can be used to study the intrinsic spin tunneling effect, which is thought to endow these materials with unusually high magnetoresistance values. This may uncover also previously unknown phenomena, leading to the conception of new electronic spin devices.

References

[1] T. Kimura, Y. Tomioka, H. Kuwahara, A. Asamitsu, M. Tamura, and Y. Tokura, Science **274**, 1698 (1996).

[2] Y. Moritomo, Y. Tomioka, A. Asamitsu, Y. Tokura, and Y. Matsui, Phys. Rev. B **51**, 3297 (1995).

[3] T. Kimura and Y. Tokura, Ann. Rev. Mater. Sci. **30**, 451 (2000).

[4] H. Asano, J. Hayakawa, and M. Matsui, Phys. Rev. B **56**, 5395 (1997).

[5] T. Kimura, A. Asamitsu, Y. Tomioka, and Y. Tokura, Phys. Rev. Lett. **79**, 3720 (1997).

[6] T. G. Perring, G. Aeppli, T. Kimura, Y. Tokura, and M. A. Adams, Phys. Rev. B **58**, R14693 (1998).

[7] S. Heim, T. Nachtrab, M. Mö, R. Kleiner, R. Koch, S. Rother, O. Waldmann, P. Müller, T. Kimura, and Y. Tokura, Physica C **367**, 348 (2002).

[8] H. Asano, Dr. Thesis, Nagoya University, Nagoya, Japan, 1992 [in Japanese].

[9] Y. Tokura (Ed.), *Colossal Magnetoresistive Oxides* (Gordon and Breach, 2000).

[10] S. Larochelle, A. Mehta, L. Lu, P. K. Mang, O. P. Vajk, N. Kaneko, J. W. Lynn, L. Zhou, and M. Greven, Phys. Rev. B **71**, 024435 (2005).

[11] C. Zener, Phys. Rev. **82**, 403 (1951).

[12] Y. Konishi, T. Kimura, M. Izumi, M. Kawasaki, and Y. Tokura, Appl. Phys. Lett. **73**, 3004 (1998).

Chapter 7

Conclusions

In the present thesis, *c*-axis epitaxial growth and characterization for thin films of colossal magnetoresistive layered manganates have been studied towards the extraction of coherent spin tunnel junctions for studies of spin tunneling phenomena. The epitaxial growth and characterization of LSMO113 films has been studied first because it is of great value when analyzing and discussing the properties of LSMO327 thin films. These films have been also exploited to fabricate a spin-injection device. *c*-Axis epitaxial layered manganate thin films have been achieved by controlling deposition rate. Characterization of these films has indicated that they include intergrowths of other phases, and the quantitative method of characterizing these intergrowths has been also presented. Partial substitution of Mn for Cu has been found effective in improving the *c*-axis epitaxial growth for layered manganates, but it degrades their magnetic properties. Using a newly proposed sputtering configuration, *c*-axis epitaxial layered manganate thin films with fairly reduced intergrowths have been successfully grown. The main results obtained in this study can be summarized as follows.

In Chapter 3, the epitaxial growth and characterization for LSMO113 thin films has been described. The relation between epitaxial thin film growth and sputtering conditions was studied. The electrical and magnetic properties of the films were characterized and the optimal epitaxial growth conditions were determined. It is found that epitaxial thin films grown at 820 °C have the best crystalline quality compared with those grown at lower substrate temperatures. When these films were annealed in oxygen at 900 °C, they showed magnetic and electrical characteristics comparable to those of bulk single crystals. LSMO113 thin films thus grown showed streaky RHEED patterns , which indicates that their surface is considerably smooth and that they are suitable for multilayer film fabrication. Exploiting their full spin polarization property, LSMO113 epitaxial thin films were combined with high-T_c superconductor thin films to fabricate a spin-injection device. A suppression in the superconducting transition temperature was found as expected, but a negative resistance was recorded. Further optimization of the spin-injection structure is needed.

In Chapter 4, the *c*-axis epitaxial growth and characterization for the layered manganate $(La,Sr)_3Mn_2O_7$ have been studied. It was shown that at the high deposition rates of

$\sim$ 25 nm/min, only *a*-axis thin films could be grown. *c*-Axis thin films appeared at substrate temperatures above 900 °C. However, their crystalline quality was very poor, and therefore, the deposition rate was decreased in order to improve the *c*-axis epitaxial growth. It is found that, by decreasing the growth rate from 25 nm/min to 0.8 nm/min, the film quality is largely improved. The magnetic and electrical properties were, however, far from the bulk ones, and the surface of the film showed many precipitates because the film contained many intergrowths such as LSMO113 and LSMO214. A quantitative method of characterizing these intergrowths based on X-ray diffraction (XRD) experiment and simulation has been presented. The results indicated that the above *c*-axis LSMO327 epitaxial thin films contained about 40 % of intergrowths.

In Chapter 5, the effects of Cu-substitution of Mn on the *c*-axis epitaxial growth and the properties of layered manganates have been studied. Cu-substitution facilitates the fabrication of sputtering targets for the manganates, but most importantly, it lowers their melting point. Therefore, the atom's migration is fostered at the growing film surface. This is of crucial importance for *c*-axis epitaxial growth. It is found that, as expected, the *c*-axis epitaxial growth is improved by introducing Cu. Films grown with Cu-substitution had an amount of intergrowths half that seen in non-substituted films. It is found, however, that Cu suppresses strongly ferromagnetism in layered manganates.

In Chapter 6, in order to grow better *c*-axis epitaxial layered manganate thin films, a new sputtering configuration has been proposed. By placing an intermediate plate between the sputtering target and the substrate, the high-energy particles that exist during sputtering were suppressed. Thus, the film growth took place in a mild environment free from disturbances, as revealed by the robustness of film composition against substrate temperature. Using this configuration, *c*-axis epitaxial layered manganate thin films with intergrowth contents less than 20 % were achieved. The electronic properties of these thin films were close to those of bulk single crystals. These *c*-axis epitaxial layered manganate thin films with reduced intergrowth contents can be used for intrinsic spin tunneling studies such as those based on small mesa structures on film's surface.

List of Publications

A. Publications Related to this Work

A-1. Full Length Papers and Letters

1. M. Lmouchter, M. Iwayama, Y. Tanaka, and M. Suzuki,
"Growth and Properties of c-Axis Epitaxial Thin Films for $La_{2-2x}Sr_{1+2x}Mn_2O_7$ Bilayer Manganates by Sputtering,"
Jpn. J. Appl. Phys. **44**, 6016–6024 (2005).

2. M. Lmouchter, M. Iwayama, and M. Suzuki,
"Effect of Cu-Substitution on the Epitaxial Growth for $La_{2-2x}Sr_{1+2x}Mn_2O_7$ Bilayer Manganates,"
Jpn. J. Appl. Phys. **45**, 4042–4043 (2006).

3. M. Lmouchter, R. Tatsumi, T. Ikawa, and M. Suzuki,
"Growth of c-Axis Epitaxial Thin Films with Reduced Intergrowths for the Bilayer Manganate $La_{2-2x}Sr_{1+2x}Mn_2O_7$ Using a New Sputtering Configuration,"
Jpn. J. Appl. Phys. **47**, 908–913 (2008).

A-2. International Conferences

1. M. Lmouchter, H. Endo, Y. Nakamura, M. Iwayama, Y. Tanaka, and M. Suzuki,
"Epitaxial Manganate Thin Films by Sputtering for Spin Injection into High-T_c Superconductors,"
Physica C **445**, 865-868 (2006).
(*Proc. Intern. Symp. on Superconductivity*, Tsukuba, Japan, 2005.)

A-3. Domestic Conferences

1. M. Lmouchter, M. Iwayama, Y. Tanaka, and M. Suzuki,
"Growth and Properties of Sputtered c-Axis $La_{1.25}Sr_{1.75}Mn_2O_7$ (LSMO327) Thin Films,"
Fall Meeting of the Japanese Society of Applied Physics, Sep. 2004, Sendai.

2. Y. Nakamura, H. Endo, T. Nagahisa, M. Lmouchter, and M. Suzuki,
   "Fabrication and Transport Property of Epitaxially Grown $La_{2-x}Sr_xCuO_4/La_{1-x}Sr_xMnO_3$ Tunnel Junctions,"
   Fall Meeting of the Japanese Society of Applied Physics, Sep. 2005, Tokushima.

3. Y. Nakamura, T. Nagahisa, K. Honma, H. Endo, M. Lmouchter, and M. Suzuki,
   "Fabrication and Transport Property of Epitaxially Grown $La_{1-x}Sr_xMnO_3/La_{2-x}Sr_xCuO_4$ Tunnel Junctions,"
   Fall Meeting of the Japanese Society of Applied Physics, Aug. 2006, Kusatsu.

4. R. Tatsumi, M. Lmouchter, and M. Suzuki,
   "Ion-Bombardment-Free Sputtering of c-Axis $La_{2-2x}Sr_{1+2x}Mn_2O_7$ Epitaxial Thin Films and their Properties,"
   Fall Meeting of the Japanese Society of Applied Physics, Aug. 2006, Kusatsu.

B. Other Publications

B-1. Full Length Papers and Letters

1. M. Suzuki, K. Anagawa, M. Lmouchter, and T. Watanabe,
   "Distinct Superconducting Gap and the Pseudogap in the Interlayer Tunneling Spectroscopy for $Bi_2Sr_2CaCu_2O_{8+\delta}$,"
   Physica C **362**, 164–168 (2001).

B-2. International Conferences

1. M. Lmouchter, K. Anagawa, M. Suzuki, T. Watanabe, and A. Matsuda,
   "Non-Conventional Temperature Dependence of the Maximum Josephson Current in $Bi_2Sr_2CaCu_2O_{8+\delta}$ Intrinsic Junctions,"
   8$^{\text{th}}$ International Superconductive Electronics Conference, June 2001, Osaka, Japan. (*Ext. Abstr.* 433–434).

2. K. Anagawa, T. Hamatani, M. Lmouchter, M. Suzuki, and T. Watanabe,
   "Short Pulse Tunneling Characteristics for Small Mesas of $Bi_2Sr_2CaCu_2O_{8+\delta}$ Intrinsic Josephson Junctions,"
   8$^{\text{th}}$ International Superconductive Electronics Conference, June 2001, Osaka, Japan. (*Ext. Abstr.* 431–432).

B-3. Domestic Conferences

1. M. Lmouchter, K. Anagawa, M. Suzuki, T. Watanabe, and A. Matsuda,
   "Temperature Dependence of the Maximum Josephson Current of Intrinsic Junctions in $Bi_2Sr_2CaCu_2O_{8+\delta}$,"
   Fall Meeting of the Physical Society of Japan, Sep. 2000, Niigata.